

Controlling light with resonant plasmonic nanostructures

The cover depicts the spiral-shaped waveform of light as it travels along a plasmonic cylindrical waveguide.

Ph.D. Thesis Utrecht University, June 2009

Controlling light with resonant plasmonic nanostructures

René de Waele

ISBN 978-90-77209-34-9

A digital version of this thesis can be downloaded from <http://www.amolf.nl>.

Controlling light with resonant plasmonic nanostructures

Controle over licht met resonante plasmonische nanostructuren

(met een samenvatting in het Nederlands)

Proefschrift

ter verkrijging van de graad van doctor aan de Universiteit Utrecht
op gezag van de rector magnificus, prof. dr. J. C. Stoof,
ingevolge het besluit van het college voor promoties
in het openbaar te verdedigen
op woensdag 17 juni 2009 des ochtends te 10.30 uur

door

René de Waele

geboren op 13 juli 1981 te Oss

Promotor: Prof. dr. A. Polman

The work described in this thesis was part of the research program of the 'Stichting voor Fundamenteel Onderzoek der Materie' (FOM), which is financially supported by the 'Nederlandse organisatie voor Wetenschappelijk Onderzoek' (NWO). This work was also supported by the NanoNed technology program of the Dutch Ministry of Economic affairs.

Keep only change constant...

Contents

1	General introduction	1
1.1	Outline of this thesis	7
2	Fabrication of metal nanostructures	9
2.1	Introduction	10
2.2	Fabrication by electron-beam lithography	10
2.3	Fabrication by ion-beam lithography	12
2.4	Conclusion	16
3	Tunable nanoscale localization of energy on plasmon particle arrays	17
3.1	Introduction	18
3.2	Experimental	20
3.3	Results	20
3.4	Discussion	25
3.5	Conclusion	25
4	Plasmon dispersion in metal nanoparticle waveguides	27
4.1	Introduction	28
4.2	Experimental	29
4.3	Results	30
4.4	Conclusion	35
5	Observation of plasmon modes in Au nanowires using CL spectroscopy	37
5.1	Introduction	38
5.2	Experimental	38
5.3	Results	39
5.4	Conclusion	43
6	Plasmon dispersion in coaxial waveguides from optical measurements	45
6.1	Introduction	46

CONTENTS

6.2	Experimental	47
6.3	Results	48
6.4	Conclusion	56
7	Negative refractive index in coaxial plasmon waveguides	57
7.1	Introduction	58
7.2	Method	60
7.3	Results	62
7.4	Conclusion	69
8	A single-layer negative-index metamaterial at visible frequencies	71
8.1	Introduction	72
8.2	Methods and results	74
8.3	Conclusion	80
	References	81
	Summary	91
	Samenvatting	93
	Acknowledgements	97
	About the author	99
	List of publications	101

General introduction

Metal nanostructures enable the confinement and control of light at nanoscale dimensions [1–3]. This ability is owed to plasmons, coherent oscillations of conduction electrons in the metal that can be excited by an incident electromagnetic wave [4]. The plasmon resonance frequency can be tuned from the ultraviolet up to the infrared by changing the size, shape or composition of the metal nanostructure. Due to the large electron density in a metal, the cross-section for the excitation can be much higher than the geometrical cross-section.

Figure 1.1(a) schematically depicts a plasmonic excitation in a metal nanoparticle. As light impinges on the particle, it polarizes the metal sphere. In this way, optical energy can be stored in the nanoparticle. The confined energy is partly dissipated in the metal by ohmic damping of the charge oscillation, and partly reradiated (scattered). The strength of either process can be engineered by varying the particle size, shape and composition. Silver (Ag) and gold (Au) are the metals with the lowest ohmic damping at optical frequencies, and therefore show the strongest resonant behavior. For Ag and Au nanoparticles with diameters of a few tens of nanometers, absorption governs the plasmon decay, whereas scattering becomes dominant for larger sizes.

The high tunability of the optical properties of metal nanoparticles has led to a large variety of applications. Metal particles with strong absorption can for instance be used for the photothermal treatment of cancer [5], while particles with a large scattering cross-section can improve the extraction efficiency of light emitting diodes [6]. Strongly scattering nanoparticles are also important for light trapping in thin-film solar cells [7]. Other applications of the high field concentration

near metal nanoparticles are found in sensing [8], luminescence enhancement [9], and surface enhanced Raman scattering [10, 11].

Many of these applications rely on the properties of individual metal nanoparticles. The pronounced optical behavior of metal nanoparticles can be further enriched by the realization of electromagnetic coupling among particles. Coupling can lead to strongly enhanced confinement of light in the space between neighboring particles [12–14]. This behavior originates from strong near-field interactions between neighboring nanoparticles. Furthermore, arrays of metal nanoparticles have been proposed to enable optical energy transport via near-field interactions between neighboring particles [15, 16]. Such inherently short-range interactions take place near-instantaneously and quasi-electrostatic models have often been adopted to calculate them.

In more complex plasmon coupling geometries, however, far-range interactions between particles must be taken into account [17–20]. For example, as proposed by Hernández *et al.* [18], field retardation and interference along metal nanoparticle arrays can create strongly localized frequency-tunable energy distributions on the arrays. In general, dynamic plasmon interactions allow for much greater tunability of the optical response than static (near-field) interactions, and as such offer great potential for a large variety of photonic functionalities, like guiding, redirecting, and concentrating light at the nanoscale. So far, experiments that demonstrate these new functionalities are scarce.

Figure 1.1(b) schematically shows a transversely polarized plasmon mode that is guided along a one-dimensional chain of metal nanoparticles. Light is strongly confined in the lateral direction, and the wavelength of the mode, or more generally the dispersion relation, is determined by the dynamic interactions between the particles [17]. So far, the effect of these dynamic interactions on the dispersion relation of metal nanoparticle plasmon waveguides has not been demonstrated experimentally.

A special case of the particle waveguide occurs when the particles are in electrical contact. In this case, plasmons are no longer confined to individual particles, and as a result the optical behavior of the structure changes drastically [14]. The simplest structure that represents this behavior is a metal nanowire (Fig. 1.1(c)) that confines plasmons in only two dimensions. It has been demonstrated that metal nanowires allow for energy transport along the wire axis [21].

The optical response of metal nanowires is strongly dispersive, in particular near the plasmon resonance or when the wire radius is smaller than the skin depth in the metal. Indeed, at high optical frequencies the wavelength of plasmons can become as short as a few tens of nanometers, though at very high ohmic loss, limiting the propagation length to only a couple of optical wavelengths. As

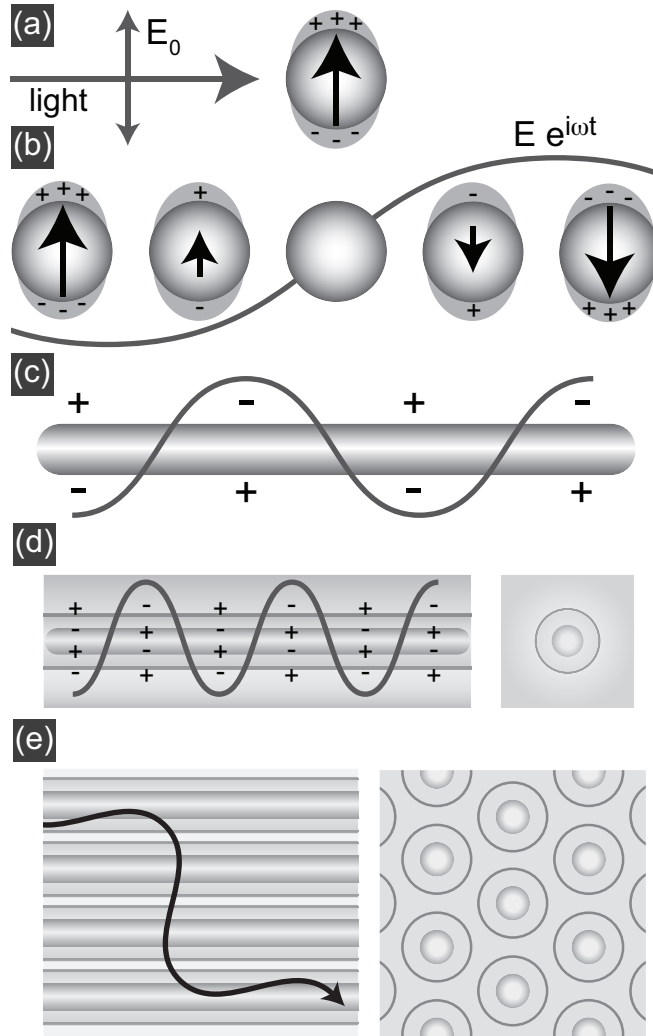


Figure 1.1: Schematic illustrations of plasmon excitations in metallic nanostructures. (a) Optical excitation of a plasmon mode in a metal nanoparticle. A field-induced surface polarization gives rise to a coherent oscillation of conduction electrons. (b) Coherent energy transport in an array of coupled metal nanoparticles. (c) Plasmon excitation in a metal nanowire of finite length giving rise to a standing plasmon wave. (d) Strong optical confinement in a coaxial resonator as result of coupling between plasmons on neighboring metal interfaces. Right hand image shows a transverse cross-section of the waveguide. (e) Light propagation in a metamaterial composed of coupled coaxial waveguides. Right hand image shows a transverse cross-section of the metamaterial.

a result they cannot be excited by plane wave illumination, and localized probes are required to investigate the dispersion. Scanning near-field optical microscopy (SNOM) has been used to characterize the mode structure on metal nanowires [21, 22]. However, this technique is inherently still resolution-limited by the size of tip. Moreover, the tip proximity may have a strong influence on the optical behavior of samples [23].

While metal nanowires offer a lateral field confinement that is much smaller than that in a dielectric waveguide of the same dimensions, the extent of the evanescent tail outside the metal into the dielectric is still of the order of 100 nm. Further control over the lateral mode confinement and dispersion can be achieved using a coaxial geometry composed of a metal wire surrounded by a dielectric channel and clad by an outer metal layer. Figure 1.1(d) shows the coaxial geometry schematically. As plasmons on opposing metal/dielectric interfaces can couple, this geometry gives rise to even stronger plasmon dispersion than is obtainable with metal nanowires. This difference is especially significant at optical frequencies well below the surface plasmon frequency. In this spectral range, the effective index of coaxial waveguides can still be very large, but ohmic losses are relatively low, enabling propagation distances of several tens of micrometers [24]. These predictions make coaxial waveguides very interesting as transport channels for integrated nano-optical circuits. So far, the propagation characteristics of plasmons in individual coaxial waveguides have not been experimentally verified. Furthermore, little is known about the incoupling and outcoupling efficiencies of coaxial plasmon waveguides.

Coaxial plasmon waveguides can be seen as the one-dimensional analogue of planar metal/insulator/metal (MIM) slab waveguides. Recently, it has been shown that certain planar MIM geometries exhibit a negative index of refraction in the visible frequency domain [25, 26]. A negative refractive index is obtained when both the dielectric function, ϵ , and the magnetic permeability, μ , are negative [27]. Although electric resonances giving $\epsilon < 0$ occur at optical frequencies in e.g. metals, naturally-occurring materials with magnetic resonances at optical frequencies are not known. Recently, a new class of materials, called metamaterials has been proposed, in which the resonant behavior is engineered by the sub-wavelength geometry and composition [28]. For example, Smith *et al.* have demonstrated negative refraction in the micrometer wave region in arrays of sub-wavelength copper strips and split-rings printed on a circuit board [29]. More recently, negative-index metamaterials consisting of nanofabricated metallic structures have been attained at near-infrared frequencies [30–32].

Planar MIM structures differ in two important ways from the previously realized negative-index designs. First, MIM waveguides can exhibit a negative index

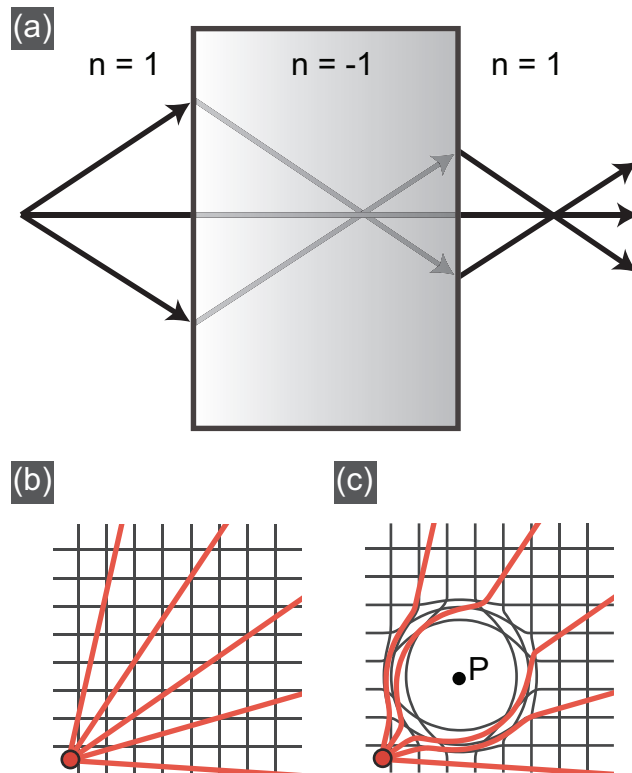


Figure 1.2: Schematic illustrations of several opportunities provided by metamaterials. (a) Focusing of a point source by a perfect lens. Due to negative refraction in the slab with $n = -1$, light makes a focus both inside and outside the lens. (b) Undistorted field lines plotted over a Cartesian grid originating from a point source in free space. (c) Field emerging from the source is excluded from a spherical volume holding an object at point P, thereby rendering the object invisible.

in the visible or ultraviolet domain [26], i.e. at much higher frequencies than other negative index realizations. Second, within an MIM slab, light can propagate in two dimensions via waveguide modes that are characterized by a negative index, whereas other designs rely on the negative response of sub-wavelength elements and often require multiple functional layers to achieve significant scattering [32].

A natural question arises whether coaxial plasmon waveguides can also possess a negative refractive index, and if so, for what geometry and over what spectral range. Naturally, the observation of negative index in individual coaxial waveguides would also inspire three-dimensional designs of negative-index metamaterials, based on arrays of coaxial waveguides. A schematic illustration of such material is shown in Fig. 1.1(e). Coupling between neighboring coaxes could possibly allow for isotropic energy transport within the metamaterial.

Studies of negative index are particularly appealing because of the intriguing phenomena they can lead to [27], such as negative refraction, reverse doppler shifts, and antiparallel energy and phase velocity. As Pendry pointed out in 2000, a slab of negative refractive index material is also capable to image objects with a resolution well below the diffraction limit [33]. This is due to the fact that evanescent field components scattered from the object, that are not collected in a normal lens geometry, are amplified in the negative-index material. In this way, all wave components originating from the source can be restored leading to a focus much smaller than the wavelength. Figure 1.2(a) shows a ray diagram of a point source being focused by a slab of negative index material. As a consequence of Snell's law of refraction the source object is focused one time inside the slab and one time outside. The size of the ultimate focus is limited only by the losses in the negative index metamaterial.

Another appealing application of metamaterials is in invisibility cloaks [28, 34]. This is made possible by the fact that in a metamaterial electromagnetic space is described in terms of a local effective permittivity ϵ , and permeability μ that are designed to vary with position. In this way electromagnetic fields may be manipulated and distorted in a controllable way. Figures 1.2(b,c) show a schematic of a material in which ϵ and μ are varied in such a way that light is excluded from a spherical region around an object at point P. Here, the metamaterial surrounding the region effectively serves as an invisibility cloak for the object. In reality, material losses of the cloak will not enable perfect invisibility. Furthermore, as the optical properties of metamaterials rely on resonances, optimal cloaking is only achieved for a narrow band of frequencies.

1.1 Outline of this thesis

This thesis focuses on manipulation of light at nanoscale dimensions using three different types of resonant plasmonic nanostructures: 1) arrays of coupled metal nanoparticles, 2) metal nanowires, and 3) (coupled) coaxial waveguides.

- Chapter 2 first describes the fabrication of metal nanostructures with well-defined features as small as 20 nm. Two distinct routes for fabrication are described, namely electron-beam lithography in combination with metal lift-off for producing metal nanoparticle arrays on isolating substrates, and ion-beam lithography to form coaxial plasmon waveguides in metal films.
- In chapter 3 we report on the optical behavior of short arrays of Ag particles with sub-wavelength spacing, illuminated with unfocused light incident along the array. Using confocal microscopy, we find that the resonant response is localized on just a few spheres at either the front or back of the array. By changing the incident wavelength we can control which side of the array becomes excited. This work demonstrates a new paradigm for nanoantenna design, which is based on engineering of the interference between multiple antenna elements, rather than relying on field enhancement in the gap between two nanoantennas.
- Chapter 4 describes angle-resolved transmission experiments to determine the plasmon dispersion relations in one-dimensional arrays of coupled Au and Ag nanoparticles. We conclude that long-range dynamic effects dominate the behavior of plasmon particle chains even when structure sizes are only a fifth of the wavelength. This has implications for the design of nanophotonic circuits in general. We also find that, taking into account dynamic effects, the calculated propagation length along the array is much larger than previously estimated using quasi-electrostatic theory.
- Chapter 5 focuses on metal nanowires. We introduce cathodoluminescence imaging spectroscopy as a novel tool to determine the eigenmodes in an optical structure at a resolution less than 10 nm. By combining spectral and spatial information we determine the dispersion relation for plasmons confined within the metal nanowires.
- Chapter 6 describes optical transmission measurements of individual coaxial nano-apertures in a Ag film. We find that the dispersion in the coaxial apertures depends strongly on the refractive index and thickness of the dielectric channel in the coax structures. From the data we conclude that plas-

mon wavelengths as small as 210 nm with propagation lengths of $\sim 2 \mu\text{m}$ are observed in apertures with ~ 50 nm-wide dielectric channels. Large phase shifts occur upon reflection off the end facets of coaxial waveguides, that can be tuned by changing the coax geometry.

- Chapter 7 describes one-dimensional coaxial waveguides, composed of a thin Si channel separating a Ag core and cladding. We calculate that coaxial plasmon waveguides can sustain modes with negative refractive index at optical frequencies. The spectral region of negative index can be shifted throughout the entire visible regime by changing the dielectric channel width. Furthermore, by fine-tuning the dielectric width, the special cases $n = -1$ and $n = 0$ can be achieved in the coax, while maintaining a decay length of 500 nm or more.
- Finally, in chapter 8 we present finite-difference time-domain simulations of the propagation of light in a new metamaterial design based on coupled Ag/GaP/Ag coaxial waveguides. We show that this material exhibits a negative refractive index $n \sim -2$ at visible frequencies that is independent of the angle-of-incidence over an angular range of $\pm 50^\circ$ and independent of polarization. This result is an important step towards the realization of three-dimensional control of optical fields at nanometer length scales.

Altogether, this thesis demonstrates several new concepts for the nanoscale management of light, by using resonant plasmonic nanostructures. We show that these materials can be fabricated, we present optical measurements at the nanoscale to characterize them, and complement this with analytical calculations and simulations. The thesis focuses on acquiring physical insights into nanophotonic confinement, waveguiding, and negative index metamaterials. The presented concepts and insights hold great promise for new applications of resonant plasmonic nanostructures in integrated optics, photovoltaics, solid-state lighting, nano-imaging, and even invisibility cloaking, as will be discussed in succeeding chapters.

Fabrication of metal nanostructures by electron- and ion-beam lithography

Metal nanoparticle chains and coaxial plasmon waveguides were fabricated on glass. Using electron-beam lithography and lift-off Au and Ag particle arrays were fabricated with particle diameters down to 50 nm and an array pitch as small as 75 nm. Using ion-beam lithography coaxial plasmon waveguides composed of a dielectric channel separating a Ag core and cladding were fabricated. By writing a ring-shaped pattern into Ag, coaxial structures with near-vertical dielectric channels as narrow as 20 nm and a length of 250–600 nm were fabricated.

2.1 Introduction

Many inspiring recent ideas in nanophotonics, ranging from nanoscale antennas [13, 35, 36] to negative-index metamaterials [30, 32], require metal structures with sub-50-nm features and very little size dispersion, making sample fabrication a challenge. Electron-beam lithography (EBL), combined with evaporation and lift-off is a powerful technique for fabrication of metal nanostructures. In EBL a pattern is written directly into a polymer resist layer, without the need for a pre-fabricated lithographic mask. The ultimate resolution that can be achieved is <10 nm [37, 38] and is mainly limited by electron scattering in the polymer matrix and swelling of the resist in the developer solution. Additional processing steps required for fabrication of metal nanostructures, including metal evaporation and resist lift-off, further limit the resolution.

A second technique that is relevant for the fabrication of nanophotonic structures is ion-beam lithography (IBL). In IBL, a tightly focused beam of high-energy ions is scanned over a sample to mill nanoscale patterns into thin layers of material. An advantage of IBL over EBL is that nanostructures can be sculpted directly from a deposited layer of material like Ag, without the use of a resist, or lift-off procedure. The resolution of IBL is comparable to that of EBL but depends on many factors, like the material in the layer, the choice of ion and the milling depth.

In this chapter we discuss the fabrication of metal nanostructures on silica substrates by means of EBL and IBL. Section 2.2 deals with fabrication of metal nanoparticle arrays using EBL and lift-off. In section 2.3 we report on fabrication of coaxial metal/insulator/metal waveguides by means of IBL.

2.2 Fabrication of metal nanoparticle arrays by electron-beam lithography and lift-off

Fused silica substrates were sonicated in demineralized water for 10 minutes. Next, the substrates were cleaned in a 1:1:5 mixture of ammonium hydroxide (33 wt.%), hydrogen peroxide (30 wt.%), and water at a temperature of 75 °C for 20 minutes. This process, developed at laboratories of the Radio Corporation of America (RCA), removes organic and metallic residues [39]. Substrates were rinsed in water and subsequently immersed in 2-propanol and blow-dried using nitrogen gas. Next, the samples were spin-coated with a ~150 nm-thick layer of 495k polymethylmethacrylate (PMMA, 4wt.% in methoxybenzene) and baked on a hot plate at 175 °C for 15 minutes. A 15-nm-thick layer of Ge was deposited on top of the PMMA layer by thermal evaporation. This layer both served as a conduction

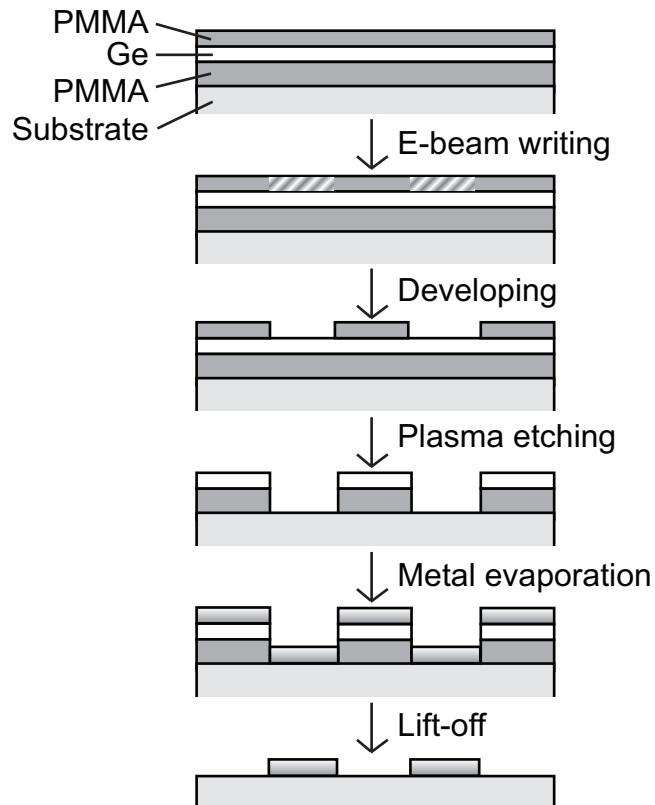


Figure 2.1: Schematic overview of the procedure to fabricate metal nanoparticle arrays using electron-beam lithography and lift-off on silica substrates. The bottom layer of polymethylmethacrylate (PMMA, 495k) has a typical thickness of 150 nm. The Ge layer is 15 nm thick. The top-layer is 950k PMMA with a thickness <100 nm. The evaporated metal thickness is 80 nm or less.

layer to prevent samples from charging during electron-beam exposure and as an etch mask for PMMA. Finally, the samples were spin-coated with a <100-nm-thick layer of PMMA (950k, 2wt.% in methoxybenzene) and baked at 175 °C again.

Figure 2.1 shows a schematic cross-section of a coated sample (top image). Further fabrication steps are also indicated in the figure. First, the PMMA stack was exposed to a strongly focused 30-keV electron beam that was position-controlled by a pattern generator. Upon exposure, cross-links in the PMMA-polymer matrix are broken, which allows for dissolution of the polymer in the developer solution. The programmed patterns consisted of one-dimensional arrays of dots that defined where metal nanoparticles would ultimately be formed on the sample. The electron dosage per dot exposure ranged between 0.05–0.13 pC, while the beam current was fixed at 50 pA.

In the next step, the top PMMA layer was developed in a 1:3 mixture of 4-methyl-2-pentanone and 2-propanol for 30 seconds. The Ge layer prevented development of the bottom PMMA layer. The developed pattern in the top PMMA layer was transferred to the Ge layer by reactive-ion etching (RIE, 40 W) using a plasma of SF₆/O₂, and subsequently transferred to the bottom PMMA layer by a RIE process (50 W) using an O₂ plasma. As PMMA is etched highly anisotropically in this process the ultimate resolution depends mainly on the developed features in the top PMMA layer, where the EBL resolution is generally the best.

Next, we deposited Ag or Au metal on samples by thermal evaporation at deposition rates of typically 0.05 nm/s to a thickness of 80 nm or less. The source crucible was placed at a distance of 50 cm below samples to ensure normal incidence of the evaporated material. In the final step the samples were immersed in acetone of 55 °C for one hour to dissolve the PMMA layer, in order to lift-off all Ag or Au that was not on the substrate, leaving only the designed pattern of metal nanoparticles.

Figure 2.2 shows scanning electron microscopy (SEM) images, taken using a 2 keV electron beam, of samples after lift-off with nanoparticle arrays of Au (a-d) and Ag (e,f). Particles in the image have an average diameter and height of 50 nm; the array-pitch is 75 nm (a,e), 100 nm (b,f), 120 nm (c) and 150 nm (d).

2.3 Fabrication of coaxial plasmon waveguides using ion-beam lithography

Quartz substrates were cleaned following the procedure described in section 2.2. Using thermal evaporation a Ag layer was deposited. The deposited thickness was typically between 200–600 nm and could be varied on a single substrate in stepwise

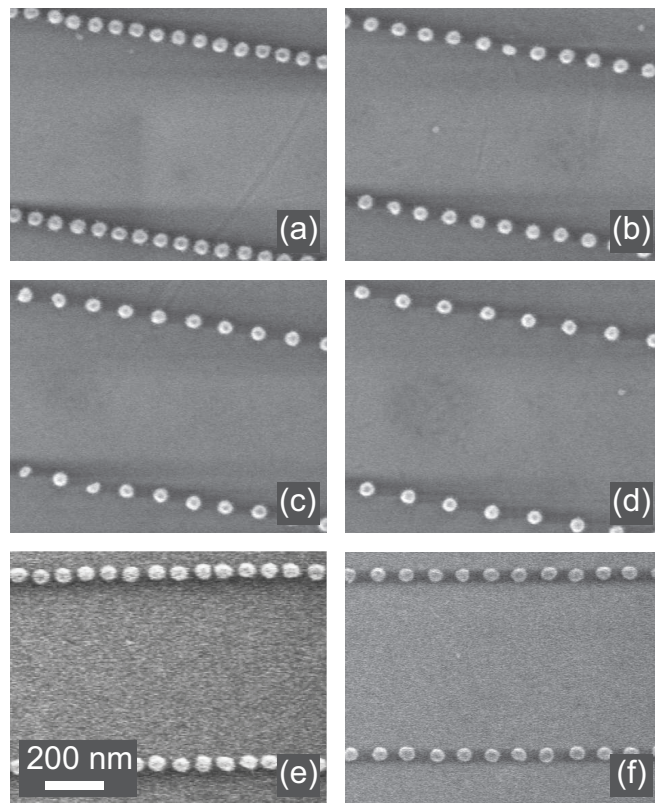


Figure 2.2: Scanning electron micrographs (2 keV electrons) of Au (a–d) and Ag (e,f) particle arrays on glass with particle diameter of 50 nm, and array pitch of 75 nm (a,e), 100 nm (b,f), 120 nm (c) and 150 nm (d).

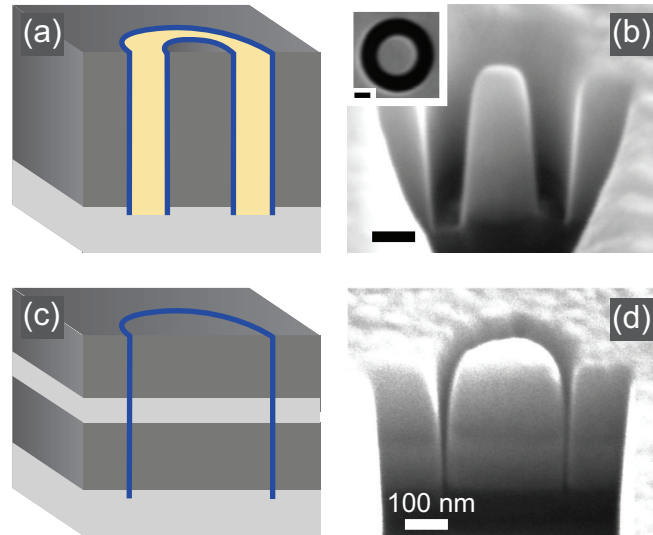


Figure 2.3: Schematic overview of the procedure to fabricate coaxial plasmon waveguides and scanning electron microscopy (SEM) images of coaxial waveguides. (a, c) Schematic cross-sections of a Ag film (a) and Ag/PMMA/Ag stack (c) on a silica substrate. Patterns for ion-beam lithography are indicated in the figures. In (a) the yellow shaded region is milled first, followed by the blue circular rims. In (c) only the blue circular rim is written. (b, d) SEM images (30 keV electrons) of the cross-sectional profile of coaxial plasmon waveguides with lengths of 485 nm, channel widths of ~ 100 nm (b) and ~ 20 nm (d) and outer radii of ~ 175 nm. The inset in (b) show a top view SEM image of the 100-nm waveguide before cross-sectioning.

increments using a mechanical shutter. In this way, layer-thickness dependent measurements could be performed on the same sample.

Coaxial waveguides composed of a Ag core, surrounded by a dielectric channel of 50–100 nm thickness, embedded in a Ag film were made following a two-step Ga-IBL process at a beam-current of 10 pA. The process-steps are indicated in Fig. 2.3(a) which shows a schematic cross-section of the Ag film. First, a 50–100 nm-wide circular channel (yellow shaded region) is milled through the Ag layer using dwell times of 100 ns and a beam step size of 1 nm. After this process step the channel profile is strongly tapered (taper angle is 12° with respect to the central waveguide axis), which is mainly due to redeposition of Ag in the waveguide during FIB milling, an effect that becomes more pronounced deeper in the Ag layer. To reduce the tapering, a second milling pass was used along the inner edges of the channel walls using a dwell time of 20 μ s, indicated in Fig. 2.3(a) by the blue lines.

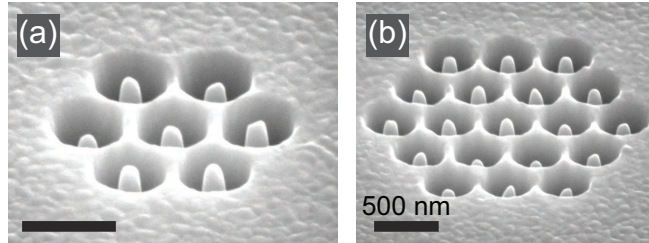


Figure 2.4: Scanning electron micrographs (30 keV electrons) of arrays of coaxial waveguides fabricated by ion-beam lithography, (a): 7-waveguide array; (b): 19-waveguide array. Waveguides have a dielectric channel of ~ 100 nm thickness and Ag core diameter of ~ 150 nm. The array pitch is 450 nm.

After this second pass the channel tapering is reduced to only 7° . SEM images of a typical waveguide with ~ 100 nm-wide channel and outer radius of ~ 175 nm are shown in Fig. 2.3(b). The main panel was taken at a 55° angle with respect to the sample normal after a cross-section was made using ion beam milling. The inset shows a top-view SEM image of the waveguide.

The same fabrication technique was used to make hexagonal arrays of waveguides. Figure 2.4 shows SEM images (taken at a 55° off-normal angle) of arrays of coaxial waveguides with a ~ 100 -nm-wide dielectric channel and core diameter of ~ 150 nm. Figure 2.4(a) shows an array of 7 waveguides, and Fig. 2.4(b) shows an array of 19 waveguides. In both images the array pitch is 450 nm.

For the fabrication of waveguides with dielectric channels of < 20 nm thickness, a 100-nm-thick PMMA film was spun over the Ag layer, followed by evaporation of a second, typically 300-nm-thick, Ag layer, which acts as a sacrificial layer. In this case, the ion-beam written pattern is given by the circular path as schematically indicated in Fig. 2.3(c). Using a dwell time of $20 \mu\text{s}$ a channel is written that is > 50 nm wide and strongly tapered at the beginning, but only < 20 nm wide and nearly vertical at the end. Figure 2.3(d) shows an SEM image of a cross-section of a typical waveguide. Deeper into the Ag/PMMA layer diffusion of sputtered Ag out of the channel is very slow and most material is redeposited on the side walls of the channel, causing the channel to narrow. However, when the channel width becomes comparable to the ion beam waist, material settles at the wider part of the channel thereby reducing channel tapering, or is partially sputtered again. After channels were milled in this way the same lift-off procedure as described in section 2.2 could be used to remove the top sacrificial Ag layer, leaving only the near-vertical, < 20 nm-wide cylindrical channels in Ag.

2.4 Conclusion

We have fabricated metal nanostructures using two different approaches. Electron-beam lithography was used to fabricate Au and Ag plasmon particle arrays on glass. The arrays with the smallest features obtained for this technique had 50-nm-diameter particles and an array pitch of 75 nm. As a second approach, we used ion-beam lithography to form coaxial plasmon waveguides composed of a dielectric cylindrical channel separating a Ag core and cladding. By milling a circular rim into a layered stack of Ag/PMMA/Ag, channels with <20 nm width and up-to 600 nm length could be obtained in the bottom Ag layer, while the top layer may be removed using lift-off. In the remainder of this thesis we investigate the optical properties of the fabricated plasmon particle arrays (chapters 3 and 4) and coaxial plasmon waveguides (chapters 6 to 8).

Tunable nanoscale localization of energy on plasmon particle arrays

We demonstrate experimentally that plasmon resonant nanoparticle chains exhibit a nanoscale localized response to unfocused light that can be controlled by tuning the incident wavelength. Confocal microscopy shows that field concentrates on just a few nanoparticles at either the front or back side of the plasmon chains. Our experiments clearly demonstrate that plasmon chains are nanoscale receivers and concentrators of light analogous to multi-element radio wave antennas. This analogy inspires new design rules for many other photonic functionalities, like guiding and redirecting light at the nanoscale.

3.1 Introduction

With the advent of novel techniques to structure materials on the nanoscale, the study of noble metal nanostructures for nanoscale photonics has gained tremendous momentum [1, 2]. The key property of metal nanostructures is that light is coupled to resonant motion of the free electron plasma in the metal, which allows metal nanostructures to enhance and confine electromagnetic fields. Such plasmonic materials are therefore promising for photonic applications in nonlinear optics [40], for the control of optical signals on sub-wavelength length scales [1, 2, 12, 15, 16], but also as biocompatible labels in microscopy [41] and as agents for locally enhanced photothermal medical therapies [42]. To achieve the goal of locally enhancing electromagnetic fields in a controlled fashion, researchers have focused on so-called plasmon antennas [13, 35, 36]. These antennas operate by the local enhancement of electric field near sharp edges of metals, and the strong field that can be generated in narrow gaps between sub-wavelength metal islands.

Chains of coupled resonant metal particles have been proposed by Quinten *et al.* [15] and Brongersma *et al.* [16] to allow transport of confined plasmon excitations from particle to particle at nanometer length scales. An intuitive picture is that waveguiding occurs below the diffraction limit and without radiation loss via instantaneous “quasi-electrostatic” near-field dipole-dipole interactions [16, 43, 44]. Recently, however, several theoretical reports have pointed out that the dispersion relation for such guiding can be phasematched to the dispersion relation of free photons around the arrays, even for arrays with sub-wavelength spacings as small as 75 nm [17, 18, 45, 46]. Around this condition, plasmon nanoparticle chains couple particularly strongly to incident light. Moreover, since interaction between particles occurs via (retarded) far-field contributions, the local response of plasmon chains is expected to be extremely sensitive to the frequency of incident light, due to interference effects [18, 19]. This effect can be used to capture light from an incident plane wave and create strongly localized tunable energy distributions as first proposed by Hernández *et al.* [18]

In this chapter we use confocal microscopy to image the local distribution of electromagnetic intensity near plasmon chains with sub-wavelength spacing in response to illumination along the array axis. The response is not spread out evenly over the entire array, but is located either at the front few particles, or at the backmost particles of the array. The exact distribution can be controlled via the incident wavelength [18]. Such a strong local response to far-field radiation on a single site of an array is equivalent to the response of radio wave antennas, in which an array of resonant scatterers is used to optimize constructive interference for maximum signal on a single electrically connected element [47, 48]. Plasmon

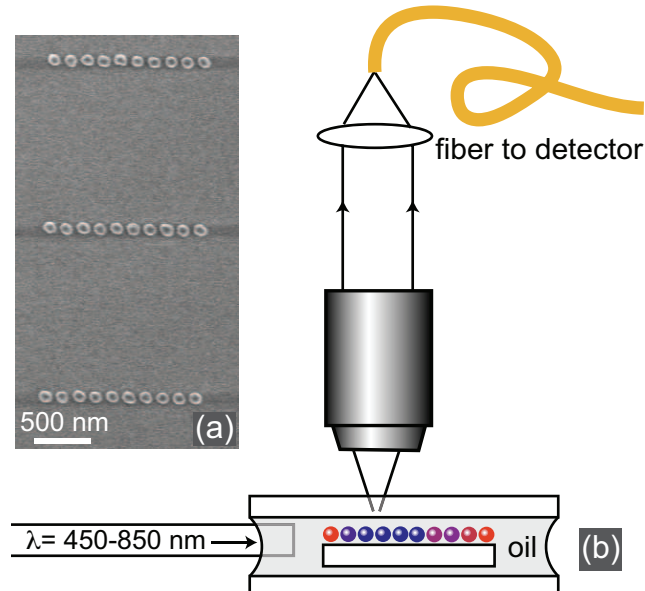


Figure 3.1: Scanning electron-microscopy image of silver nanoparticle arrays and schematic overview of the experimental setup. (a) Finite arrays of silver nanoparticles with a width of 110 nm and height of 50 nm on a substrate of silica, imaged by scanning electron microscopy. (b) Schematic drawing of the experimental setup. The substrate with the nanoparticles is embedded in index matching oil ($n = 1.46$). An optical fiber (core diameter 100 μm) is used to direct the light (bandwidth 5 nm) into the oil layer along the particle chains. The localized optical response of the arrays is probed in a confocal microscope with 60 \times objective (numerical aperture 0.8).

particle chains are equivalent to such multi-element radio wave antennas, apart from the source of the resonance of individual buildings blocks. Whereas in the case of RF antennas, the resonance derives its existence entirely from the scatterer size, in the optical case resonant scattering requires a material resonance. Our work thus demonstrates a new paradigm for nanoantenna design: instead of relying on edges or gaps to create field singularities, one can engineer the interferences in radiative coupling between many resonant antenna elements to efficiently funnel light into a nanoscale spot.

3.2 Experimental

Silver nanoparticle chains were fabricated using electron-beam lithography and lift-off on fused silica substrates. Figure 3.1(a) shows a scanning electron microscopy image of three typical arrays. Each array consists of ten particles with a width of 110 nm and height of 50 nm. The center-to-center distance between adjacent particles within arrays is 150 nm and the arrays are separated by 1.7 μm , at which plasmon interaction between the chains is negligible. Samples were subsequently embedded in index matching oil ($n = 1.46$) and sandwiched between a pair of glass cover slips. A supercontinuum white light source was used to optically excite the nanoparticle chains. A monochromator enabled tuning of the excitation wavelength between 450 nm and 850 nm. Using an optical fiber we guided the excitation beam into the layer of index matching oil embedding the sample, and illuminated the arrays sideways along the array axis (Fig. 3.1(b)). Light that was scattered in the upward direction by the nanoparticle arrays was collected by a microscope objective (60 \times , numerical aperture of 0.8) in an infinity-corrected confocal microscope arrangement. The collected light was focused onto a 25 μm diameter confocal pinhole using a tube lens with focal length $f = 160$ mm, and was subsequently detected by an avalanche photodiode. Two-dimensional confocal images were acquired by simultaneously scanning sample and excitation fiber with a piezoelectrically driven scanning stage.

3.3 Results

Figure 3.2 shows confocal images of the topmost array in Fig. 3.1(a) under irradiation with the excitation beam directed along the array. Incident light travels from left to right in the images. The position of the array is schematically indicated by the circles. Figure 3.2(a) shows the optical response of the array at an excitation wavelength of 600 nm. At this wavelength, most of the scattered light is recorded from the front side of the array, i.e. from the side that is first encountered by the excitation beam. The optical behavior of the array dramatically changes when the wavelength is tuned to 700 nm (Fig. 3.2(b)). Most of the light is now scattered at the back side of the array. These images demonstrate that we can controllably concentrate light on just a few nanoparticles using unfocused illumination at a wavelength close to the single-particle resonance ($\lambda = 650$ nm).

To study the transition of the response that is shown in Fig. 3.2 in more detail, we plot the optical response for multiple excitation wavelengths from 550 to 800 nm in Fig. 3.3(a). The graphs in the figure were obtained by summing the signal

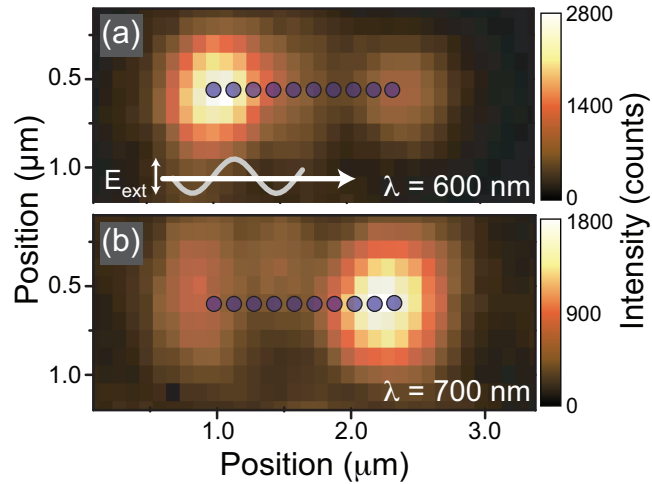


Figure 3.2: Two-dimensional confocal images of an array with ten silver particles (colored circles) that is illuminated from the left along the array axis. (a) For excitation of 600 nm the response localizes on the front part of the array. (b) At 700 nm the back side of array is preferentially excited. Pixel integration time for both images was 50 ms.

along the lateral direction of the recorded confocal images, i.e. perpendicular to the array axis. The curves in Fig. 3.3(a) are all normalized and plotted with an offset for clarity. The figure also depicts the location of the particle array and the propagation direction of the incident light beam. We find that for the shorter wavelengths the front side of the array is preferentially excited, while the back-most particles become preferentially excited at longer wavelengths. The transition between these two regimes occurs abruptly around $\lambda = 675$ nm within a bandwidth much narrower than the plasmon linewidth and when the particle spacing d is equal to about one third of the wavelength in the embedding medium with $n = 1.46$ ($d \sim \lambda/3$).

To analyse these observations we have performed calculations of the field distribution for a chain of ten coupled silver nanoparticles, similar to the model by Hernández *et al.* [18] Optical constants were derived from reference [49]. The model approximates nanoparticles by point-dipoles [17, 18, 45, 46] and yields the dipole moment \mathbf{p} induced on each particle as a function of the incident wavelength. Strictly speaking, the particles in our experiment are oblate, causing a splitting of the single-particle resonance [50, 51]. This splitting can be taken into account by introducing a polarizability tensor, rather than a scalar polarizability

to describe the reponse of individual particles [50]. However, the anisotropy need not be taken into account to analyze our experiment. Based on Ref. [51] we find that the blue-shifted resonance occurs at $\lambda \sim 475$ nm, outside our data set, and that it is an order of magnitude weaker in absolute cross-section than the red-shifted mode. Due to dynamic depolarization, the resonance wavelength of the red-shifted mode almost coincides with that of a plasmon sphere of the same diameter (110 nm). A detailed vectorial analysis of the detection optics [52] further shows that the out-of-plane polarization corresponding to the blue-shifted mode is very inefficiently detected relative to the in-plane polarization corresponding to the red-shifted mode (contrast 1:50). The blue-shifted mode can hence be ignored, and we use the scalar polarizability of a silver nanosphere of the same radius as the oblate semimajor axis.

It is important to realize that phase retardation as well as radiative and non-radiative loss mechanisms are fully taken into account in our point-dipole description. Indeed, phase retardation and interference are crucial for the phenomena in Figs. 3.2 and 3.3: if we only include near-field interactions as in the commonly used quasistatic model [16, 40, 43, 44], we do not observe any asymmetric energy distribution on the array. The calculations were done for plane wave excitation and a refractive index of the surrounding dielectric medium of 1.46. We find a strong localization of the power ($\propto |\mathbf{p}|^2$) on the frontmost sphere for excitation at short wavelengths. In agreement with the experimental results we find that the backmost particle of the array becomes preferentially excited for wavelengths longer than approximately 675 nm. The colored spheres in the bottom and top part of Fig. 3.3(b) show how the dipole moments are distributed over the particles in the chain for the short ($\lambda = 550$ nm) and long ($\lambda = 800$ nm) wavelength case respectively. These calculations show that the power is truly confined to only one or two spheres in the chain at a position that can be tuned through the incident wavelength.

To directly compare the dipole model with the experimental observations we need to account for the microscope collection optics, keeping in mind that radiation from many coherently coupled dipoles within the focus interferes at the confocal pinhole. Therefore we use a vectorial amplitude point spread function [52] to translate the calculated dipole moments into far field intensity profiles (Fig. 3.3(b)), that can be compared to the experimental data in Fig. 3.3(a). We see excellent qualitative agreement between the experimental and calculated data, especially regarding the frequency range of the transition.

For a quantitative comparison we consider the response from the front and back side of the array for wavelengths around the observed transition wavelength (Fig. 3.4). The curves in Fig. 3.4(a) are for the experiment and intersect at a wave-

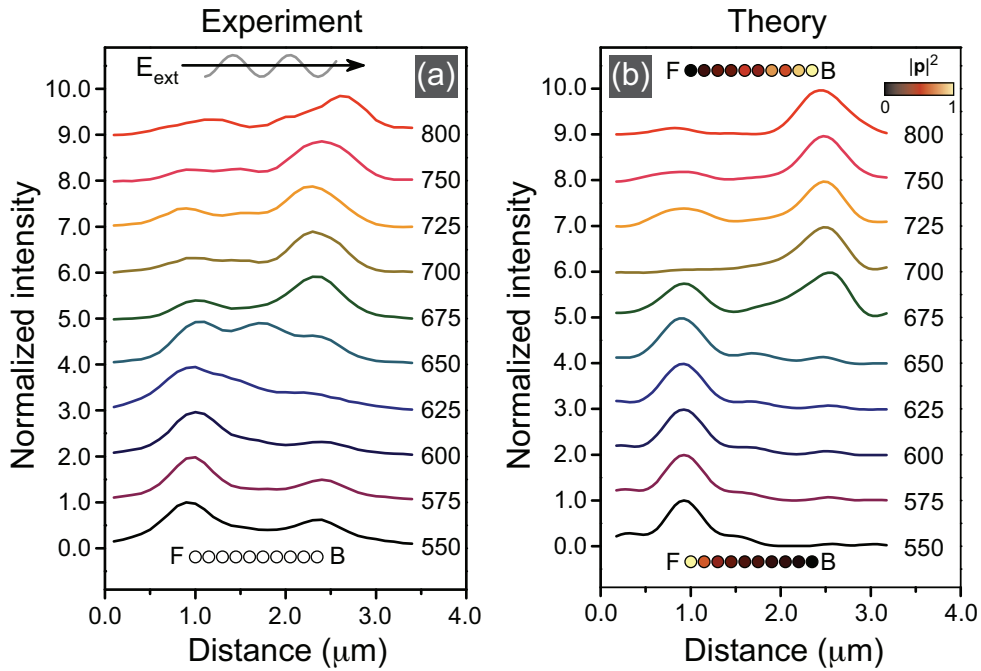


Figure 3.3: Comparison between the measured and calculated optical response of a silver nanoparticle array. (a) Optical response measured for wavelengths from 550 to 800 nm. The curves were obtained by summing intensity maps as in Fig. 3.2 along the lateral dimension, i.e. perpendicular to the array axis. Light travelled from left to right in the image and the position of the array is indicated by the open circles. The localized response is strongest on the front (F) side of the array for wavelengths below 675 nm and strongest on the back (B) side for longer wavelengths. (b) Calculated optical response of the array, obtained using a dipole coupling model, taking into account retardation and (non-)radiative loss, showing similar behavior. The colored circles at the bottom and top of panel (b) show the relative ohmic power on each sphere of the array, for excitation at 550 and 800 nm respectively. In the short wavelength case the energy is confined to the leftmost sphere, while for the longer wavelength the energy localizes on the rightmost spheres.

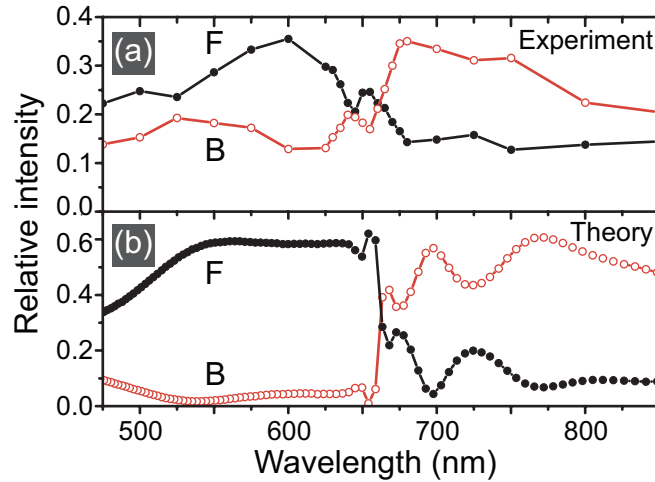


Figure 3.4: Ratio between the optical response from front and back side of the array as a function of wavelength. (a) Relative contribution to the total signal recorded from the front (F, closed circles) and back (B, open circles) of the array. The localized response is obtained by summing of the signal over an area of 500 nm (parallel) \times 1000 nm (lateral) around the front- or backmost sphere of the array, normalized by the integrated signal over the whole array. (b) Calculated relative contributions to the far field intensity by front and back side of the array.

length of about 650 nm, while the calculated curves in Fig. 3.4(b) show a crossover wavelength of approximately 660 nm, very close to the experiment. For wavelengths far away from the intersection point ($\lambda < 550$ nm, $\lambda > 775$ nm) the energy in the chain becomes more delocalized, which causes a reduced contrast between front and back side of the array. Both calculated curves in Fig. 3.4(b) show oscillations in the intensity contrast for excitation wavelengths close to or longer than the crossover wavelength. These variations are not observed in the experimental curves. We attribute this to particle size and position disorder in the array. The silver nanoparticles used in the experiment have a 5% spread in diameter as observed with scanning electron microscopy. Monte Carlo simulations including this level of disorder yield an ensemble averaged crossover wavelength of 668 ± 15 nm. Our calculations also show that the intensity contrast between the front and back side of the array depends on the disorder. For applications the required fabrication accuracy will ultimately depend on the desired functionality.

3.4 Discussion

To understand the response of plasmon particle chains we note a one-to-one correspondence with radio antenna arrays first proposed by Yagi and Uda [47, 48]. Such antenna receivers consist of a single dipole that is electrically connected to read out the radio signal, and that is embedded in an array of regularly spaced scatterers that have a resonant response around the operating frequency. The role of the dipole scatterers is to enhance the signal by optimizing the constructive interference of the incident field and scattered fields at the read-out dipole. For Yagi-Uda antennas signal reception is optimal on the backmost end of the antenna when the spacing is around $\sim \lambda/3$ and when the array points into the source direction, as in our experiment (Fig. 3.2(b)). Since dipole-array antennas rely on the combination of a dipole resonance and optimized geometry for interference, their response is strongly directional and sharply frequency-dependent as in Fig. 3.4. The description of plasmon chains as coupled point-dipole arrays is equivalent to that of dipole array radio antennas, yet downsized to nanometer scale and operating at optical frequencies. There is one important conceptual difference however [44]: while radio engineers need to create a geometrical resonance in the single building-block shape, the single building-block resonance in plasmon arrays requires a resonant material response. Control over the exact resonance frequency, linewidth and polarization anisotropy of single building blocks can be obtained both by changing the material response (i.e., using different metals) and by varying the particle geometry to be, e.g., ellipsoidal or layered in a core-shell geometry, rather than spherical [42, 50]. Plasmon materials are unique in providing the requisite material resonance for sub-wavelength nanoparticles: indeed our model shows that no tunable energy localization occurs for dielectric dots of similar size. Intuitively one might expect that ohmic damping is the main drawback of using a material resonance. However, a Mie calculation shows that for our silver particles the albedo is almost 0.95, implying that 95% of the damping of a single particle resonance is radiative, and only 5% is absorptive. Indeed, removing ohmic damping from our model does not affect either the plasmon resonance linewidth or the energy localization.

3.5 Conclusion

We have shown that the resonant optical response in a metal nanoparticle chain, illuminated with unfocused light, can localize on just a few particles at either the front or back side of the array. By tuning the wavelength of the incident light we

can actively control which side of the array becomes excited. Optimizing field enhancements locally by using arrays of many resonant antenna elements as in this work is complementary to, and can be advantageously combined with current approaches to optical antennas that rely on shape singularities [13, 35, 36]. Finally, we point out that our work invalidates a common design approach in plasmonics: it is the first experiment to invalidate the commonly accepted quasistatic approximation that coupling to far-field radiation is unimportant for sub-wavelength nanoparticle configurations, since energy localization is not observed in the quasistatic model. As a consequence many existing proposals to use sub-wavelength plasmon particle arrays need to be critically reassessed. For instance, our experiment implies that guiding of light below the diffraction is not limited by ohmic damping [16, 43] but by radiative loss [17, 45, 46]. While coupling to radiation can be suppressed for guiding [17], enhancing it also offers exciting new opportunities based on the antenna phenomena demonstrated in our work: this includes many applications in nanoscale optoelectronics, nonlinear optics, sensing, ultrasmall directional light sources and wavelength tuneable nanolithography [19].

Experimental evidence for large dynamic effects on the plasmon dispersion of subwavelength metal nanoparticle waveguides

We present angle and frequency resolved optical extinction measurements to determine the dispersion relation of plasmon modes on Ag and Au nanoparticle chains with pitches down to 75 nm. The large splitting between transverse and longitudinal modes and the band curvature are inconsistent with reported electrostatic near-field models, and confirm that far-field retarded interactions are important, even for $\lambda/5$ -sized structures. The data imply that lower propagation losses, larger signal bandwidth and larger maximum group velocity than expected can be achieved for wave vectors below the light line. We conclude that for the design of optical nanocircuits coherent far-field couplings across the entire circuit need to be considered, even at subwavelength feature sizes.

4.1 Introduction

A fundamental limit to the realization of sub-wavelength (sub- λ) optical devices is that the interaction strength of dielectric objects with light vanishes as the objects get smaller [50, 53]. Plasmonics may allow to overcome this inherent limitation of dielectrics by packing the large polarizability of free electron resonances into a small physical volume [1, 50, 51]. In this framework plasmon particle arrays have been proposed as an ideal platform that combines the ease of controlled nanofabrication with the prospects of creating, e.g., ultra-small antennas to efficiently harvest, enhance and emit optical power [18, 54], as well as a toolkit for nanophotonic circuits [44]. Thus plasmon chains may act as sub- λ width waveguides, waveguide bends, signal splitters, and filters [15, 16, 55–57]. As a parallel development, sub- λ arrays of scatterers with magnetic rather than electric resonances have recently gained tremendous interest for developing optical metamaterials [58].

Pioneering experiments have focused on qualitative understanding of the resonance splitting and mode structure in plasmon particle clusters and arrays [55, 56]. The observed polarization-dependent resonances in linear (1D) particle chains, for instance, correlated well with trends anticipated from a simple near-field quasi-electrostatic model for the chain dispersion relation [16, 57]. This ‘quasistatic’ model, which is valid on deep sub- λ length scales, also formed the basis for forecasting the functionality of more complex structures, such as plasmon chain splitters and multiplexers [16, 44, 59]. Very recently, however, several groups have developed electrodynamic models that predict large quantitative and qualitative deviations from the quasistatic insights [17, 46, 60–63]. If these deviations indeed occur, a redevelopment of general design rules for complex nanophotonic circuits is required to include electrodynamic effects even on small length scales.

So far, quantitative experiments to discriminate between quasistatic and electrodynamic predictions at sub- λ spacings have not been reported. In this chapter we present angle and frequency resolved optical extinction experiments on many arrays of Ag and Au nanoparticles at various particle sizes and sub- λ pitches down to $\lambda/5$. Sub- λ plasmon arrays are an interesting system to test for dynamic effects. Recently, large modifications were predicted for the dispersion of modes in 1D plasmon particle chains and, equivalently, in 1D magnetic split ring resonator arrays [64]. For instance, the deviations include a much larger $k = 0$ splitting between the longitudinal and transverse modes, and a polariton splitting of the transverse dispersion branch at the crossing with the vacuum dispersion relation (light line) [17, 46, 61–63]. For sub- λ waveguiding these models further imply a large increase in group velocity and decrease in propagation loss compared to

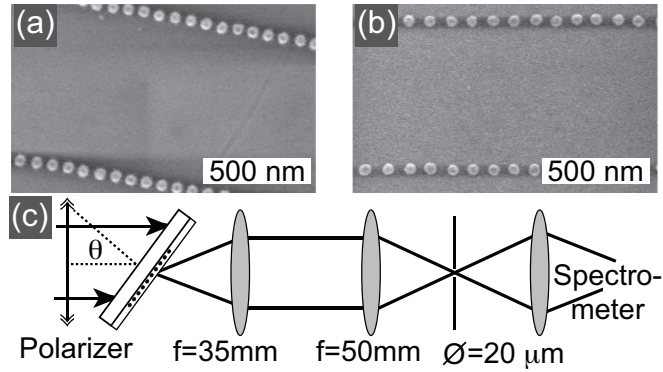


Figure 4.1: (a, b) Scanning electron micrographs of particle arrays on glass with $r = 25$ nm, $d = 75$ nm (a, Au) and $r = 25$, $d = 100$ nm (b, Ag). (c) Overview of the angle-dependent transmission setup. A collimated beam illuminates a large sample area. The sample angle is varied. Light is collected from a small spot on the sample (collection NA= 0.2).

electrostatic predictions [17]. The dispersion relations measured in our experiment agree well with the recent electrodynamic models, and deviate strongly from quasistatic predictions down to pitches as small as $\lambda/5$. As a consequence we anticipate that design proposals for sub- λ nano-optical circuits at currently realistic sizes (~ 50 nm pitch) cannot be based on quasistatic analysis [44], because coherences and coupling across the full structure will dominate the optical performance.

4.2 Experimental

We determine the nanoparticle chain dispersion relation above the light line by far-field extinction measurements on Ag and Au nanoparticle arrays prepared on glass using electron-beam lithography. After physical vapor deposition of Ag or Au and resist liftoff, we obtained linear arrays of particles of 50 nm height, at pitches of $d = 75, 100, 120$ and 150 nm and with radii varied between $r = 25$ and 55 nm, as determined by scanning electron microscopy (SEM, cf. Fig. 4.1(a,b)). The estimated error in determining r is 2 nm. For each pitch the particle radii are below $r/d = 0.37$. We have fabricated square fields containing parallel particle chains (chain length 60 μm), with randomly varying inter-chain spacing (minimum 700 nm, mean 1 μm). The large inter-chain spacing ensures that coupling between chains is negligible, while the random variation suppresses grating effects that occur for

periodic arrangements. Finally, we spin-coat the samples with a 100 nm layer of PMMA to ensure that the particle chains are embedded in a homogeneous dielectric environment. To determine the dispersion relation we use a wavelength-resolved transmission setup (see Fig. 4.1(c)) in which the sample is mounted on a rotation stage (axis perpendicular to the chains, along the PMMA/glass interface) that gives access to incident angles from $\theta = -60^\circ$ to $+60^\circ$. The chains are illuminated by a collimated white-light beam (divergence $\sim 5^\circ$) from a fiber-coupled incandescent source, which illuminates a large (mm-size) area on the sample. Using a pinhole on the transmission side, only the transmitted intensity from a $\sim 15 \mu\text{m}$ spot (associated $\Delta k/k \sim 0.09$ (i.e., 5°)) on the sample is collected by a cooled Si-CCD coupled spectrometer. The transmission is obtained by normalizing the transmitted intensity to that recorded from an unpatterned substrate at the same angle. Using a broadband polarizer, we select the incoming polarization to be either transverse to the chains, or longitudinal (p-polarization). For nonzero θ , the p-polarization also acquires a field-component transverse to the chain.

4.3 Results

Figure 4.2 shows transmission spectra for the full angular range for Ag chains of pitch 150 nm, and radius 45 nm (Fig 4.2(a,c)), and for a smaller pitch of 100 nm and radius 30 nm (Fig 4.2(b,d)). At normal incidence ($\theta = 0^\circ$), a band of extinction around $\lambda = 500$ nm for $d = 150$ nm (470 nm for $d = 100$ nm) is observed for transverse polarization, and at $\lambda = 625$ nm (550 nm for $d = 100$ nm) for longitudinal polarization. The redshift of modes for larger particles is consistent with the well-known single-particle resonance shift with particle size [50, 65]. The occurrence of two bands shifted to either side of the single particle resonance is consistent with earlier reports on the $\theta = 0^\circ$ extinction of nanoparticle chains [55, 56]. Qualitatively this splitting corresponds to the excitation of collective modes in the chain of dipole scatterers: the transverse mode is blue shifted due to the antiparallel orientation of each dipole with the field of its neighbors, while the longitudinal mode is red shifted as each dipole is aligned with the field of its neighbors. For increasing angle-of-incidence, the two branches have opposite curvature, both shifting towards the single particle resonance.

The spectral dependencies of the extinction branches evident in Fig. 4.2 are qualitatively consistent with both the quasistatic model and full dynamic calculations for the dispersion relation of plasmon chain excitations. In order to quantitatively compare the data with the two models, we determine the transmission minima from a Gaussian fit to the transmission spectrum (plotted in the frequency

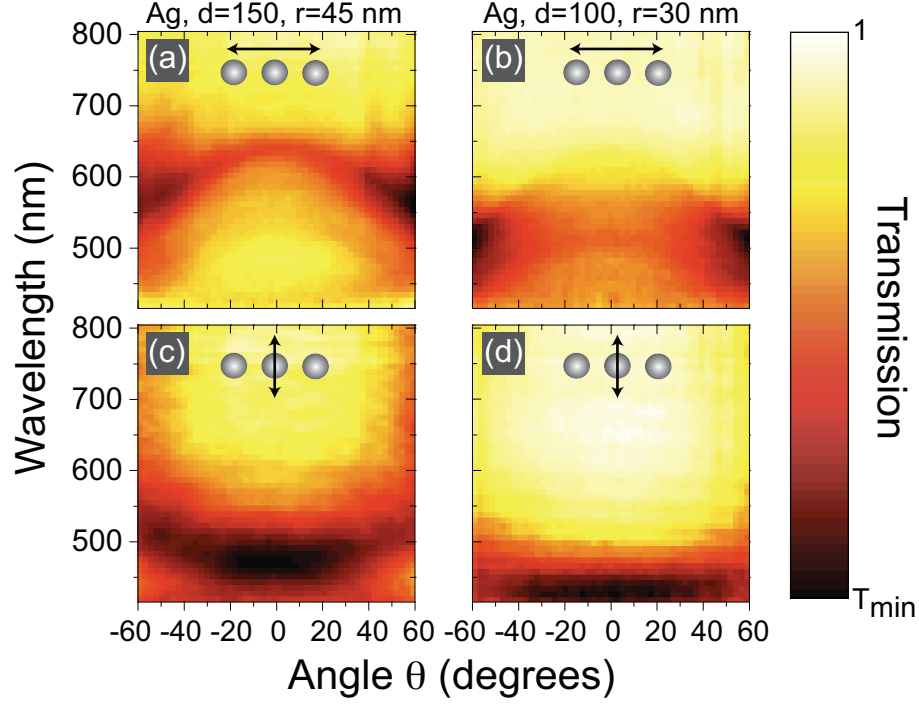


Figure 4.2: Transmission as a function of angle and wavelength for longitudinal (a,b) and transverse polarization (c,d) for Ag arrays with $r = 45, d = 150$ nm (a,c) and $r = 30, d = 100$ nm (b,d). The color scale runs from $T_{\min} = 0.65$ in (a,c) and $T_{\min} = 0.80$ in (b,d).

domain) for each angle. In Fig. 4.3, we plot the resulting center frequencies taken from Fig. 4.2(b,d) as a function of $|\mathbf{k}_{\parallel}| = 2\pi/\lambda \sin(|\theta|)$, i.e. the wave vector component of the incident beam along the chain. The measurements reach up to $k_{\parallel} = 0.86\omega/c$, or up to 60% of the light line in the medium embedding the particles. To appreciate the large width of the extinction resonances, the bandwidth at $1/e$ height of the fitted Gaussians is shaded in the diagram. The typical $1/e$ full width is 2500 cm^{-1} ($\sim 60 \text{ nm}$). First, we compare to the generic quasistatic point-dipole prediction for the nanoparticle chain dispersion relation [16, 55–57]:

$$\omega^2 = \omega_0^2 \left[1 + \left(\frac{r}{d} \right)^3 \sum_{j=1}^{\infty} \kappa_{T,L} \frac{\cos(jkd)}{j^3} \right]. \quad (4.1)$$

Here ω_0 is the single-particle resonance frequency, and $\kappa_T = 2$ for transverse, and

$\kappa_L = -4$ for longitudinal modes¹. We assume spherical particles with r/d taken from SEM data to obtain the quasistatic prediction in Fig. 4.3 (dotted curves). There are two striking discrepancies between the data and the quasistatic model. First, the splitting at normal incidence ($k_{\parallel} = 0$) between the two branches is a factor two to three larger in the data than in the quasistatic model. The quasistatic model even falls outside the broad width of the extinction peaks. Secondly, the quasistatic model predicts that the transverse and longitudinal branch cross at $kd = 0.46\pi$ independent of r/d at a frequency equal to the single-particle resonance. No sign of this crossing is observed in the data. It seems surprising that such discrepancies between data and the quasistatic model haven't been noted in earlier studies [55, 56]. These studies focused on $k = 0$ only, without investigating nonzero scattering angles. On the basis of $k = 0$ data only, one might assume that a larger splitting is due to an error in r/d . For our data, this would imply an unlikely 40% error in estimating r/d . However, even if one would scale r/d to match the $k_{\parallel} = 0$ splitting, the quasistatic model would still not be consistent with the full angle-dependent data set: the presence of the band crossing at $kd = 0.46\pi$ would impose a much larger curvature of both bands than observed in our data.

The fact that the quasistatic model does not describe the data could be due to several approximations: the quasistatic model ignores dynamic effects, multipole effects, the presence of the PMMA-air interface, and particle anisotropy. Based on Ref. [57] we conclude that multipole effects do not resolve the discrepancy between the quasistatic model and our data: multipole effects do not alter the quasistatic dispersion relation for $r/d < 0.35$, a criterion satisfied in our experiment ($r/d = 0.3 \pm 0.02$). For larger r/d , multipole effects in fact reduce the quasistatic $k = 0$ splitting, and shift the band crossing to even smaller wave vectors [57], inconsistent with the absence of a crossing in our data. To study the effect of the dielectric interface, we have analyzed the quasistatic model for dipoles near a dielectric interface using image dipole theory [53]. Within this model the image dipoles have a weaker dipole moment by a factor $(\epsilon_m - 1)/(\epsilon_m + 1)$ (with ϵ_m the embedding dielectric constant) and are located at a distance of 150 nm, i.e., further than the array pitch. As a consequence the estimated increase in splitting is less than 15%, i.e., much less than the 2 to 3-fold enhancement in the experiment. Regarding anisotropy, the particles for which data is reported in Fig. 4.3 are mildly oblate (height 50 nm and diameter 60 nm). At $\theta = 0^\circ$, both polarizations used in the experiment are along equivalent axes of the single-particle polarizability tensor, so that an enhanced splitting is not due to excitation of distinct single-

¹For Drude models of the metal dielectric constant, $\epsilon_{\text{metal}} = \epsilon_b - \eta\omega_p^2/[\omega(\omega + i\gamma)]$, with $\epsilon_b \neq 1$, $\gamma = 0$, κ is reduced by $[3\epsilon_m/(\epsilon_b + 2\epsilon_m)] \approx 0.66$ for Ag in glass.

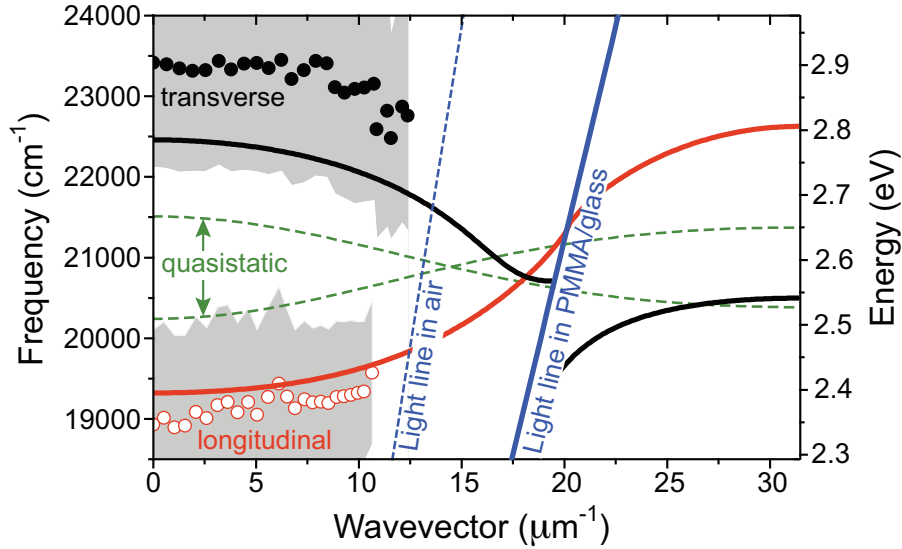


Figure 4.3: Symbols: frequency (in cm^{-1} (left axis) or eV (right axis)) of minimum transmission versus wave vector for transverse and longitudinal polarization in Fig. 4.2(b,d), i.e. the $d = 100$ nm, $r = 30$ nm Ag particles. Shaded areas: $1/e$ bandwidth of the transmission minima. Straight lines: light lines in air and in the embedding medium. Thick (thin) curves: dynamic (static) prediction.

particle resonances. In addition, we calculated the polarizability tensor (including dynamic depolarization shifts [51, 65]). The resonance relative to that of a $r = 30$ nm spherical particle is only shifted by 4 nm, and the on-resonance polarizability along the long axes is in fact 10% smaller. Within the quasistatic model, particle anisotropy is hence expected to reduce the splitting, rather than explaining the observed enhancement.

Having excluded that modifications to the quasistatic model due to multipole effects, interface corrections or particle anisotropy can explain the dispersion relation observed in the experiment, we now compare the data to a full electrodynamic point-dipole model [17] that includes Ohmic damping, radiation damping, and depolarization shifts in the single-particle polarizability [65], as well as all terms in the dipole field. Within this model the dispersion relation has recently been calculated perturbatively [45, 62], and self-consistently for finite [46] and infinite

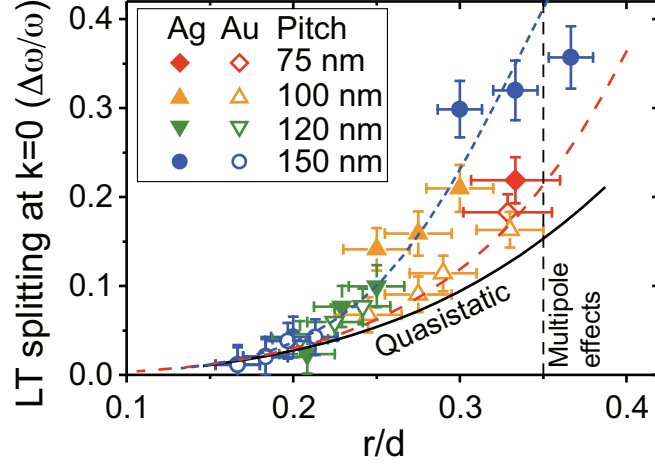


Figure 4.4: Symbols: Relative splitting between transverse and longitudinal branch at $k = 0$ versus r/d for several pitches d as indicated for Ag and Au arrays. Black curve: quasistatic prediction for Ag arrays. Colored curves: dynamic predictions for $d = 75$ nm (Ag, dashed) and $d = 150$ nm (Ag, dotted). Multipole effects set in beyond the dashed vertical. [57]

arrays [17, 63]. Using a dielectric model for silver that is a modified Drude fit² to tabulated data [49], and taking r and d from SEM observations, we plot the self-consistent infinite array model as solid curves in Fig. 4.3. This model predicts a band splitting at $k = 0$ that is approximately twice the splitting in the quasistatic model for the same geometrical parameters, as well as a band curvature for wave vectors away from $k = 0$ that is in much better agreement with the experimental data. Keeping in mind that the dynamic model has no adjustable parameters, the reasonable correspondence with the data is a strong indication that retardation effects and far-field coupling are indeed determining the dispersion relation for $d = 100$ nm silver nanoparticle chains. The remaining deviation from the dynamic model may yet again be due to the small particle anisotropy, the PMMA-air interface, or multipole effects [60] the influence of which is much more difficult to estimate quantitatively for electrodynamic rather than quasistatic models.

Based on the data in Figs. 4.2 and 4.3 we conclude that the large splitting between the transverse and longitudinal branch at normal incidence compared to the quasistatic prediction is a good indicator for the relevance of far-field effects.

²We fit optical data in [49] using $\epsilon_{\text{metal}} = \epsilon_b - \eta\omega_p^2 / [\omega(\omega + i\gamma)]$. For silver, $\epsilon_b = 5.45$, $\eta = 0.73$, $\omega_p = 1.72 \cdot 10^{16} \text{ s}^{-1}$ and $\gamma = 8.35 \cdot 10^{13} \text{ s}^{-1}$.

Figure 4.4 shows the measured relative splitting $\Delta\omega/\omega$ for many combinations of particle radius r and pitch d plotted against r/d , both for Ag and Au particle arrays. In the quasistatic limit, the splitting is simply proportional to $(r/d)^3$ (see Eq. (4.1)). In the dynamic model, the splitting depends on r and d separately as is clear from the dynamic predictions for the smallest ($d = 75$ nm) and largest ($d = 150$ nm) pitch used in our experiments (dashed/dotted in Fig. 4.4). Figure 4.4 demonstrates that for Ag particles the splitting is generally a factor ~ 2 larger than quasistatic theory predicts, in agreement with the dynamic model. For Au particles, the difference is not as large, which may explain why previous studies did not resolve deviations from quasistatic theory [55, 56]. Still, the observed splittings for Au systematically exceed the quasistatic prediction. We attribute this smaller effect for gold to the much lower albedo ($\leq 20\%$ for $r = 25$ nm Au, compared to $\sim 80\%$ for Ag) [50]. Since low-albedo particles radiate less strongly, far-field corrections to the dispersion relation will be less important.

4.4 Conclusion

The experiment reported in this chapter shows that the dispersion relation for plasmon modes on sub- λ metal chains is strongly modified by far-field interactions, even for pitches as small as $d = 75$ nm or $\sim \lambda/5$. This experiment thus confirms recent models [17, 45, 46, 62, 63] that overturn the quasistatic view on plasmon chains [16, 57]. The next challenge is to address wave vectors below the light line, for which propagation distances up to 5–10 μm at group velocities around $0.3c$ are feasible [17]. These propagation distances far exceed initial estimates, which were based on the damping rate of single particles [16, 55, 56]. Below the light line, the damping rate is strongly reduced since far-field destructive interference suppresses all radiative loss. It will be a challenge to excite these wave vectors selectively: local excitation, *e.g.* at a waveguide entrance, will excite wave vectors both below and above the light line. Recent simulations confirm that retardation effects are very important for local excitation of finite sub- λ plasmon chains, giving rise to a complex and strongly frequency dependent response [18]. However, interpretation in terms of superpositions of modes above and below the light line is nontrivial, since depending on the excitation either the dispersion relation for real k and complex ω , or for complex k with real ω applies, as discussed in Ref. [17]. As the complexity is increased to include 2D clusters, we expect far-field effects to become even stronger [60]. Therefore, our work implies that an essentially quasistatic electric circuit-design approach [44] to nanophotonics is only applicable to structures of total size below ~ 50 nm, *i.e.*, a scale at which fab-

4 Plasmon dispersion in metal nanoparticle waveguides

rication of several coupled components is extremely challenging. Sub- λ photonic structures at the current fabrication limit will always require a fully electrodynamic optimization of the coherent coupling between all building blocks: far-field interference is key to optimize the functionality and reduce the loss.

Observation of plasmon modes in Au nanowires using high-resolution cathodoluminescence imaging spectroscopy

We use cathodoluminescence imaging spectroscopy to excite and investigate plasmonic eigenmodes of Au nanowires with lengths of 500–1200 nm and ~100 nm width. We observe emission patterns along the Au nanowire axis that are symmetric and strongly wavelength dependent. Different patterns correspond to different resonant modes of the nanowire. From the observed patterns we derive the spatial and spectral properties of the wire eigenmodes and determine the dispersion relation for plasmonic Au nanowire modes.

5.1 Introduction

The ever-increasing speed and decreasing size of electronic circuits will meet fundamental limits in the near future. Integration of electronics with optics is promising because optical components can provide a very high bandwidth. However, a simple downscaling of conventional optics to nanometer scale is not possible due to the diffraction limit, hindering true nanoscale applications. Surface plasmon polaritons (SPPs) are electromagnetic waves that are strongly coupled to electron plasma oscillations at a metal-dielectric interface. They are characterized by a dispersion below the light line, enabling reduced wavelengths at optical frequencies [1, 66]. Moreover, they are strongly bound to the metal surface leading to high lateral confinement. SPPs propagating along metal nanowires therefore allow photonic manipulation below the diffraction limit.

At small length scales, metal nanowires with finite length behave as plasmonic cavities with resonant eigenmodes [67]. Properties of metal nanowire plasmon resonances have been investigated by extinction measurements on large ensembles [67, 68]. To study the nature of the resonances in greater detail, individual wires have been investigated using scanning near-field optical microscopy (SNOM) [21, 22]. With SNOM however, one is still limited in resolution by the size of the tip (> 50 nm). Furthermore, the tip proximity can have a very strong influence on the optical behavior of the sample [23, 69].

Here we study photonic properties of metal nanowires at high resolution using electron radiation. The electron beam generates a broad spectrum of SPPs, which can subsequently generate cathodoluminescence (CL) radiation that can be detected [70–72]. In this chapter, we use CL imaging spectroscopy for direct observation of plasmonic nanowire modes and determine both spectral and spatial properties of plasmonic eigenmodes. Based on the data we determine the dispersion relation of SPPs on the Au nanowires.

5.2 Experimental

Au nanowires were fabricated on a doped silicon substrate using electron beam lithography and lift-off. Figure 5.1(a) shows a scanning electron micrograph of a nanowire specimen. The nanowire width is ~ 100 nm and the length is 725 nm. Additional nanowires were fabricated with lengths in the 500–1200 nm range. The nanowires were separated by $5 \mu\text{m}$, so that no interaction between wires is expected. The silicon provides a highly conductive substrate avoiding charging during electron beam irradiation, but does give a weak CL background signal that is

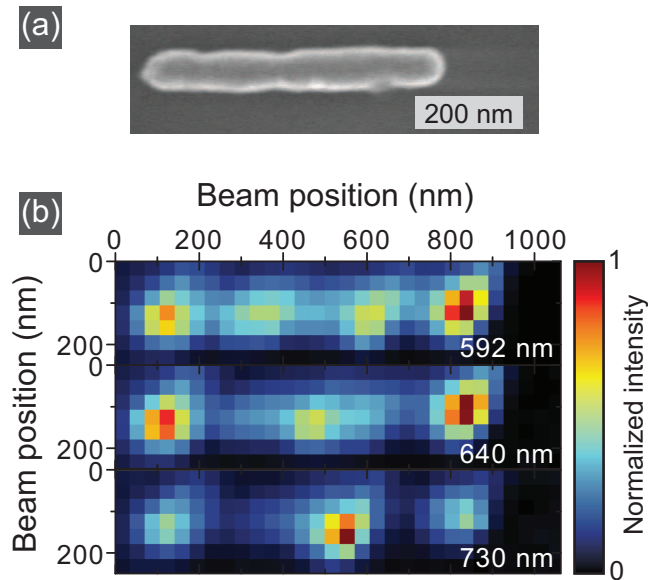


Figure 5.1: (a) Scanning electron micrograph of a 725 nm long Au nanowire on a Si substrate, fabricated using e-beam lithography. Scalebar is 250 nm. (b) Cathodoluminescence images of the Au nanowire, at wavelengths of 592, 640 and 730 nm. The light emission pattern is strongly wavelength dependent, indicating excitation of different plasmonic modes.

subtracted from the data.

CL spectroscopy was performed in a scanning electron microscope (SEM) extended with a Gatan ParaCL cathodoluminescence system. The electron beam (30 kV, waist < 5 nm) is sent through a hole in a parabolic mirror that is mounted above the substrate. The mirror collects light that is emitted from the sample within a large opening angle of 1.4π sr, and collimates it into a spectrometer that is equipped with a CCD detector with a 1340×100 pixel array, recording spectra in the 390–950 nm wavelength range.

5.3 Results

Figure 5.1(b) shows the result of spectral collection during an electron beam scan of a 725 nm long Au nanowire (SEM image in Fig. 5.1(a)). The electron beam was scanned in 7 rows and 30 columns and for every pixel a spectrum was collected. The figure shows emission in three wavelength windows from this scan, around

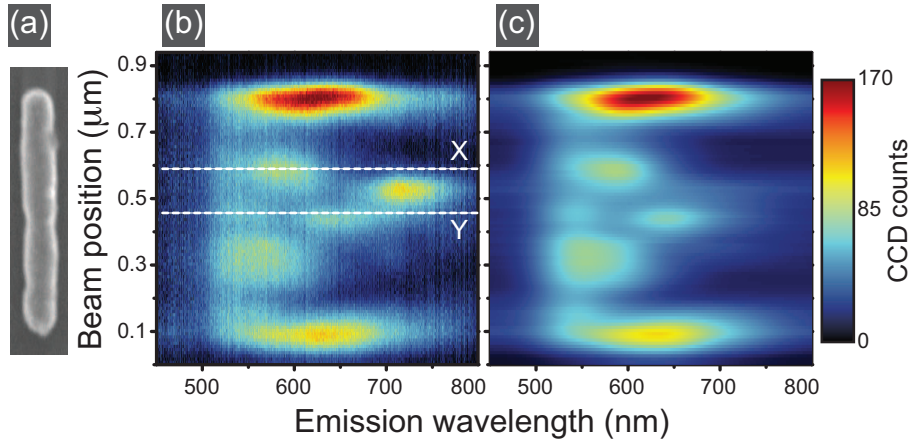


Figure 5.2: (a) SEM image of the Au nanowire. (b) Cathodoluminescence spectral line scan along the axis of a 725 nm long and ~ 100 nm wide Au nanowire on Si. For every beam position (vertical axis), a spectrum is plotted (horizontal axis). The lines X and Y indicate the position at which the spectra that are plotted in Fig. 5.3 are taken. (c) Reconstruction of the line scan image from the fit results, showing that the 4 resonant mode spectra that have been used, represent all resonances of the wire. The artifact in (b) around 730 nm was removed before fitting, because it does not correspond to a geometric resonance.

592, 640 and 730 nm. For 592 nm we observe a pattern of 4 maxima, while for 640 and 730 nm 3 maxima are observed. These images demonstrate that the electron beam can excite multiple resonances on the wire, that each have a specific spatial profile.

For a more detailed investigation of the data in Fig. 5.1, the electron beam was scanned along the wire axis, and for every beam position spaced by 14 nm a spectrum was collected (see Fig. 5.2(a) for a SEM image). The result of this scan is shown in Fig. 5.2(b). The spectral axis is plotted horizontally and beam position is plotted vertically. The color scale indicates the recorded intensity. Before further analysis, we remove from the dataset the peak around wavelength 730 nm and position $0.53 \mu\text{m}$ using a two-dimensional Gaussian fit¹.

Figure 5.3(a) shows the CL spectra for two positions on the wire, that are indicated by X and Y in Fig. 5.2(b). Gaussian fits are performed on these data and show for spectrum X predominant contributions of the resonances peaking at 540 nm

¹We assume that this spot originates from a resonance that is related to an irregularity on the wire rather than a geometric plasmon resonance. Indeed, the irregularity is observed in the SEM image (see Fig. 5.2(a))

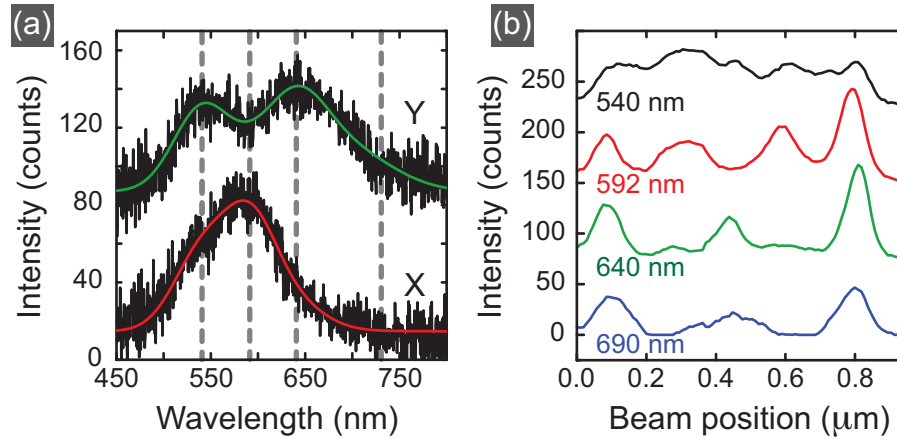


Figure 5.3: (a) CL spectra taken at two different positions along a 725 nm long Au nanowire (black curves). X and Y correspond to positions as indicated in Fig. 5.2(b). Also plotted in the figure are fits (green and red curves) to these data by a set of 4 Gaussian resonances at center wavelength of 540, 592, 640 and 690 nm, indicated in the figure by vertical dotted lines. (b) Fitted intensity of each resonance plotted as a function of electron beam position. The 640 nm and 690 nm modes show three maxima, the 592 nm mode shows four maxima and five maxima are vaguely observed for the 540 nm mode.

and 592 nm, while spectrum Y is made up mostly by the 540 nm and 640 nm resonance. The fitted spectral widths are in the range 40–70 nm, corresponding to a characteristic cavity Q of ~ 10 .

Figure 5.3(b) plots relative contributions of each resonance at every position on the nanowire. Three clear maxima are observed along the wire for the 640 nm and 690 nm resonances; 4 maxima are observed for the 592 nm resonance, and — less pronounced — 5 maxima are seen for the shortest-wavelength resonance at 540 nm. To verify the quality of the analysis, the line scan data in Fig. 5.2(b) were reconstructed by convoluting the four resonance spectra with the spatial profiles. This reconstruction is drawn in Fig. 5.2(c) and shows that the 4 resonances provide a good representation of the data.

For a further analysis, we treat the nanowire resonances as organ-pipe like modes, i.e. interfering SPPs travelling in opposite directions that reflect at the wire ends. Furthermore, we assume that the CL emission spectrum from the sample is directly related to the intensity of different eigenmodes at the spot of the electron beam. [70, 73, 74]

In this picture, the distance between two intensity maxima in the profiles of

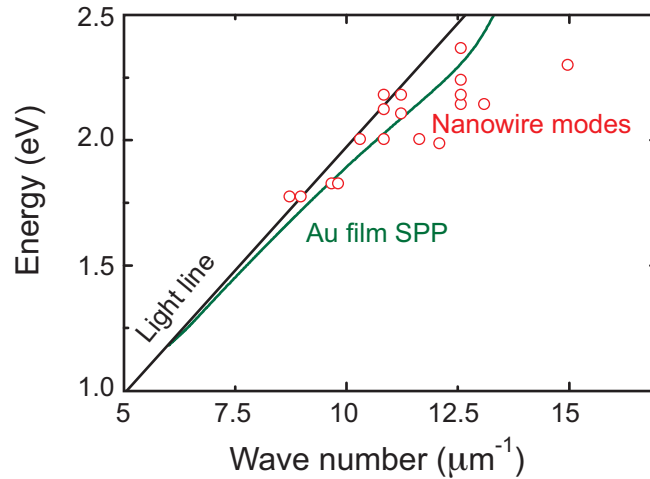


Figure 5.4: Experimentally determined dispersion of surface plasmon modes on Au nanowires with different lengths (circles). Dotted line: light line in vacuum. Solid line: dispersion relation of a SPP on an infinite Au film.

Fig. 5.3(b) corresponds to $\lambda_p/2$, where λ_p is the SPP wavelength. For a wave in a dispersive medium, with complex index of refraction, there is a nontrivial phase shift upon reflection from the wire end, that can be wavelength dependent. For this reason we only determine λ_p from peaks within the wire, to avoid the effect of this phase shift.

From the data in Fig. 5.3(b), and additional measurements on Au nanowires with different lengths in the 700–1200 nm range, several values for λ_p were determined for the corresponding resonance wavelength.

Combining the resonance energy with the corresponding SPP wavelength (λ_p) yields a data point of the dispersion relation of SPPs on a Au nanowire. Dispersion data for all measurements are plotted in Fig. 5.4. The SPP dispersion for a planar Au film as well as the vacuum light line are also plotted. As can be seen in Fig. 5.4, the wire modes are close to the dispersion relation for SPPs on a Au-vacuum interface.

Finally we note that the spatial profiles in Fig. 5.3(b) for 640 and 690 nm are quite similar. This is possibly due to the fact that the wires are not embedded in a homogeneous medium, but are fabricated on top of a silicon substrate, which may cause splitting of wire resonances. More work is required to investigate this in greater detail.

5.4 Conclusion

We have used cathodoluminescence imaging spectroscopy to observe the plasmonic behavior of gold nanowires. We show that Au nanowires behave as plasmon resonators, with eigenmodes with distinct spatial profiles. The simultaneous measurement of spectral and spatial characteristics of the modes allowed us to determine the dispersion of SPPs on Au nanowires.

Plasmon dispersion in coaxial waveguides from single-cavity optical transmission measurements

We determine the plasmon dispersion relation in coaxial waveguides composed of a circular dielectric channel separating a metallic core and cladding. Optical transmission measurements are performed on isolated coaxial nano-apertures fabricated on a Ag film using focused ion-beam lithography. The dispersion depends strongly on the dielectric material and layer thickness. Our experimental results agree well with an analytical model for plasmon dispersion in coaxial waveguides. We observe large phase shifts at reflection from the end facets of the coaxial cavity, which strongly affect the waveguide resonances and can be tuned by changing the coax geometry.

6.1 Introduction

In only a few years time the rapidly growing field of plasmonics has generated a large array of new nanophotonic concepts and applications. The ability of metal nanostructures to localize light to sub-wavelength volumes [13, 54, 75] has provided opportunities for e.g. sensing applications [11] and nanoscale optical lithography [19, 76]. Plasmonics also provides a way to finely tailor the dispersion relation of light, giving the ability to shrink the wavelength of light down to only a few tens of nanometers at optical frequencies [77], or create materials with negative index of refraction [33]. Possible applications where precise control of the optical dispersion is essential range from true-nanoscale optical components for integration on semiconductor chips to lenses for sub-wavelength imaging [33, 78] and invisibility cloaks [28, 79].

Recently, coaxial plasmon waveguides with a circular dielectric channel separating a metallic core and cladding, have received a great deal of attention in connection to observed enhanced transmission from 2-dimensional arrays of coaxial nanoapertures at infrared wavelengths [80–82]. The transmission enhancements have been ascribed to standing optical waves along the axis of the coaxial apertures [24, 83, 84]. Past studies have been limited to short (< 200 nm) coaxial channels, allowing observation only of the lowest order resonances [80–82]. Furthermore, optical transmission has only been measured for arrays of coaxial waveguides, making it hard to separate transmission enhancements owing to channel resonances from enhancements related to collective resonances of the array [80–82, 85]. To investigate the optical resonances of coaxial waveguides in detail, measurements on single coaxial nanostructures are necessary. Furthermore, a systematic study is needed of the phase shifts upon reflection from the waveguide ends, as they strongly affect the resonances of a short waveguide.

Here, we report optical transmission measurements of isolated coaxial plasmon waveguides in Ag with systematically varied lengths in the range 265–485 nm. By varying the channel length the dispersion relation for these structures was determined for the first time. The experimental results agree well with an analytical model for plasmon dispersion in coaxial waveguides. We observe a significant enhancement of the wave vector of light when coupled to coaxial waveguides from free space, even at frequencies well below the surface plasmon resonance. It is found that the phase shift upon reflection off the waveguide ends can be tuned by changing the waveguide geometry. We anticipate that the combination of strong optical confinement and relatively low propagation loss make coaxial waveguides very promising as nanoscale optical components.

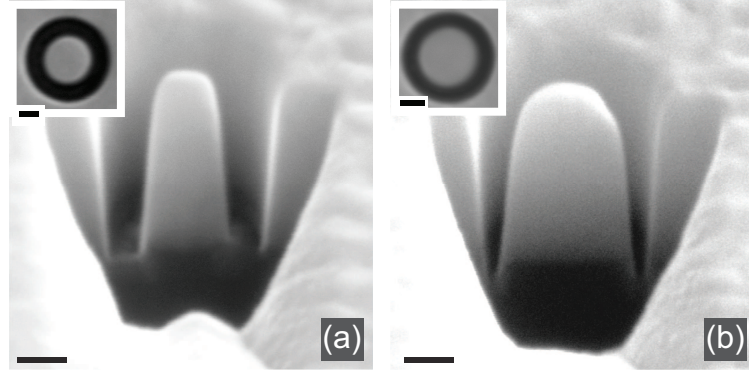


Figure 6.1: SEM images of the cross-sectional profile of coaxial plasmon waveguides with lengths of 485 nm and widths of ~ 100 nm (a) and ~ 50 nm (b) and outer radii of ~ 175 nm. The insets show top view SEM images of the waveguides before cross-sectioning. Scale bars are 100 nm.

6.2 Experimental

The plasmon dispersion in coaxial waveguides was determined from transmission measurements of isolated coaxial channels prepared using focused ion beam (FIB) milling on films of Ag. Ag was deposited by thermal evaporation on quartz substrates. The Ag thickness was varied between 265 and 485 nm in 20 nm increments using a shutter. We fabricated coaxial waveguides by FIB milling 20–100-nm-wide circular channels through the Ag layer. Figure 6.1 shows scanning electron microscope (SEM) images of 485-nm-long coaxial channels with an outer radius of ~ 175 nm and channel widths of ~ 100 nm (a) and ~ 50 nm (b). The main panels in Fig. 6.1 were taken at a 55-degree angle with respect to the sample normal after a cross-section was made using FIB milling. The images display a small degree of tapering of the channels ($\sim 7^\circ$ taper angle), which is mainly caused by re-deposition of Ag in the waveguide during FIB milling, an effect that becomes more pronounced deeper in the Ag layer. The insets in Fig. 6.1 are top-view SEM images of the coaxial channels that show excellent uniformity of the channel radii and width. Coaxial channels were separated by $50 \mu\text{m}$ to avoid coupling between waveguides.

To investigate the influence of channel length and width on the optical response of coaxial waveguides we performed optical transmission measurements. Radiation from a supercontinuum white light source was focused onto individual coax structures using a 0.95 NA objective. The transmitted light was collected by a 0.7 NA objective and directed into a spectrometer equipped with CCD detector

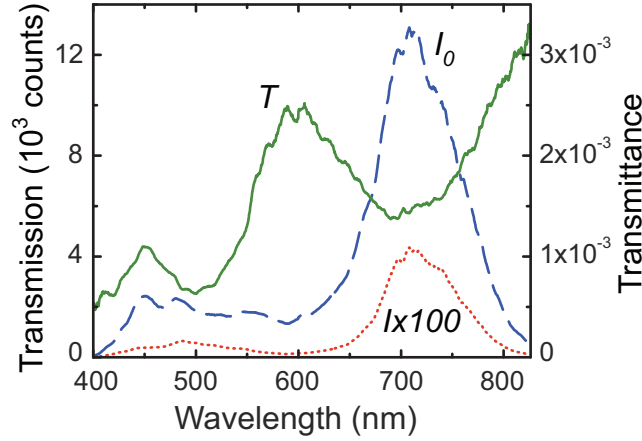


Figure 6.2: Transmission measurement (red dotted spectrum, I multiplied by 100) of a coaxial waveguide with ~ 100 -nm-wide dielectric channel and length of 485 nm (see Fig. 6.1b) and a reference spectrum (blue dashed line, I_0). The transmittance defined as the waveguide transmission spectrum divided by the reference spectrum is depicted by the green curve (green drawn line, T).

to measure optical spectra. For reference, we measured transmission spectra of $10 \times 10 \mu\text{m}$ open squares in which the Ag layer had been completely removed by FIB milling.

6.3 Results

Figure 6.2 shows transmission spectra of a 100-nm-wide, 485-nm-long coax channel (I) and of a reference area close to the waveguide (I_0). The transmittance spectrum ($T = I/I_0$) is obtained by normalizing the waveguide transmission to the reference spectrum and is also shown in the figure. Three distinct maxima can be resolved in the transmittance spectrum, at ~ 450 nm, ~ 600 nm and >820 nm, which we attribute to Fabry-Perot cavity resonances of the coaxial waveguide. To corroborate this hypothesis we have measured the transmittance of a series of coaxial waveguides of equal channel width but varying channel lengths.

Figure 6.3 shows transmittance spectra of 100-nm wide coaxial channels with length decreasing from 485 nm (same data as in Fig. 6.2) to 265 nm in 20 nm increments. Several features are observed. First, the resonance at 600 nm for the longest waveguide gradually blue-shifts to 450 nm for the shortest waveguide. Also, the resonance at 450 nm, observed for the largest channel length, blue-shifts

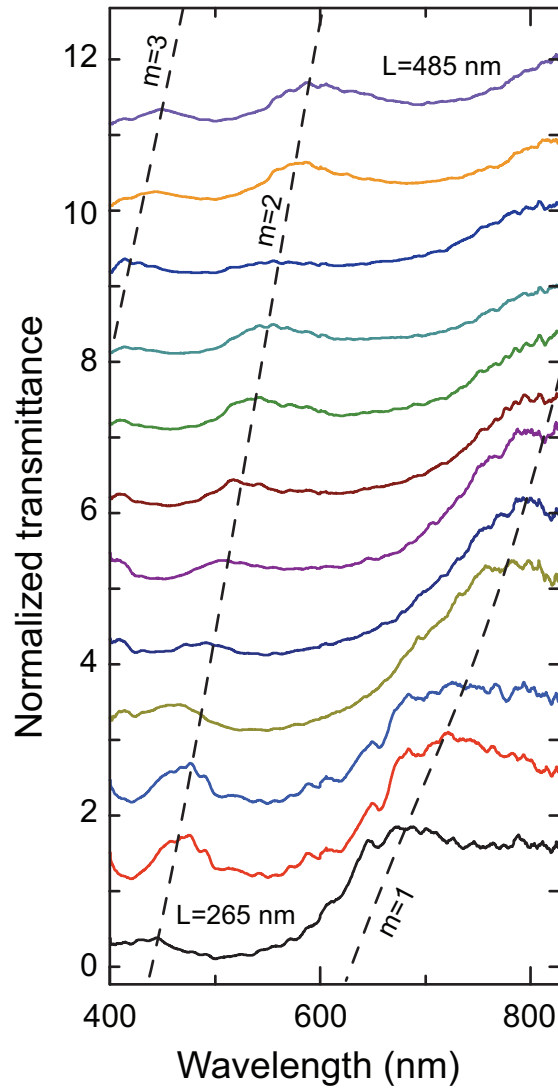


Figure 6.3: Transmittance spectra of coaxial waveguides with varying lengths. The outer radius and channel width were ~ 175 nm and ~ 100 nm respectively, while the waveguide length was decreased from 485 nm (top curve) to 265 nm (bottom curve) in increments of 20 nm. Data are shifted vertically for clarity. The black dashed lines are guides for the eye and connect the resonance peaks ($m = 1-3$).

to a wavelength below 400 nm for waveguides shorter than 400 nm. The broad peak in the long-wavelength range of the spectra also blue-shifts as the length of the cavity is decreased, showing a main peak at a wavelength of 650 nm for the shortest waveguides.

Fabry-Pérot resonances result from interference between forward and backward propagating plasmon waves in the cavity. On resonance, the condition,

$$|2Lk_{SPP}(\omega) + \Delta\phi_1 + \Delta\phi_2| = 2\pi \times m \quad (6.1)$$

must be fulfilled, with L the length of the waveguide, $k_{SPP}(\omega)$ the wave vector of the plasmon at frequency ω , $\Delta\phi_{1,2}$ the phase shifts as a result of plasmon reflection at either end of the waveguide, and m the mode number.

Before we can determine the plasmon dispersion in coaxial waveguides it is necessary to assign mode numbers to the measured Fabry-Pérot resonances. With this in mind, we performed exact calculations of $k_{SPP}(\omega)$ by solving Maxwell's equations for a cylindrical structure of infinite length [24, 83, 86–88]. The azimuthal dependence of the electric and magnetic fields in the waveguide is described by the harmonic function $e^{in\psi}$ of order n . Note, that we expect to only excite modes of odd azimuthal order in the experiment as the incident electric field has even parity about the center of the waveguide aperture. The radial dependence of the fields in all three domains (Ag-dielectric-Ag) is described by solutions to the 2^{nd} order Bessel differential equation. We apply a Bessel function of the first kind, J_n , to the Ag core and a Hankel function of the first kind, $H_n^{(1)}$, to the Ag cladding. Inside the dielectric channel the radial field dependence is described by a linear combination of Bessel and Hankel functions of the first kind. On each domain boundary we formulate four continuity conditions for the tangential components of the electric and magnetic fields. The optical eigenmodes of the coaxial waveguide are found when the determinant of the resulting homogeneous system of eight equations with eight unknown coefficients vanishes.

In this way dispersion relations were determined for waveguides of any chosen channel width. To account for the tapered profile of the resonators in the experiment we calculated the effective dispersion relation by index-averaging $k_{SPP}(\omega)$ over a series of dispersion curves corresponding to the varying lateral dimensions of the waveguide determined from SEM images (Fig. 6.1). By inserting this index-averaged dispersion into equation (6.1) we obtain the resonance frequency as function of cavity length and mode number m . We compared these results to experimental values of the resonance frequency, obtained by fitting the transmittance spectra with Lorentzian line shapes, as function of waveguide length. This comparison makes it possible to assign mode numbers to the measured resonances and construct the plasmon dispersion relation for the

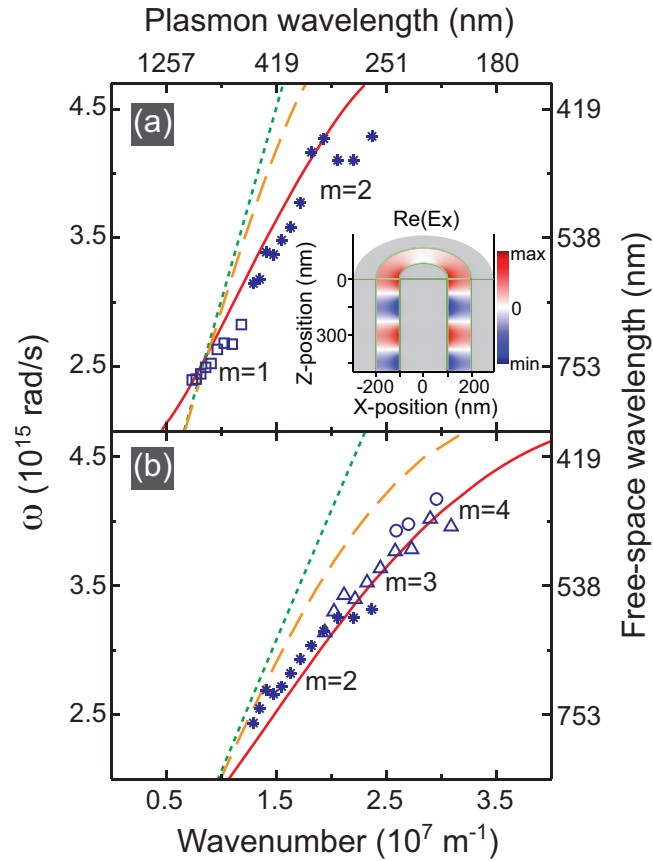


Figure 6.4: Measured dispersion data and calculated index-averaged dispersion relations (red drawn lines) for coaxial plasmon waveguides with (a) ~50-nm-wide air channel and (b) ~50-nm-wide spin-on-glass (SOG) filled channel. Light lines for air (a) and SOG (b) are also shown (dotted green lines), along with the plasmon dispersion (dashed orange curves) at a flat Ag/air interface (a) and Ag/SOG interface (b). Symbols in the figure correspond to different Fabry-Pérot mode numbers, m , where $\square = 1$, $*$ = 2, $\triangle = 3$, $\circ = 4$. The inset in (a) shows the calculated electric field distribution of the mode of azimuthal order $n = 1$, in a SOG-filled coaxial waveguide with outer radius of 200 nm and channel width of 100 nm at $\omega = 3.5 \times 10^{15}$ rad/s.

coaxial waveguides. In a first analysis we assume that the plasmon phase shift upon reflection at the cavity ends, which will be discussed further on, is zero.

Figure 6.4(a) shows the dispersion data for coaxial channels with an average outer diameter of ~ 175 nm and ~ 50 -nm-wide air channel (see Fig. 6.1(b)) along with the calculated dispersion curve for azimuthal order $n = 1$, taking into account the tapering in the structures as determined from SEM data (Fig. 6.1). Good agreement between experiment and calculations is observed. Different symbols indicate measured resonances characterized by mode numbers, $m = 1$ and 2. Dispersion in air and at a Ag/air interface are plotted for reference. The figure shows up to $\sim 60\%$ larger wave vectors in coaxial waveguides compared to free space. At lower frequencies ($\omega < 2.5 \times 10^{15}$ rad/s) the calculated dispersion relation flattens slightly and crosses the air light line, in agreement with experimental data in that frequency range.

To further increase the dispersion, we have filled the coaxial nanostructures by spin-coating the sample with a ~ 200 -nm-thick layer of spin-on-glass (SOG, $n = 1.46$). SEM of FIB-milled cross-sections confirmed that SOG in-filled the structures entirely. Figure 6.4(b) shows the dispersion data for in-filled coaxial waveguides of the same dimensions as in (a). In this case resonances with mode numbers $m = 2-4$ were observed. We further note a shift of the dispersion data to higher wave numbers compared to the air case of Fig. 6.4(a), as well as a clear increase in the curvature of the dispersion relation. In this case we observe up to ~ 2.2 times larger wave vectors in coaxial waveguides compared to free space. Figure 6.4(b) also shows the calculated plasmon dispersion (red drawn curve).

Thus far we have demonstrated cases where the calculated dispersion relations match the experimental data quite well. Figure 6.5(a) compares the dispersion data and calculated dispersion relation (red drawn curve) for air-filled waveguides with a dielectric channel width of ~ 100 nm. Although the data follow the same general trend as the calculated curve the two show a clear offset in wavenumber with respect to each other. In the final part of this letter we will show that the observed discrepancy between the data and theory results from a net phase shift ($\Delta\phi_1 + \Delta\phi_2$) that the plasmons gain when they reflect off the cavity ends, which can be tuned by changing the cavity geometry.

As equation (6.1) shows, a nonzero net phase shift causes the resonance wavelengths to shift. To study the phase shift we have performed finite difference time domain (FDTD) simulations to obtain the field profile in structures similar to those used in the experiment. In the simulations we used a linearly polarized broad-band optical pulse to excite the structures. By applying a discrete Fourier transform of the time-dependent fields we obtain the spatial field intensity profiles at any given optical frequency. In Fig. 6.6 we show the simulation results

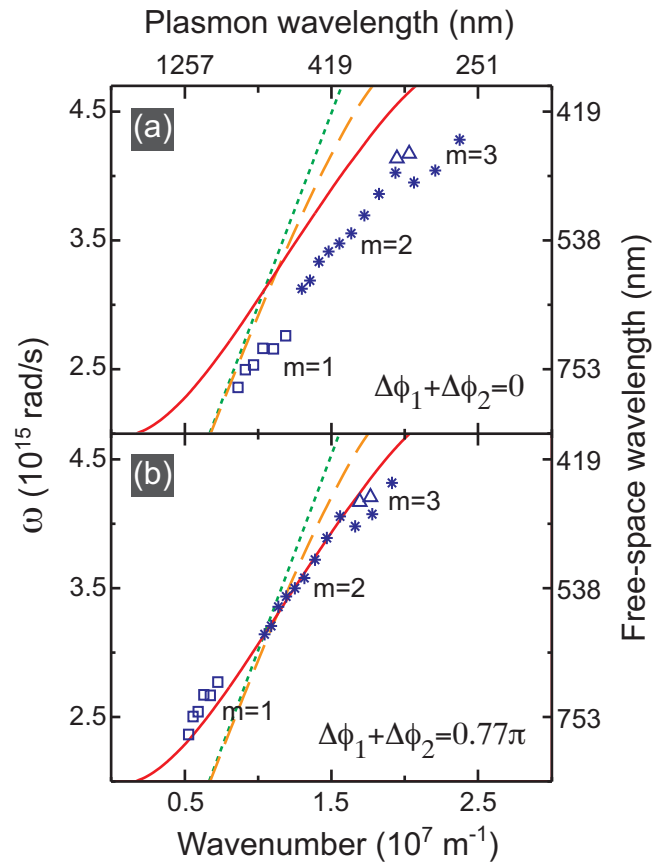


Figure 6.5: Measured dispersion data and calculated index-averaged dispersion relations (red drawn lines) for coaxial plasmon waveguides with a 100-nm-wide air channel. In (a) the dispersion data is plotted, assuming a zero net phase shift as result of reflections at the end facets of the cavity. In (b) the data is plotted for an overall reflection phase shift of 0.77π which was determined using simulations. Light lines for air are also shown (dotted green lines), along with the plasmon dispersion (dashed orange curves) at a flat Ag/air interface. Symbols in the figure correspond to different Fabry-Pérot mode numbers, m , where $\square = 1$, $*$ = 2, $\triangle = 3$.

for an air-filled coaxial waveguide of the same dimensions as the structure shown in Fig. 6.1(a) excited at an angular frequency of 4.2×10^{15} rad/s (free-space wavelength of 450 nm). Figure 6.6(a) shows the steady-state intensity distribution in the plane of polarization for the electric field component that is parallel to the polarization direction of the incident light. As in the experiment the waveguide is excited at the air-side (left-side in the figure).

In the steady state, the field profile in the cavity is a superposition of plasmon waves propagating in forward and backward direction after any number of reflections at the input or distal end of the cavity. The analytical expression of the resulting electric field in the cavity as a function of position in the direction parallel to the waveguide axis, is given by

$$E(z) \propto e^{ikz} + |r_1| e^{i(k(L-z) + \langle k \rangle L + \Delta\phi_1)} \quad (6.2)$$

where k is the plasmon wave vector (which depends on z as a result of waveguide tapering), $\langle k \rangle$ is the index-averaged wave vector, and $|r_1|$ and $\Delta\phi_1$ are the reflectance and reflection phase shift at the distal end of the cavity, respectively. Note, that the field profile inside the cavity is not affected by the reflectivity of the input end of the waveguide. In fact, the field profile is simply proportional to the original plasmon wave and the plasmon wave after one reflection, added together.

Figure 6.6(b) plots the intensity distribution in the cavity as a function of position along the waveguide axis (blue dotted curve), obtained by laterally summing the intensity values in Fig. 6.6(a). To obtain the phase shift at the distal end of the waveguide (right end in Fig. 6.6(a)) we fit the intensity distribution with $|E(z)|^2$ (see equation (6.2)). As the plasmon wave vector is calculated analytically, the only fit parameters, besides an amplitude constant, are $\Delta\phi_1$ and $|r_1|$. The result of the fit is plotted in Fig. 6.6(b) (red drawn curve). From the fit it follows that the phase shift as result of the reflection at the substrate-end of the waveguide is close to π . The visibility of the oscillation depends on the reflectance $|r_1|$ at the distal cavity end. Based on the fit we find that the reflectance of the substrate-side end facet is equal to 75%.

To obtain the reflection phase shift at the input end facet, $\Delta\phi_2$, the intensity distribution in the waveguide was simulated for light impinging on the nanostructure from the substrate-side of the cavity. We show the result of this simulation in Fig. 6.6(c). Owing to a lower reflectance of the air-side end facet of 20% the visibility of the intensity distribution is smaller. Furthermore we find that the phase shift upon reflection at the air-side cavity end is close to zero. Using the reflectance values as determined from the fits and the calculated waveguide losses we obtain a cavity quality factor of only ~ 4 , which explains the broad spectral width of resonances in measured spectra. We note however, that the cavity losses

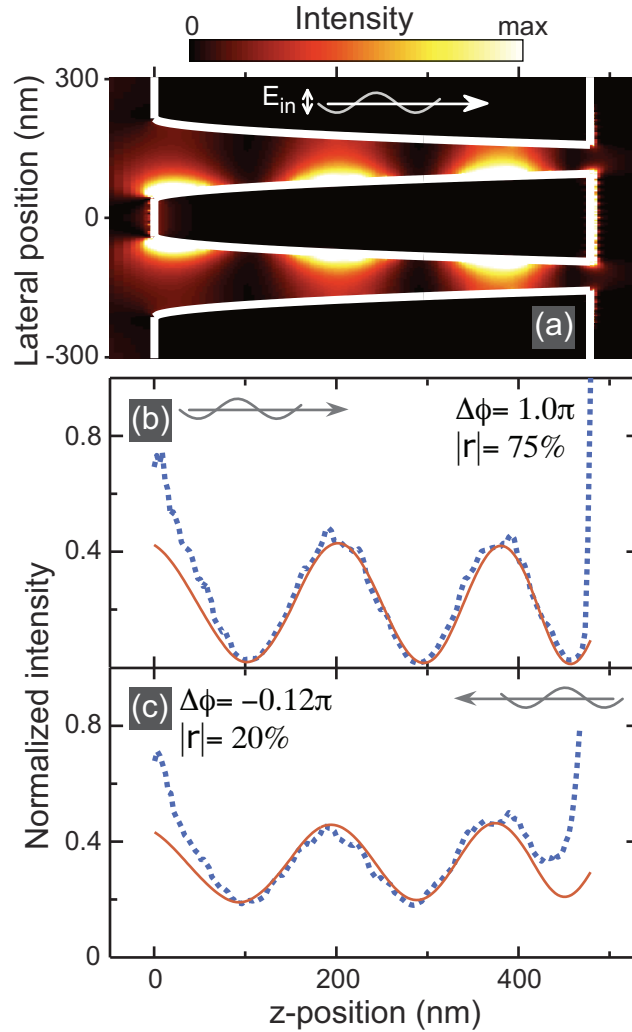


Figure 6.6: Steady-state simulation results of the electric field intensity profile inside a 485-nm long coaxial cavity with an air-filled ~ 100 -nm wide dielectric channel excited at an angular frequency of 4.2×10^{15} rad/s (free-space wavelength of 450 nm). (a) Electric field intensity distribution inside the coaxial cavity for light incident from the left. (b,c) Intensity as a function of position integrated along the lateral direction (dotted lines) for light incident from the left (b) and right (c). The red drawn curves are fits of the intensity profile, that were used to find the reflectance and reflection phase shifts at the distal end facets. The reflection phase shift is 1.0π at the substrate-side and -0.12π at the air-side of the cavity, while the values for the reflectance are 75% and 20% respectively.

are almost entirely due to the rather poorly reflecting end facets of the cavity. By improving the end face reflectivity it should be possible to attain quality factors of more than 80.

The analysis in Fig. 6.6 was done at a frequency of 4.2×10^{15} rad/s (free-space wavelength of 450 nm). At lower frequencies, we find that the overall phase shift tends to decrease (data not shown). The average net phase shift we find for frequencies within the experimental bandwidth equals $\sim 0.77\pi$. In Fig. 6.5(b) we plot the dispersion relation taking into account this average phase shift, and observe a close agreement between theory and experiment. Note, that in our analysis of waveguides with a ~ 50 -nm wide dielectric channel (Fig. 6.4) or waveguides filled with SOG, best agreement between experiment and theory was found for phase shifts close to zero, demonstrating that the phase shifts on reflection can be tuned by changing the geometry.

6.4 Conclusion

We have shown that the plasmon dispersion in coaxial waveguides with sub-wavelength dimensions can be determined from single-cavity transmission measurements. Our dispersion data agrees well with an analytical model for dispersion in coaxial waveguides of infinite length and demonstrates the large degree of tunability by varying the coaxial cavity dimensions and dielectric medium. A plasmon phase shift up to π occurs upon reflection off the cavity ends and strongly affects the cavity resonance. The phase shift depends greatly on the waveguide geometry, providing further tunability of the coaxial cavity resonances. The fundamental insights obtained in this paper are important in further studies of nanoscale waveguiding and imaging with coaxial cavities, as well as their use in negative-index metamaterials.

Negative refractive index in coaxial plasmon waveguides

We theoretically show that coaxial waveguides composed of a metallic core, surrounded by a dielectric cylinder and clad by a metal outer layer exhibit negative refractive index modes over a broad spectral range in the visible. For narrow dielectric gaps (10 nm GaP embedded in Ag) a figure-of-merit of 18 can be achieved at $\lambda_0 = 460$ nm. For larger dielectric gaps the negative index spectral range extends well below the surface plasmon resonance frequency. By fine-tuning the coaxial geometry the special case of $n = -1$ at a figure-of-merit of 5, or $n = 0$ for a decay length of 500 nm can be achieved.

7.1 Introduction

Controlling the propagation of light at the nanoscale is one of the challenges in photonics. Surface plasmons, electromagnetic modes that propagate at a metal/dielectric interface provide a key opportunity to achieve this goal, due to their relatively small evanescent fields [1, 2]. Moreover, as their dispersion can be strongly controlled by geometry, their effective wavelength can be shrunk well below the free-space wavelength, enabling further miniaturization of optical components. Initial experiments on plasmon optics were carried out at planar metal/dielectric interfaces, demonstrating basic control of plasmons. Plasmonic components such as mirrors [89, 90] and waveguides [91, 92] were realized, however still of relatively large size due to the >100 nm evanescent tails, and with limited control over dispersion. Subsequently, insulator-metal-insulator structures were investigated, and have demonstrated confinement of light to <100 nm length scales in taper geometries [75, 93], though at high loss. The reverse, metal-insulator-metal (MIM) geometries, have demonstrated lower loss, higher dispersion [77, 94], and recently the attainment of a negative index of refraction [25, 26, 95].

A disadvantage of planar MIM structures is that they only confine light in one transverse direction. Recently, coaxial MIM waveguides, composed of a metal core surrounded by a dielectric cylinder clad by a metal outer layer have been introduced, that confine light in all transverse directions [24, 80]. We have recently reported optical transmission measurements through single coaxial waveguides, from which the dispersion diagram for these nanoscale waveguides was determined [96].

Inspired by the earlier work on MIM waveguides, a natural question arises whether coaxial waveguides would possess a negative refractive index, and if so, for what geometry and over what spectral range. Since the coaxial waveguides are essentially 3-dimensional objects, the observation of negative index in individual coaxes, would also inspire the design of 3-dimensional negative-index metamaterials [30, 32, 33, 58, 97] composed of arrays of coaxial waveguides.

In this chapter we theoretically study the dispersion of coaxial Ag/Si/Ag plasmon waveguides and demonstrate that for well-chosen geometries modes with a negative refractive index are observed. These modes are dominant over other waveguide modes for a wide range of frequencies above the surface plasmon resonance frequency. We discuss the influence of waveguide geometry and material on the mode index and demonstrate that the figure-of-merit (FOM), defined as the magnitude of the real part of the propagation constant in the waveguide divided by the imaginary part [26, 98], can be as high as 18.

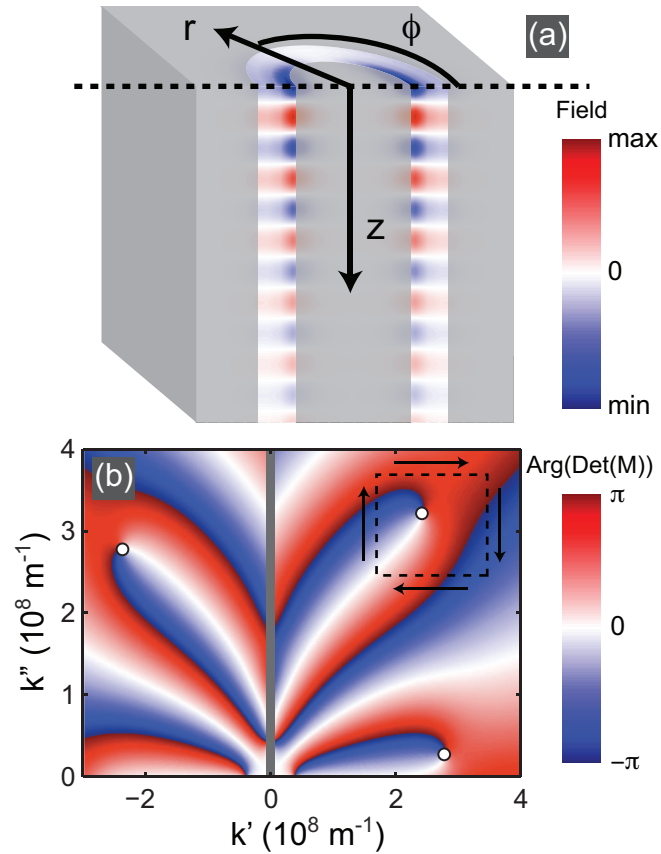


Figure 7.1: Coaxial plasmon waveguide geometry and numerical mode solving method. (a) Schematic cross-section of a coaxial waveguide with the definition of the cylindrical polar coordinates, r , ϕ and z . The metallic inner core and outer cladding separate a dielectric channel. A schematic wave propagating in the waveguide in the direction of positive z is also indicated. (b) Argument θ of the determinant, $\det[M(k)]$, plotted in the complex k -plane for a Ag/Si/Ag waveguide with 75 nm inner core diameter and 10-nm-wide dielectric channel at $\omega = 3 \times 10^{15}$ rad/s. By cycling around the closed loop indicated by the dashed square the net number of discontinuities in θ is determined. Zero positions are indicated by the white circles.

7.2 Method

Optical modes of coaxial waveguides are calculated by solving Maxwell's equations analytically [86–88]. The electric and magnetic fields in the waveguide take the form

$$\mathbf{F}(r, \phi, z, t) = \mathbf{F}(r, \phi) e^{i(kz - \omega t)} \quad (7.1)$$

where r and ϕ are the polar coordinates in the transverse plane and z is the direction of propagation (see Fig. 7.1(a)); $k = k' + ik''$ is the complex propagation constant.

The azimuthal dependence of the fields is described by the harmonic function $e^{in\phi}$ of order n . In the remainder we only consider modes with $n = 1$, since these are the lowest order modes that couple to free-space radiation. The radial dependence of the fields in all three domains (metal-dielectric-metal) is described by solutions to the 2^{nd} order Bessel differential equation. We apply a Bessel function of the first kind, J_n , to the metal core, as that function remains finite at the waveguide axis. A Hankel function of the first kind, $H_n^{(1)}$, is applied to the metal cladding. Inside the dielectric channel the radial field is described by two linearly independent cylinder functions. The arguments of the cylinder functions in each of the three domains is $\kappa_i r$, where κ_i is the radial wave number in medium i , defined via

$$\kappa_i^2 \equiv \epsilon_i \frac{\omega^2}{c^2} - k^2 \quad (7.2)$$

where ϵ_i is the complex dielectric constant in domain i . To satisfy the condition that fields decay to zero at radial infinity we take the square root of equation (7.2) such that the radial wave number has a positive imaginary part.

On each domain boundary we formulate four continuity conditions for the tangential components of the electric and magnetic fields. The optical eigenmodes of the coaxial waveguide are found when the determinant of the resulting homogeneous system of eight equations with eight unknown coefficients vanishes,

$$\det[M(k)] = 0 \quad (7.3)$$

where M is the matrix of the system of equations. We have used two independent methods for determining the optical modes, $k(\omega)$, of the structure. One involved a numerical procedure developed to detect local minima of the determinant of the system in the complex k -plane. The other method relies on the fact that the argument, θ , given by

$$\det[M(k)] = |\det[M(k)]| e^{i\theta} \quad (7.4)$$

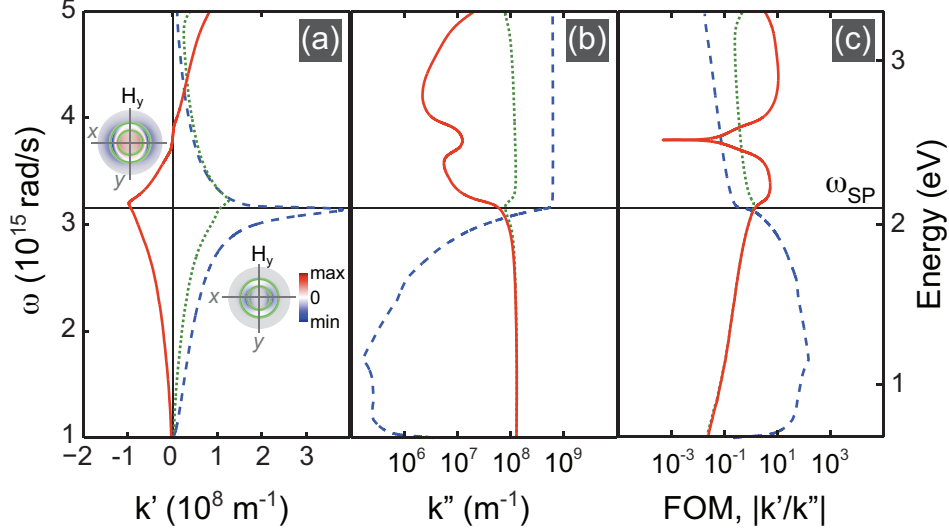


Figure 7.2: Dispersion relations of the three lowest-order modes of a coaxial waveguide with 75-nm-diameter Ag core, 25-nm wide Si channel, and infinite outer Ag cladding. Radial frequency is plotted versus propagation constant k' (a), attenuation constant k'' (b), and figure-of-merit k'/k'' (c). The Ag/Si surface plasmon resonance frequency $\omega_{SP} = 3.15 \times 10^{15}$ rad/s ($\lambda_0 = 598$ nm) is indicated by the horizontal line. Panel (a) shows two modes with positive index (blue dashed curve and green dotted curve) and one mode with a negative index below a frequency of $\sim 3.8 \times 10^{15}$ rad/s (red drawn curve). The insets in (a) show the H_y field distribution in the transverse plane of the waveguide at 2.8×10^{15} rad/s for the positive-index mode (blue dashed dispersion curve) and at 3.6×10^{15} rad/s for the negative-index mode.

is undefined when $\det[M(k)] = 0$. This can be visualized in a plot of θ in the complex k -plane. An example is shown in Fig. 7.1(b) where θ is plotted for a coaxial waveguide with a Ag core and cladding and a 10 nm silicon spacer layer. We used empirically determined optical constants for the metal [99] and dielectric [49]. Contour lines in the figure appear to close in on each other at each of the zeros, which are indicated by the white dots in the figure. By counting each discontinuity $-\pi \rightarrow \pi$ and $\pi \rightarrow -\pi$ about a closed loop in the figure (for an example, see the dashed square loop in Fig. 7.1(b)) we are able to determine the number of zeros in the enclosed area. In case we find that one or more zeros reside in the area, we split the area up in smaller pieces and repeat the procedure until the location of the zero(s) is determined with double computer precision.

Using this method, solutions for k were found for real frequency, so that dis-

persion relations, $\omega(k)$, could be constructed. Calculations were performed in the optical angular frequency regime $1 \times 10^{15} \text{ rad/s} < \omega < 5 \times 10^{15} \text{ rad/s}$ (free-space wavelength, $\lambda_0 = 377\text{--}1884 \text{ nm}$). We only consider modes with positive energy velocity, v_e , or equivalently, positive attenuation constant k'' [26]. Therefore, to achieve antiparallel energy and phase velocity, which is the unique requirement for a negative mode index, the propagation constant k' needs to be negative.

7.3 Results

Figure 7.2 shows the dispersion relation, $\omega(k)$, for the three lowest-order modes in a coaxial waveguide consisting of a 75-nm-diameter Ag core surrounded by a 25-nm-thick Si layer and infinite Ag cladding. In (a) the angular frequency is plotted against k' , while (b) shows the frequency as function of k'' , which determines the propagation length of light in the waveguide via

$$L = \frac{1}{2k''}. \quad (7.5)$$

The surface plasmon resonance frequency $\omega_{SP} = 3.15 \times 10^{15} \text{ rad/s}$ ($\lambda_0 = 598 \text{ nm}$) is indicated by the horizontal line.

Figure 7.2(a) shows two coaxial modes (blue dashed line and green dotted line) with positive propagation constants over the entire spectral range. Both dispersion curves closely resemble the dispersion of a surface plasmon polariton propagating along a planar Si/Ag interface. However, the corresponding propagation constants (Fig. 7.2(a)), are nearly three times as large as for the planar single interface plasmon. This is due to the fact that confinement of the plasmon in the coaxial waveguide geometry leads to larger mode overlap with the metal. Figure 7.2(a) also shows the existence of a third mode (red drawn curve) that has a negative propagation constant k' for frequencies below $3.8 \times 10^{15} \text{ rad/s}$ ($\lambda_0 = 496 \text{ nm}$). The effective index $n = ck'/\omega$ ranges from $-9 < n < 5$ in the frequency range of Fig. 7.2. The insets in (a) show the H_y field in the transverse plane for the negative-index mode (calculated at $\omega = 3.6 \times 10^{15} \text{ rad/s}$) as well as for the most dispersive positive mode (blue dashed curve in Fig. 7.2(a), $\omega = 2.8 \times 10^{15} \text{ rad/s}$). From the images it is clear that the mode with positive effective index has a symmetric field distribution with respect to the two centers of the dielectric channel on the x-axis. The H_y field is primarily concentrated at the boundary between the metal core and dielectric channel. The negative-index mode in contrast, has its field primarily concentrated at the outermost channel boundary and has an H_y -field distribution that is anti-symmetric about the center of the dielectric channel, similar to modes with negative index in planar metal-insulator-metal waveguides [26].

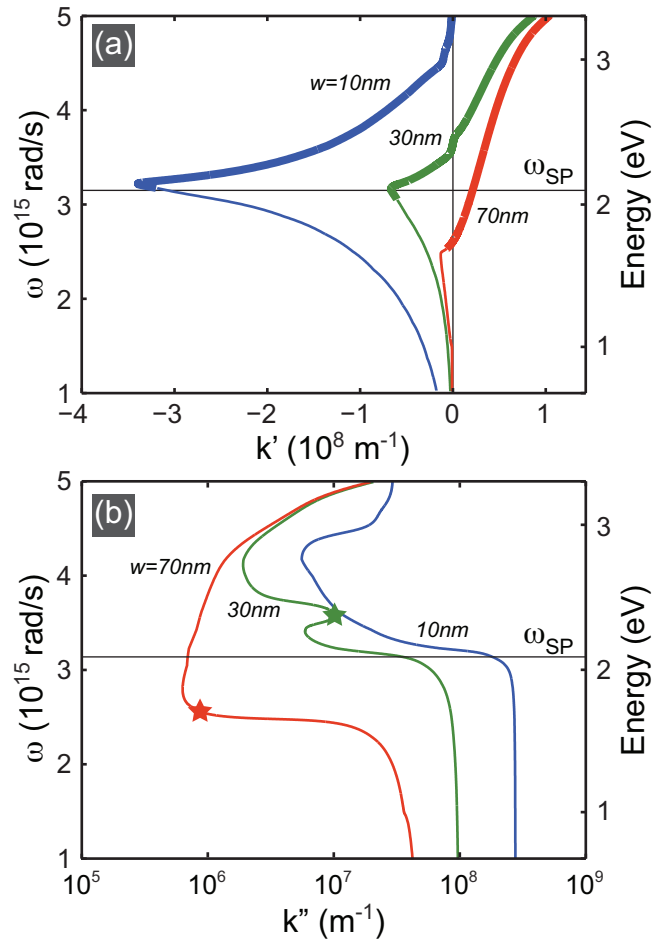


Figure 7.3: Dispersion relations for negative-index coaxial waveguides with Ag core and cladding and Si dielectric channel, (a): $\omega(k')$; (b): $\omega(k'')$. The inner core diameter is fixed at 75 nm and the Si-channel thickness w is 10 nm, 30 nm, and 70 nm. Positive-index modes (as shown in Fig. 7.2(a)) are not shown in the figure. The bold sections of the dispersion curves indicate the spectral range over which the negative-index mode is dominant, i.e. has lower loss than the positive index modes. The frequency where the red and green dispersion curves cross $k' = 0$ is indicated by the star-symbols.

Figure 7.2(b) shows that for frequencies below the surface plasmon resonance frequency ω_{SP} the lowest-order positive-index mode (blue dashed line) has lowest loss and will therefore be dominant over other modes. Interestingly, above ω_{SP} the negative-index mode (red curve) becomes the dominant mode, as its losses are significantly lower than those for the positive-index modes. Figure 7.2(c) shows the figure-of-merit (FOM), k'/k'' , of the modes. As can be seen, the negative-index mode has a FOM that approaches 10 for a narrow frequency interval around 3.4×10^{15} rad/s ($\lambda_0 = 554$ nm). The data in Fig. 7.2 clearly demonstrate that dominant modes of negative index indeed exist in coaxial plasmon waveguides.

Next, we investigate the conditions that are required to achieve a negative index by varying the geometry and materials of the waveguide. Figure 7.3 shows the effect of changing the dielectric layer thickness on the dispersion of the negative index mode. Calculations were performed for a Ag/Si/Ag coaxial waveguide with a core diameter of 75 nm for a dielectric layer thickness of 10 nm, 30 nm, and 70 nm. Figure 7.3(a) shows that the variation in dielectric layer thickness has a very dramatic effect on the dispersion of the negative-index mode. First of all, the largest negative index is observed for the thinnest dielectric. Second, while for the 10-nm and 30-nm dielectric gaps the frequency of the resonance associated with the negative index mode appears close to the surface plasmon resonance at 3.2×10^{15} rad/s, for the 70-nm gap this resonance is significantly red-shifted to 2.5×10^{15} rad/s. The spectral range over which the mode is dominant, indicated by the bold curves in Fig. 7.3(a), also extends to lower frequencies when increasing the channel width. For the 70-nm gaps a narrow frequency range is found near 2.4×10^{15} rad/s ($\lambda_0 = 785$ nm) where the index is negative and the figure-of-merit is 5.

As the dispersion branches cross the $k' = 0$ line the effective refractive index of the mode vanishes [100]. Coaxial waveguides with a narrow dielectric gap suffer high loss at this frequency. The green star in Fig. 7.3(b) indicates the frequency at which the dispersion curve crosses the $k' = 0$ line for the 30-nm gap; a high value of $k'' = 10^7$ m⁻¹ is found. In contrast, for the 70-nm-wide dielectric channel waveguides the losses at the $k' = 0$ crossing (red star in Fig. 7.3(b)) are much lower ($k'' < 10^6$ m⁻¹), corresponding to a decay length of 500 nm. Note that in the spectral range where the phase velocity ω/k' goes to zero, the group velocity, $v_g = d\omega/dk'$, is much larger than zero.

The two striking effects observed here: a) waveguide resonances that shift with geometry, and b) increased propagation length for $k' = 0$ modes for increasing dielectric thickness are in strong contrast to what is observed in planar metal-insulator-metal waveguides [26]. This suggests that coupling of plasmon fields across the nanoscale diameter of the metal core strongly influences the dispersion

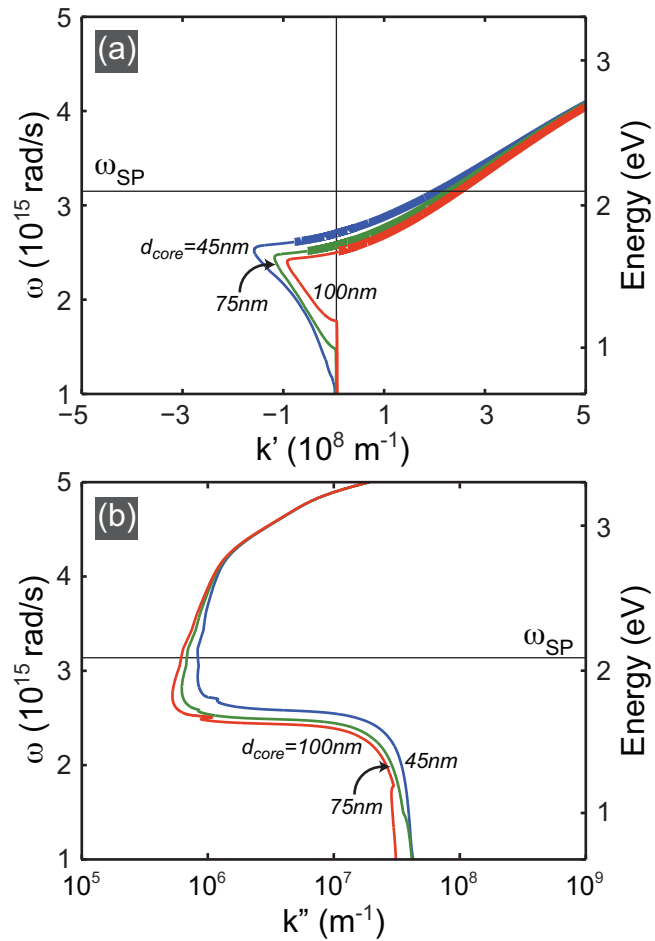


Figure 7.4: Dispersion relations for coaxial waveguides with Ag core and cladding and 70-nm-wide Si dielectric channel, (a): $\omega(k')$; (b): $\omega(k'')$. The inner core diameter, d_{core} , is 45 nm (blue curves), 75 nm (green curves) and 100 nm (red curves). Only modes with negative index are plotted. Bold lines indicate the spectral range where the mode is dominant over the positive-index mode.

of the negative index modes. To investigate this, we studied the influence of the metal core diameter on the dispersion of the mode, while keeping the channel width fixed to 70 nm. Figure 7.4 shows the results for waveguides with inner core diameters of 45, 75 and 100 nm. The figure shows that the spectral range where the mode is both dominant and characterized by a negative index becomes smaller going from a 45-nm-diameter core to a 75 nm core, and vanishes when the core size is increased to 100 nm. This behavior coincides with a red-shift of the resonance in k'' when the core diameter is increased (Fig. 7.4(b)). We attribute the resonance red-shift for increasing core diameter to a depolarization effect similar to what is known for bulk metallic particles, which show a plasmon resonance red-shift for increasing diameter [65]. Based on this insight, we predict that a large degree of control over dispersion and resonance red-shift may also be attained in planar structures composed of a multi-layered stack of metal and dielectric. In fact, negative index materials based on metal-dielectric multi-layers have been reported in literature [101]. A final observation that can be made in Fig. 7.4 regards the special case of $n = -1$; for a coaxial waveguide with a core diameter of 50 nm and a 70-nm wide Si channel a mode with $n = -1$ is observed with a FOM = 5 at $\omega = 2.61 \times 10^{15}$ rad/s (free-space wavelength of 720 nm).

Thus far we have studied the influence of the coax geometry on the frequency dispersion of k . Next, we will investigate the effect of changing the type of metal in core and cladding, as well as the dielectric in the cylindrical channel. Figure 7.5 shows the frequency dispersion for a coaxial waveguide with inner metal core diameter of 75 nm and dielectric channel width of 25 nm surrounded by an infinite metal cladding. We compare the results for Si (blue curves), GaP (green curves), and silica (red curves) channels in Ag, and for a Si channel in Au (purple curves). The curves are normalized to the surface plasmon resonance frequency for the corresponding planar metal/dielectric geometry. Interestingly, coaxial plasmon waveguides support dominant negative index modes regardless of the investigated choice of materials. The propagation vector k' is most strongly negative for waveguides filled with GaP and least negative for silica, which indicates that, to obtain a strong effect, the dielectric constant needs to be high ($n_{GaP} = 3.5$ at the GaP/Ag surface plasmon resonance). The figure-of-merit for the modes in Fig. 7.5(a) is plotted in Fig. 7.5(b). Due to the low loss and high index of GaP, the highest figure-of-merit is found in these waveguides. The highest number we found (FOM = 18) was for a 10-nm-wide GaP channel in Ag at $\omega = 4.1 \times 10^{15}$ rad/s ($\lambda_0 = 460$ nm, data not shown). Waveguides composed of Au show a lower FOM than those with Ag, which is attributed to the higher losses in Au.

Finally, in Fig. 7.6 we present the field distribution in a coaxial waveguide with negative index. Figure 7.6(a) shows the H_y -field on the outer metal-dielectric in-

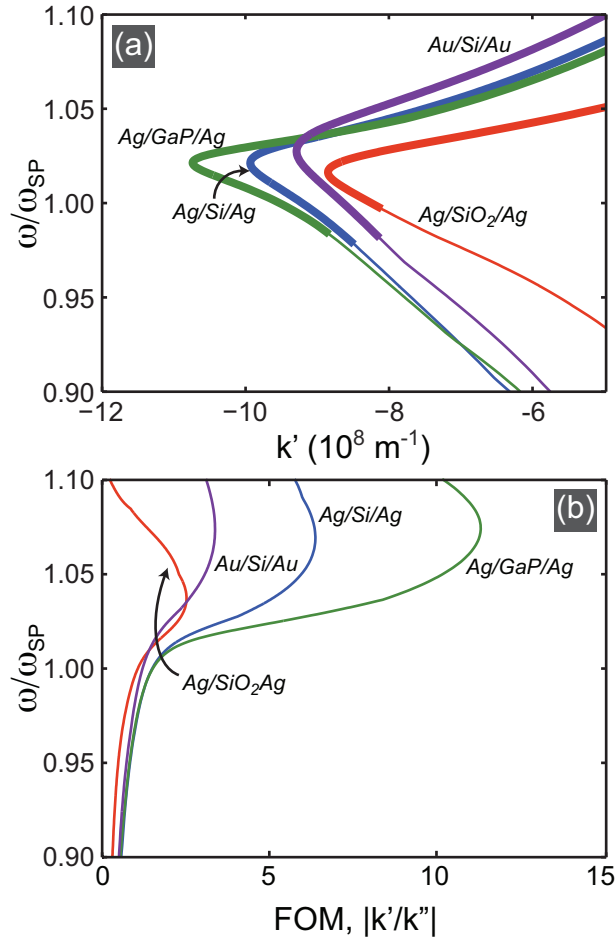


Figure 7.5: Dispersion relations for coaxial waveguides with 75-nm-diameter metal core, 25-nm-wide dielectric channel and infinite metal cladding, (a): $\omega(k')$; (b): FOM k'/k'' . The type of metal in the core and cladding, as well as the dielectric material was varied. The frequency axes are normalized to the corresponding surface plasmon resonance frequency ω_{SP} . Blue curves are for a Si channel surrounded by Ag ($\omega_{SP} = 3.15 \times 10^{15}$ rad/s), green curves for GaP in Ag ($\omega_{SP} = 3.49 \times 10^{15}$ rad/s), red curves for SiO₂ in Ag ($\omega_{SP} = 5.24 \times 10^{15}$ rad/s) and purple curves for Si in Au ($\omega_{SP} = 2.77 \times 10^{15}$ rad/s). Bold curves indicate the spectral range where the negative-index mode is dominant.

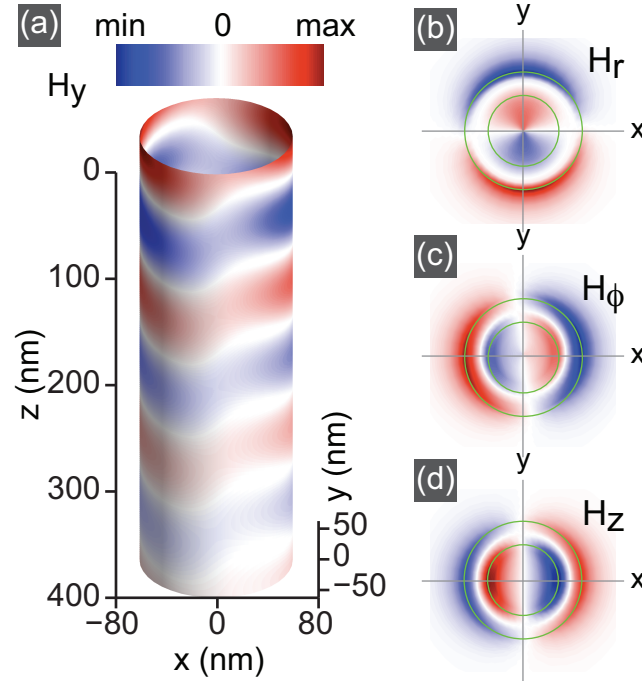


Figure 7.6: Magnetic field images of a coaxial waveguide with 75 nm Ag core diameter, 25-nm-wide GaP-filled ring and infinite Ag cladding at a frequency of 3.75×10^{15} rad/s. In (a) we plot the H_y field distribution on the boundary of the Ag cladding with the dielectric channel. Note that the phase-fronts in the waveguide are in general not perpendicular to the optical axis (z -axis). In (b-d) we plot the polar magnetic field components in the transverse plane. The amplitude of the fields plotted in the figure has the same order of magnitude in all of the four panels.

terface of a coaxial waveguide with 75-nm-diameter Ag core and 25-nm-wide GaP channel for a frequency $\omega = 3.75 \times 10^{15}$ rad/s (free-space wavelength of 500 nm, $\omega/\omega_{SP} = 1.08$ in Fig. 7.5). Clearly, the phase fronts in the waveguide are not planar. As a result, a non-zero z -component of the electromagnetic field is observed. Figure 7.6(b) shows the distribution of H_r in the transverse plane. Its magnitude is similar to that of the H_y -field. For completeness, Figures 6 (c) and (d) show the H_ϕ and H_z components of the field. Note that these fields are antisymmetric with respect to the center of the dielectric channel and are located mostly inside the metal.

7.4 Conclusion

We have theoretically demonstrated that coaxial plasmon waveguides sustain modes with negative refractive index at optical frequencies. The negative-index modes have a larger propagation length than the positive-index modes over a large spectral range, depending on the dielectric thickness. For a 10-nm-wide GaP dielectric and a 75-nm-wide Ag core a figure-of-merit $k'/k'' = 18$ is found at $\lambda_0 = 460$ nm. For Ag/Si/Ag coaxial waveguides with increasing Si-channel thickness the dominant negative-index mode shifts well below the surface plasmon resonance frequency: for a 70 nm Si-channel it is found at $\lambda_0 = 750$ nm. The mode index can be fine-tuned to a value of -1 with a figure-of-merit as high as 5 at 720 nm. At slightly higher frequencies, the same mode has an effective index $n=0$ with positive group velocity, and a decay length of 500 nm. Overall higher tunability and figure-of-merit are found for coaxial waveguides of Ag rather than Au, and filled with a dielectric of highest optical constant. Based on the large degree of dispersion control that can be achieved with coaxial plasmon waveguides we anticipate that these structures will find use in new designs for nanoscale photonic integrated circuits (waveguides, splitters, multiplexers), in three-dimensional negative-index metamaterials, and invisibility cloaks.

A single-layer negative-index metamaterial at visible frequencies

Metamaterials are artificial electromagnetic materials built-up by sub-wavelength structuring rather than chemical composition. Negative-index metamaterials (NIMs) are a special class, with both negative permittivity and permeability. To date, three-dimensional NIMs have been realized through layering of resonant periodic structures, such as split-ring resonators, and have been demonstrated at microwave to infrared frequencies in a narrow range of angles-of-incidence and polarization. We report simulations of a metamaterial composed of a single functional layer of coupled coaxial plasmon waveguides, that exhibits an index of refraction of $n \sim -2$ in the blue spectral region with a figure-of-merit > 8 . The resulting NIM refractive index is independent of the angle-of-incidence over an angular range of $\pm 50^\circ$ and independent of the polarization direction, yielding a functionally three-dimensional NIM at visible frequencies.

8.1 Introduction

Metamaterials are artificial materials that exhibit extraordinary electromagnetic properties not observed in their constituent materials. In resonant-element based negative-index materials (NIMs), the unusual “left-handed” behavior of light originates from sub-wavelength resonant elements that behave like “artificial-atoms” with engineered magnetic and electric resonance giving rise to a negative permeability and permittivity and thus to an effective negative index. NIMs offer many appealing functionalities, including imaging below the diffraction limit [33, 78], and invisibility cloaking [28, 79, 102–104]. Negative refraction was first demonstrated experimentally in arrays of mm-size copper strips and split-ring resonators operating at microwave frequencies [105]. This discovery sparked a great effort to scale down the size of constituent resonant components to enable operation at higher frequencies. For example, micrometer-sized structures were successfully fabricated giving rise to a negative refractive index at THz frequencies [106]. For operation at optical frequencies the typical size of the sub-wavelength scatterers is in the 10–100 nm range, very close to practical fabrication limits. So far, the highest reported operational frequency of NIMs was demonstrated at the deep-red side of the visible spectrum ($\lambda_0 = 780$ nm) using structures with features as small as 8 nm [107]. Moreover, to achieve significant scattering from the constituent elements in the visible, metamaterial need to be built up from a stack of multiple functional layers [32, 107]. This further limits the feasibility of fabricating an NIM based on scattering elements in the visible regime.

Recently, a conceptually different approach was taken to achieve a negative refractive index in the visible. Investigation of the mode structure of two-dimensional metal/insulator/metal (MIM) plasmonic waveguides [25, 26] revealed that certain MIM waveguide geometries exhibit a negative index of refraction at visible frequencies. Arrays of negative-index MIM waveguides can serve as a quasi three-dimensional metamaterial [95]. However, such geometries only exhibit a negative index for specific polarization and angle-of-incidence. This is due to the fact that plasmonic MIM modes, which are transverse-magnetically (TM) polarized, can only be excited with electric fields perpendicular to the MIM interface, and the negative index mode, which has an antisymmetric field profile, can only be excited at off-normal incidence [26].

These practical limitations of planar MIM geometries can be circumvented in a coaxial MIM geometry in which the planar MIM waveguide is wrapped onto itself to create a structure with a metal core, surrounded by a dielectric cylinder and a metal cladding (see Fig. 8.1). Calculations on individual coaxial plasmonic MIM waveguides show a negative refractive index, which is relatively insensitive to

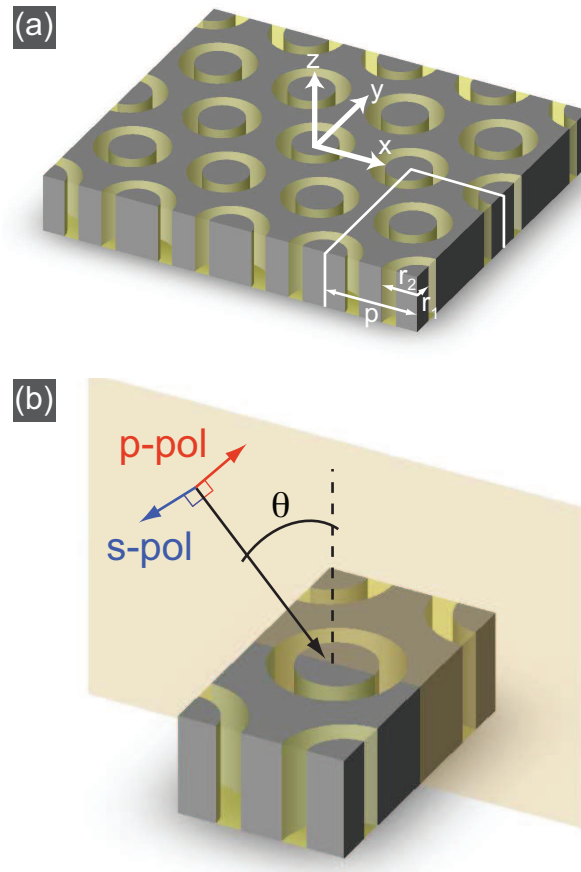


Figure 8.1: Schematics of the NIM layer geometry. (a) Slab of single-layer NIM consisting of sub-wavelength coaxial structures in hexagonal configuration. Inner radius r_1 , as well as the outer radius r_2 , and the array pitch p are defined in the image. (b) Image of a unit cell of the periodic structure. The angle-of-incidence θ as well as the in-plane (p) and out-of-plane (s) polarization directions are shown.

the angle-of-incidence and polarization due to the cylindrical symmetry. Here, we theoretically demonstrate that a two-dimensional array of vertically oriented MIM waveguides arranged in a dense hexagonal configuration functions as a three-dimensional single-layer negative-index material at visible frequencies down to the blue. We show that the refractive index of this new geometry is insensitive to the angle-of-incidence over an angular range of $\pm 50^\circ$ and independent of the polarization direction of incident light.

8.2 Methods and results

Figure 8.1 shows schematics of the NIM layer under study. We consider coaxial MIM waveguides composed of a 25-nm thick cylindrical channel of GaP, wrapped around a Ag core, and embedded in a Ag layer. The inner Ag core radius r_1 and outer radius r_2 are fixed at 37.5 nm and 62.5 nm respectively, while the array pitch p was varied in the range of 165–330 nm. Figure 8.1(b) shows the unit cell of the periodic metamaterial.

To estimate the effective refractive index of the material, we first calculate the mode index dispersion in the constituent coaxial elements by solving Maxwell's equations in cylindrical coordinates [24, 86, 88] for a coaxial MIM waveguide of infinite length (see chapter 7). The eigenmodes of the waveguide that we find are given by the complex propagation constant $k(\omega) = k'(\omega) + ik''(\omega)$, where k' is the propagation constant and k'' is the attenuation constant, which both strongly depend on the frequency ω . We define the direction of energy flow as the direction where light is attenuated, given by the sign of k'' , which is always kept positive in our calculations. In that case, the mode refractive index n is given by $n = ck'/\omega$, where c is the velocity of light. Optical constants for the calculations are taken from tabulated literature data¹.

In Fig. 8.2(a) we show calculated index dispersion relations for a single coaxial Ag/GaP/Ag waveguide with $r_1 = 37.5$ nm and $r_2 = 62.5$ nm. The Ag/GaP surface plasmon energy $\hbar\omega_{SP}$ is indicated for reference. In qualitative agreement with reported results on planar MIM structures [26] we find one mode with positive index over the entire spectral range (red curve), and a second mode with a negative refractive index for energies below 2.7 eV ($\lambda_0 = 460$ nm, blue curve). The effective index of the second mode ranges from $-9 < n < 1$ in the energy range of Fig. 8.2. The insets in Fig. 8.2(a) show the H_y field profiles corresponding to the positive

¹For the metal we used optical data taken from [99]; for GaP we used optical constants from [49].

²We only show dispersion for the two lowest order modes with the right symmetry to couple to free-space radiation.

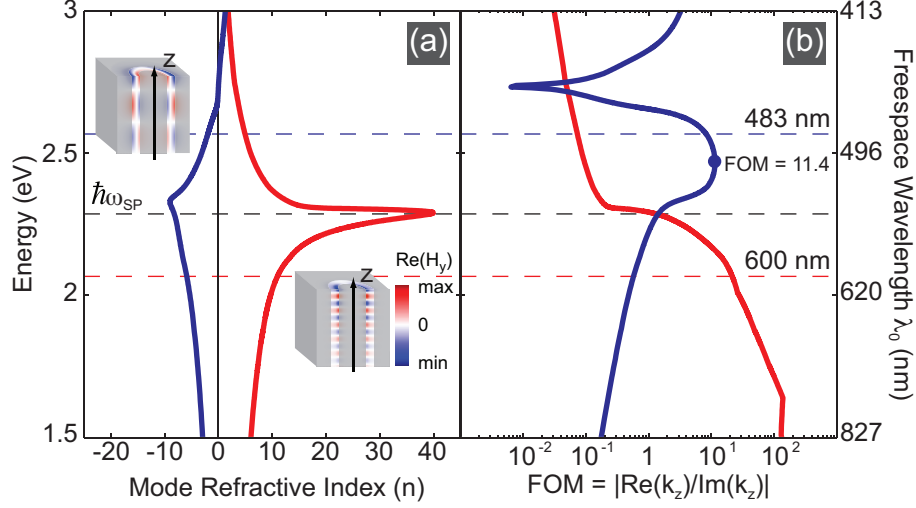


Figure 8.2: Dispersion relations of the two lowest-order modes in a coaxial waveguide consisting of an inner Ag core with radius, $r_1 = 37.5$ nm, 25 nm thickness GaP channel, and infinite Ag cladding. Energy is plotted versus the mode index n (a) and figure-of-merit (FOM) $|k'/k''|$ (b). The Ag/GaP surface plasmon energy $\hbar\omega_{SP}$ at 2.3 eV ($\lambda_0 = 540$ nm) is indicated by the black dashed horizontal line. Panel (a) shows one mode with positive index (red curve) and one mode (blue curve) with a negative index below an energy of 2.7 eV ($\lambda_0 = 460$ nm). The insets in (a) show the H_y field distribution in the waveguide at a wavelength of 600 nm for the positive-index mode and at 483 nm for the negative index mode.

index mode at $\lambda_0 = 600$ nm ($n = 11$) and the negative index mode at $\lambda = 483$ nm ($n = -1.8$). The positive-index mode has a field profile that is radially symmetric within the GaP channel, while the negative-index mode exhibits an antisymmetric field profile in the gap between the metal core and cladding.

Figure 8.2(b) shows the figure-of-merit (FOM) defined as $\text{FOM} = k'/k''$ for the two modes. We find that the mode with positive index (red curve) is dominant for energies below $\hbar\omega_{SP} = 2.3$ eV with a FOM ranging from 1–100. However, for energies above $\hbar\omega_{SP}$, the negative-index mode (blue curve) is dominant with a maximum FOM of 11.4 at $\lambda_0 = 503$ nm. The lowest propagation loss (k'') for the negative index mode is found at $\lambda_0 = 483$ nm, with a corresponding FOM of 8.3.

Next, we discuss the collective response of coupled coaxial waveguide arrays. We first model a hexagonal array of semi-infinitely long coaxial waveguides embedded in a Ag slab. Exploiting the symmetry of the array, we define a single

metamaterial unit cell and apply Bloch boundary conditions along the in-plane directions and simulate the collective response using finite difference time domain (FDTD) calculations.

Figure 8.3(a) shows a time-snapshot of the H_y -field in an array with a pitch of 165 nm illuminated by a p-polarized plane wave of $\lambda_0 = 483$ nm at an incidence-angle of 30° . At this pitch the waveguides are separated by 40 nm, or twice the skin depth $\delta \sim 20$ nm of an isolated waveguide. Clearly, phase fronts are observed that refract in the negative direction, i.e. to the same side of the interface normal as the incident light. By following the phase fronts in time (data not shown) we observe backward phase propagation at an angle of -13° with respect to the interface normal, as indicated in the figure by the blue arrow labeled k .

To measure the direction of power flow, we calculate the Fourier transform of the fields at the excitation frequency, yielding field quantities that are proportional to the system's steady state response. Although the power flow is highly anisotropic in the layer, its average direction can be determined by spatially averaging the Poynting vector components inside the material. This procedure yields an average Poynting vector S depicted as a green arrow in Fig. 8.3(a) with antiparallel orientation to the phase velocity direction, an indication of having a true negative index of refraction in the layer. Using Snell's law of refraction and the Poynting vector angle we find that the metamaterial has an effective refractive index of -2.2 , close to the index of individual coaxes ($n = -1.8$). This value also corresponds to the increased spatial frequency in the refracted beam. From the wavelength in the metamaterial and the exponential energy decay in the waveguides we find a FOM= 8.2 in the material, nearly equal to the FOM calculated for isolated coaxial structures.

By repeating these simulations and analyses for angles ranging from normal incidence to an angle of 50° , for both s- and p-polarized light at $\lambda_0 = 483$ nm, we find very similar results for the refractive index, with n varying between -2.3 and -2.0 . Such small dependence of the index on polarization and angle-of-incidence has not been demonstrated in any other NIM so far. Valentine *et al.* for example only investigate normal incidence for a NIM in the near-infrared [32], while planar MIM structures can only be excited at a small range of angles and specific polarization [26].

To corroborate these results, we have simulated a wedge refraction experiment using a ~ 300 -nm-thick metamaterial slab, cut at a 3-degree angle. As illustrated in Fig. 8.4(a), one side of the wedge is illuminated at normal incidence with p-polarized light of $\lambda_0 = 483$ nm. To prevent undesired reflections from the surface of the simulation volume to appear in the image, light was coupled into the layer from a $1.2\ \mu\text{m}$ -wide dielectric waveguide oriented perpendicular to the metamaterial plane. Figure 8.4(a) shows that light refracts negatively at the angled side of

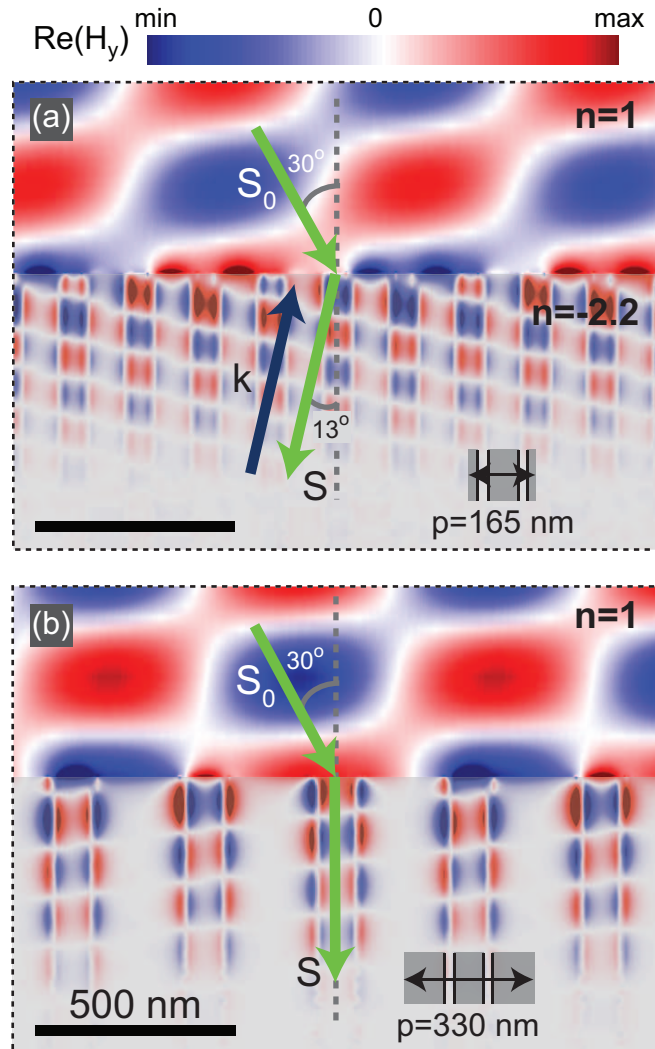


Figure 8.3: Time-snapshots of the magnetic field distribution (H_y) in the polarization plane. Light of $\lambda_0 = 483$ nm is incident on a semi-infinite slab of single-layer NIM at an angle of 30° from air. The constituent Ag/GaP/Ag coax elements in the array have an inner radius $r_1 = 37.5$ nm and outer radius $r_2 = 62.5$ nm. The array pitch p is 165 nm (a) and 330 nm (b). Arrows denote the direction of energy flow (S) and phase velocity (k). For clarity we also indicate the unit cell of the structure.

the prism, exiting the structure at an angle $\theta = -7^\circ$ with respect to the surface normal of the outgoing plane (dashed line in Fig. 8.4(a)). Figure 8.4(b) shows a polar plot of the refracted light, obtained by transformation of the near-field, monitored at the exit side of the prism, to the far-field. Using Snell's law and the negative refraction angle we derive a refractive index of the metamaterial slab of $n = -2.0$, in agreement with the index derived from Poynting vector calculations for the semi-infinite slab.

To demonstrate the metamaterial's index insensitivity to the angle-of-incidence, we also simulate the refraction of light for 30° off-normal incidence (Figs. 8.4(c,d)), again for a 3-degree wedge. The green arrows in Fig. 8.4(c) indicate the direction of the Poynting vector for the incident and refracted beams. In this case the beam is refracted at an angle $\theta = -38^\circ$ with respect to the flat interface, corresponding to an index $n = -2.0$, again equal to the index found for normal incidence.

To illustrate the metamaterial's tunability with wavelength, we study the refraction for 600 nm radiation for which the mode index dispersion for a single waveguide element (Fig. 8.2(a)) shows a positive index ($n = 11$). Indeed, as Figs. 8.4(e,f) show, the beam is now refracted to the opposite side of the interface normal, to an angle of 20° , corresponding to a positive index of $n = 6.5$. We attribute the difference in index between the metamaterial and isolated waveguides to strong in-plane coupling between the coaxial waveguides. Thus, by illuminating the structure with wavelengths either above or below the surface plasmon resonance of Ag/GaP, we can excite both positive and negative refractive indices within the same metamaterial. Furthermore, by tuning the index dispersion of individual coaxial elements (e.g. by varying the dielectric layer thickness or material), we can precisely tune the metamaterial-index at a given frequency to take very large negative or positive values.

Finally, we address the effect of in-plane coupling on the effective refractive index of the layer. The collective refraction behavior shown in Fig. 8.3(a) and Fig. 8.4 implies that strong in-plane coupling between neighboring waveguides occurs. Figure 8.3(b) shows refraction in a semi-infinite slab of material at an angle-of-incidence of 30° with respect to the interface normal ($\lambda_0 = 483$ nm). The array pitch $p = 330$ nm, corresponds to an inter-waveguide separation of 205 nm, or more than ten times the skin depth $\delta = 20$ nm. At this separation distance we do not expect to see any coupling, which should result in vertical power flow along each waveguide, as observed for isolated waveguides. Indeed, by calculation of the average Poynting flux in the layer we establish that no net horizontal power flow occurs. This illustrates the strong dependence of the layer response on the array pitch, which thus possibly serves as another way to tune the material index.

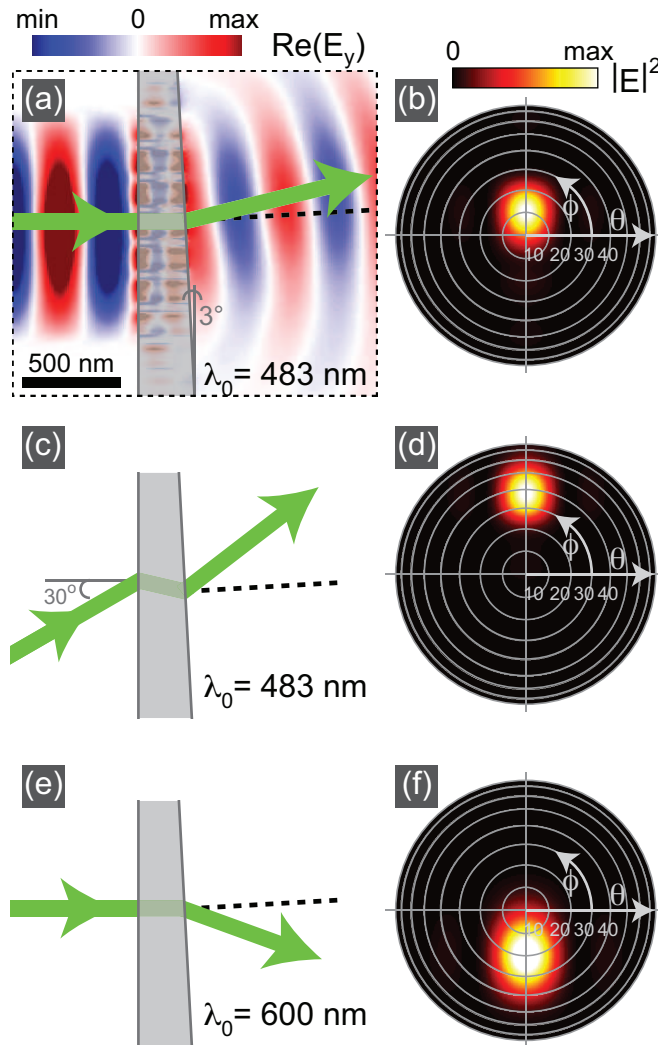


Figure 8.4: Wedge refraction simulations. A ~ 300 -nm-thick metamaterial slab is illuminated from the left at normal (a,b,e,f) and 30-degree off-normal incidence (c,d). The right side of the slab is cut at a 3-degree angle to allow refraction (black dashed line indicates the surface normal). The wavelength of incident light λ_0 is 483 nm (a-d) and 600 nm (e,f). The three panels on the left (a,c,e) depict the calculated power flow in- and outside the slab (green arrows), while the three corresponding right-side panels (b,d,f) show the electric far-field intensity in a polar plot. In panel (a) we also plot the E_y field distribution in the plane of refraction for light incident on the metamaterial from a $1.2\text{ }\mu\text{m}$ -wide waveguide.

8.3 Conclusion

We have theoretically demonstrated a novel optical metamaterial, composed of coupled coaxial Ag/GaP/Ag channels that exhibits a negative index of refraction in the blue. Unlike previous optical metamaterial designs based on resonant elements [31, 32, 98, 108], requiring multiple functional layers to achieve strong scattering, the NIM discussed here requires only a single functional layer composed of coupled coaxial waveguides. Antiparallel energy and phase velocity is observed. We show that the index of the material is independent of the angle-of-incidence over an angular range $\pm 50^\circ$ and is independent of polarization. Furthermore, with the dispersion relation of the individual constituent plasmonic coaxial waveguides largely determining the operation of the metamaterial, the structure presented here is highly tunable in index, ranging from large negative values to large positive values in the visible frequency regime. We anticipate that the single-layer geometry of this new negative-index metamaterial renders the design highly feasible for fabrication using standard nanofabrication tools. This work opens the way to nanoscale optical imaging of e.g. biological samples, and invisibility cloaking in the visible spectral range.

REFERENCES

- [1] W. L. Barnes, A. Dereux, and T. W. Ebbesen, *Surface plasmon subwavelength optics*, Nature **424**, 824 (2003).
- [2] E. Ozbay, *Plasmonics: Merging photonics and electronics at nanoscale dimensions*, Science **311**, 189 (2006).
- [3] A. Polman, *Plasmonics applied*, Science **322**, 868 (2008).
- [4] U. Kreibig and M. Vollmer, *Optical properties of metal clusters*, Springer, Berlin, 1995.
- [5] L. R. Hirsch, A. M. Gobin, A. R. Lowery, F. Tam, R. A. Drezek, N. J. Halas, and J. L. West, *Metal nanoshells*, Ann. Biomed. Eng. **34**, 15 (2006).
- [6] S. Pillai, K. R. Catchpole, T. Trupke, G. Zhang, J. Zhao, and M. A. Green, *Enhanced emission from Si-based light-emitting diodes using surface plasmons*, Appl. Phys. Lett. **88**, 161102 (2006).
- [7] K. R. Catchpole and A. Polman, *Plasmonic solar cells*, Opt. Express **16**, 21793 (2008).
- [8] J. Homola, S. S. Yee, and G. Gauglitz, *Surface plasmon resonance sensors: review*, Sensor Actuat. B-Chem. **54**, 3 (1999).
- [9] H. Mertens, J. S. Biteen, H. A. Atwater, and A. Polman, *Polarization-selective plasmon-enhanced silicon quantum-dot luminescence*, Nano Lett. **6**, 2622 (2006).
- [10] K. Kneipp, Y. Wang, H. Kneipp, L. T. Perelman, I. Itzkan, R. Dasari, and M. S. Feld, *Single molecule detection using surface-enhanced Raman scattering (SERS)*, Phys. Rev. Lett. **78**, 1667 (1997).

References

- [11] S. M. Nie and S. R. Emery, *Probing single molecules and single nanoparticles by surface-enhanced Raman scattering*, *Science* **275**, 1102 (1997).
- [12] J. R. Krenn, A. Dereux, J. C. Weeber, E. Bourillot, Y. Lacroute, J. P. Goudonnet, G. Schider, W. Gotschy, A. Leitner, F. R. Aussenegg, and C. Girard, *Squeezing the optical near-field zone by plasmon coupling of metallic nanoparticles*, *Phys. Rev. Lett.* **82**, 2590 (1999).
- [13] P. Muhlschlegel, H. J. Eisler, O. J. F. Martin, B. Hecht, and D. W. Pohl, *Resonant optical antennas*, *Science* **308**, 1607 (2005).
- [14] L. A. Sweatlock, S. A. Maier, H. A. Atwater, J. J. Penninkhof, and A. Polman, *Highly confined electromagnetic fields in arrays of strongly coupled Ag nanoparticles*, *Phys. Rev. B* **71**, 235408 (2005).
- [15] M. Quinten, A. Leitner, J. R. Krenn, and F. R. Aussenegg, *Electromagnetic energy transport via linear chains of silver nanoparticles*, *Opt. Lett.* **23**, 1331 (1998).
- [16] M. L. Brongersma, J. W. Hartman, and H. A. Atwater, *Electromagnetic energy transfer and switching in nanoparticle chain arrays below the diffraction limit*, *Phys. Rev. B* **62**, 16356 (2000).
- [17] A. F. Koenderink and A. Polman, *Complex response and polariton-like dispersion splitting in periodic metal nanoparticle chains*, *Phys. Rev. B* **74**, 033402 (2006).
- [18] J. V. Hernández, L. D. Noordam, and F. Robicieux, *Asymmetric response in a line of optically driven metallic nanospheres*, *J. Phys. Chem. B* **109**, 15808 (2005).
- [19] A. F. Koenderink, J. V. Hernandez, F. Robicieux, L. D. Noordam, and A. Polman, *Programmable nanolithography with plasmon nanoparticle arrays*, *Nano Lett.* **7**, 745 (2007).
- [20] A. V. Mayshev, V. A. Malyshev, and J. Knoester, *Frequency-controlled localization of optical signals in graded plasmonic chains*, *Nano Lett.* **8**, 2369 (2008).
- [21] H. Ditlbacher, A. Hohenau, D. Wagner, U. Kreibig, M. Rogers, F. Hofer, F. R. Aussenegg, and J. R. Krenn, *Silver nanowires as surface plasmon resonators*, *Phys. Rev. Lett.* **95**, 257403 (2005).

-
- [22] K. Imura, T. Nagahara, and H. Okamoto, *Near-field optical imaging of plasmon modes in gold nanorods*, J. Chem. Phys. **122**, 154701 (2005).
- [23] A. F. Koenderink, M. Kafesaki, B. C. Buchler, and V. Sandoghdar, *Controlling the resonance of a photonic crystal microcavity by a near-field probe*, Phys. Rev. Lett. **95**, 153904 (2005).
- [24] F. I. Baida, A. Belkhir, D. V. Labeke, and O. Lamrous, *Subwavelength metallic coaxial waveguides in the optical range: Role of the plasmonic modes*, Phys. Rev. B **74**, 205419 (2006).
- [25] H. J. Lezec, J. A. Dionne, and H. A. Atwater, *Negative refraction at visible frequencies*, Science **316**, 430 (2007).
- [26] J. A. Dionne, E. Verhagen, A. Polman, and H. A. Atwater, *Are negative index materials achievable with surface plasmon waveguides? A case study of three plasmonic geometries*, Opt. Express **16**, 19001 (2008).
- [27] V. Veselago, *The electrodynamics of substances with simultaneously negative values of ϵ and μ* , Sov. Phys. Usp. **10**, 509 (1968).
- [28] J. Pendry, D. Schurig, and D. Smith, *Controlling electromagnetic fields*, Science **312**, 1780 (2006).
- [29] R. A. Shelby, D. R. Smith, and S. Schultz, *Experimental verification of a negative index of refraction*, Science **292**, 77 (2001).
- [30] G. Dolling, C. Enkrich, M. Wegener, C. M. Soukoulis, and S. Linden, *Simultaneous negative phase and group velocity of light in a metamaterial*, Science **312**, 892 (2006).
- [31] V. M. Shalaev, W. S. Cai, U. K. Chettiar, H. K. Yuan, A. K. Sarychev, V. P. Drachev, and A. V. Kildishev, *Negative index of refraction in optical metamaterials*, Opt. Lett. **30**, 3356 (2005).
- [32] J. Valentine, S. Zhang, T. Zentgraf, E. Ulin-Avila, D. Genov, G. Bartal, and X. Zhang, *Three-dimensional optical metamaterial with a negative refractive index*, Nature **455**, 376 (2008).
- [33] J. B. Pendry, *Negative refraction makes a perfect Lens*, Phys. Rev. Lett. **85**, 3966 (2000).
- [34] U. Leonhardt, *Optical conformal mapping*, Science **312**, 1777 (2006).
-

References

- [35] P. J. Schuck, D. P. Fromm, A. Sundaramurthy, G. S. Kino, and W. E. Moerner, *Improving the mismatch between light and nanoscale objects with gold bowtie nanoantennas*, Phys. Rev. Lett. **94**, 017402 (2005).
- [36] E. Cubukcu, E. A. Kort, K. B. Crozier, and F. Capasso, *Plasmonic laser antenna*, Appl. Phys. Lett. **89**, 093120 (2006).
- [37] W. Chen and H. Ahmed, *Fabrication of 5-7 nm wide etched lines in silicon using 100 keV electron-beam lithography and polymethylacrylate resist*, Appl. Phys. Lett. **62**, 1499 (1993).
- [38] S. Yasin, D. G. Hasko, and H. Ahmed, *Fabrication of < 5 nm width lines in poly(methylmethacrylate) resist using a water:isopropyl alcohol developer and ultrasonically-assisted development*, Appl. Phys. Lett. **78**, 2760 (2001).
- [39] W. Kern and D. A. Puotinen, *Cleaning solutions based on hydrogen peroxide for use in silicon semiconductor technology*, RCA Rev. **31**, 187 (1970).
- [40] D. A. Genov, A. K. Sarychev, V. M. Shalaev, and A. Wei, *Resonant field enhancements from metal nanoparticle arrays*, Nano Lett. **4**, 153 (2004).
- [41] V. Jacobsen, P. Stoller, C. Brunner, V. Vogel, and V. Sandoghdar, *Interferometric optical detection and tracking of very small gold nanoparticles at a water-glass interface*, Opt. Express **14**, 405 (2006).
- [42] C. Loo, A. Lowery, N. Halas, J. West, and R. Drezek, *Immunotargeted nanoshells for integrated cancer imaging and therapy*, Nano Lett. **5**, 709 (2005).
- [43] S. A. Maier, P. G. Kik, H. A. Atwater, S. Meltzer, E. Harel, B. E. Koel, and A. A. G. Requicha, *Local detection of electromagnetic energy transport below the diffraction limit in metal nanoparticle plasmon waveguides*, Nat. Mater. **2**, 229 (2003).
- [44] N. Engheta, A. Salandrino, and A. Alù, *Circuit elements at optical frequencies: Nanoinductors, nanocapacitors, and nanoresistors*, Phys. Rev. Lett. **95**, 095504 (2005).
- [45] D. S. Citrin, *Coherent excitation transport in metal-nanoparticle chains*, Nano Lett. **4**, 1561 (2004).
- [46] W. H. Weber and G. W. Ford, *Propagation of optical excitations by dipolar interactions in metal nanoparticle chains*, Phys. Rev. B **70**, 125429 (2004).

-
- [47] S. Uda, *Wireless beam of short electric waves*, J. IEE , 237 (1926).
- [48] H. Yagi, *Beam transmission of ultra short waves*, IRE Proc. **16**, 715 (1928).
- [49] E. Palik, editor, *Handbook of optical constants of solids*, Academic Press, Inc., Orlando, FL., 1985.
- [50] C. F. Bohren and D. R. Huffman, *Absorption and scattering of light by small particles*, Wiley, New York, 1983.
- [51] K. L. Kelly, E. Coronado, L. L. Zhao, and G. C. Schatz, *The optical properties of metal nanoparticles: The influence of size, shape, and dielectric environment*, J. Phys. Chem. B **107**, 668 (2003).
- [52] O. Haeberlé, M. Ammar, H. Furukawa, K. Tenjimbayashi, and P. Torok, *Point spread function of optical microscopes imaging through stratified media*, Opt. Express **11**, 2964 (2003).
- [53] J. D. Jackson, *Classical electrodynamics*, Wiley, New York, 1975.
- [54] R. de Waele, A. F. Koenderink, and A. Polman, *Tunable nanoscale localization of energy on plasmon particle arrays*, Nano Lett. **7**, 2004 (2007).
- [55] S. A. Maier, M. L. Brongersma, P. G. Kik, and H. A. Atwater, *Observation of near-field coupling in metal nanoparticle chains using far-field polarization spectroscopy*, Phys. Rev. B **65**, 193408 (2002).
- [56] S. A. Maier, P. G. Kik, and H. A. Atwater, *Observation of coupled plasmon-polariton modes in Au nanoparticle chain waveguides of different lengths: Estimation of waveguide loss*, Appl. Phys. Lett. **81**, 1714 (2002).
- [57] S. Y. Park and D. Stroud, *Surface-plasmon dispersion relations in chains of metallic nanoparticles: An exact quasistatic calculation*, Phys. Rev. B **69**, 125418 (2004).
- [58] D. R. Smith, J. B. Pendry, and M. C. K. Wiltshire, *Metamaterials and negative refractive index*, Science **305**, 788 (2004).
- [59] L. Dobrzynski, A. Akjouj, B. Djafari-Rouhani, J. O. Vasseur, M. Bouazaoui, J. P. Vilcot, H. A. Wahsh, P. Zielinski, and J. P. Vigneron, *Simple nanometric plasmon multiplexer*, Phys. Rev. E **69**, 035601 (2004).

References

- [60] L. L. Zhao, K. L. Kelly, and G. C. Schatz, *The extinction spectra of silver nanoparticle arrays: Influence of array structure on plasmon resonance wavelength and width*, J. Phys. Chem. B **107**, 7343 (2003).
- [61] D. S. Citrin, *Plasmon-polariton transport in metal-nanoparticle chains embedded in a gain medium*, Opt. Lett. **31**, 98 (2006).
- [62] C. R. Simovski, A. J. Viitanen, and S. A. Tretyakov, *Resonator mode in chains of silver spheres and its possible application*, Phys. Rev. E **72**, 066606 (2005).
- [63] A. Alu and N. Engheta, *Theory of linear chains of metamaterial/plasmonic particles as subdiffraction optical nanotransmission lines*, Phys. Rev. B **74**, 205436 (2006).
- [64] M. C. K. Wiltshire, E. Shamonina, I. R. Young, and L. Solymar, *Experimental and theoretical study of magneto-inductive waves supported by one-dimensional arrays of "swiss rolls"*, J. Appl. Phys. **95**, 4488 (2004).
- [65] M. Meier and A. Wokaun, *Enhanced fields on large metal particles: dynamic depolarization*, Opt. Lett. **8**, 581 (1983).
- [66] H. Raether, *Surface plasmons on smooth and rough surfaces and on gratings*, Springer-Verlag, Berlin, 1988.
- [67] G. Schider, J. R. Krenn, A. Hohenau, H. Ditlbacher, A. Leitner, F. R. Aussenegg, W. L. Schaich, I. Puscasu, B. Monacelli, and G. Boreman, *Plasmon dispersion relation of Au and Ag nanowires*, Phys. Rev. B **68**, 155427 (2003).
- [68] G. Laurent, N. Felidj, J. Aubard, G. Levi, J. R. Krenn, A. Hohenau, G. Schider, A. Leitner, and F. R. Aussenegg, *Evidence of multipolar excitations in surface enhanced Raman scattering*, Phys. Rev. B **71**, 045430 (2005).
- [69] C. Girard and A. Dereux, *Optical spectroscopy of a surface at the nanometer-scale – A theoretical study in real space*, Phys. Rev. B **49**, 11344 (1994).
- [70] N. Yamamoto, K. Araya, and F. J. García de Abajo, *Photon emission from silver particles induced by a high-energy electron beam*, Phys. Rev. B **64**, 205419 (2001).
- [71] J. T. V. Wijngaarden, E. Verhagen, A. Polman, C. E. Ross, H. J. Lezec, and H. A. Atwater, *Direct imaging of propagation and damping of near-resonance surface plasmon polaritons using cathodoluminescence spectroscopy*, Appl. Phys. Lett. **88**, 221111 (2006).

-
- [72] M. V. Bashevov, F. Jonsson, A. V. Krasavin, N. I. Zheludev, Y. Chen, and M. I. Stockman, *Generation of traveling surface plasmon waves by free-electron impact*, Nano Lett. **6**, 1113 (2006).
- [73] J. Nelayah, M. Kociak, O. Stephan, F. J. García de Abajo, M. Tence, L. Henrard, D. Taverna, I. Pastoriza-Santos, L. M. Liz-Marzan, and C. Colliex, *Mapping surface plasmons on a single metallic nanoparticle*, Nat. Phys. **3**, 348 (2007).
- [74] M. Bosman, V. J. Keast, M. Watanabe, A. I. Maarroof, and M. B. Cortie, *Mapping surface plasmons at the nanometre scale with an electron beam*, Nanotechnology **18**, 165505 (2007).
- [75] E. Verhagen, A. Polman, and L. Kuipers, *Nanofocusing in laterally tapered plasmonic waveguides*, Opt. Express **16**, 45 (2008).
- [76] C. Hubert, A. Rumyantseva, G. Lerondel, J. Grand, S. Kostcheev, L. Billot, A. Vial, R. Bachelot, P. Royer, S. H. Chang, S. K. Gray, G. P. Wiederrecht, and G. C. Schatz, *Near-field photochemical imaging of noble metal nanostructures*, Nano Lett. **5**, 615 (2005).
- [77] H. Miyazaki and Y. Kurokawa, *Squeezing visible light waves into a 3-nm-thick and 55-nm-long plasmon cavity*, Phys. Rev. Lett. **96**, 097401 (2006).
- [78] N. Fang, H. Lee, C. Sun, and X. Zhang, *Sub-diffraction-limited optical imaging with a silver superlens*, Science **308**, 534 (2005).
- [79] A. Alù and N. Engheta, *Multifrequency optical invisibility cloak with layered plasmonic shells*, Phys. Rev. Lett. **100**, 113901 (2008).
- [80] W. J. Fan, S. Zhang, B. Minhas, K. J. Malloy, and S. R. J. Brueck, *Enhanced infrared transmission through subwavelength coaxial metallic arrays*, Phys. Rev. Lett. **94**, 033902 (2005).
- [81] J. Salvi, M. Roussey, F. I. Baida, M. P. Bernal, A. Mussot, T. Sylvestre, H. Maillotte, D. V. Labeke, A. Perentes, I. Utke, C. Sandu, P. Hoffmann, and B. Dwir, *Annular aperture arrays: study in the visible region of the electromagnetic spectrum*, Opt. Lett. **30**, 1611 (2005).
- [82] S. M. Orbons, A. Roberts, D. N. Jamieson, M. I. Haftel, C. Schlockermann, D. Freeman, and B. Luther-Davies, *Extraordinary optical transmission with coaxial apertures*, Appl. Phys. Lett. **90**, 251107 (2007).
-

References

- [83] M. I. Haftel, C. Schlockermann, and G. Blumberg, *Enhanced transmission with coaxial nanoapertures: Role of cylindrical surface plasmons*, Phys. Rev. B **74**, 235405 (2006).
- [84] M. I. Haftel, C. Schlockermann, and G. Blumberg, *Role of cylindrical surface plasmons in enhanced transmission*, Appl. Phys. Lett. **88**, 193104 (2006).
- [85] D. V. Labeke, D. Gerard, B. Guizal, F. I. Baida, and L. Li, *An angle-independent frequency selective surface in the optical range*, Opt. Express **14**, 11945 (2006).
- [86] J. A. Stratton, *Electromagnetic theory*, McGraw-Hill Book Company, New York, London, 1st ed. edition, 1941.
- [87] D. Marcuse, *Light transmission optics*, Van Nostrand Reinhold, New York, 1972.
- [88] L. Novotny and C. Hafner, *Light propagation in a cylindrical waveguide with a complex, metallic, dielectric function*, Phys. Rev. E **50**, 4094 (1994).
- [89] J. Weeber, M. U. González, A. L. Baudrion, and A. Dereux, *Surface plasmon routing along right angle bent metal strips*, Appl. Phys. Lett. **87**, 221101 (2005).
- [90] A. Drezet, F. R. Aussenegg, A. Leitner, and J. R. Krenn, *Dielectric stripes on gold as surface plasmon waveguides*, Appl. Phys. Lett. **88**, 094104 (2006).
- [91] P. Berini, *Plasmon polariton modes guided by a metal film of finite width*, Opt. Lett. **24**, 1011 (1999).
- [92] M. Sandtke and L. Kuipers, *Slow guided surface plasmons at telecom frequencies*, Nat. Phot. **1**, 573 (2007).
- [93] M. I. Stockman, *Nanofocusing of optical energy in tapered plasmonic waveguides*, Phys. Rev. Lett. **93**, 137404 (2004).
- [94] J. A. Dionne, L. A. Sweatlock, H. A. Atwater, and A. Polman, *Plasmon slot waveguides: Towards chip-scale propagation with subwavelength-scale localization*, Phys. Rev. B **73**, 035407 (2006).
- [95] G. Shvets, *Photonic approach to making a material with a negative index of refraction*, Phys. Rev. B **67**, 035109 (2003).

-
- [96] R. de Waele, S. P. Burgos, A. Polman, and H. A. Atwater, *Plasmon dispersion in coaxial waveguides from single-cavity optical transmission measurements*, Submitted, 2009.
- [97] V. M. Shalaev, *Optical negative-index metamaterials*, Nat. Phot. **1**, 41 (2007).
- [98] G. Dolling, M. Wegener, and S. Linden, *Realization of a three-functional-layer negative-index photonic metamaterial*, Opt. Lett. **32**, 551 (2007).
- [99] P. B. Johnson and R. W. Christy, *Optical constants of the noble metals*, Phys. Rev. B **6**, 4370 (1972).
- [100] A. Alù, M. G. Silveirinha, A. Salandrino, and N. Engheta, *Epsilon-near-zero metamaterials and electromagnetic sources: Tailoring the radiation phase pattern*, Phys. Rev. B **75**, 155410 (2007).
- [101] Z. Jacob, L. V. Alekseyev, and E. Narimanov, *Optical hyperlens: Far-field imaging beyond the diffraction limit*, Opt. Express **14**, 8247 (2006).
- [102] D. Shurig, J. J. Mock, B. J. Justice, S. A. Cummer, J. B. Pendry, A. F. Starr, and D. R. Smith, *Metamaterial electromagnetic cloak at microwave frequencies*, Science **314**, 977 (2006).
- [103] W. Cai, U. K. Chettiar, A. V. Kildishev, and V. M. Shalaev, *Optical cloaking with metamaterials*, Nat. Phot. **1**, 224 (2007).
- [104] R. Liu, C. Ji, J. J. Mock, J. Y. Chin, T. J. Cui, and D. R. Smith, *Broadband ground-plane cloak*, Science **323**, 366 (2009).
- [105] D. R. Smith, W. J. Padilla, D. C. Vier, S. C. Nemat-Nasser, and S. Schultz, *Composite medium with simultaneously negative permeability and permittivity*, Phys. Rev. Lett. **84**, 4184 (2000).
- [106] S. Zhang, Y. S. Park, J. Li, X. Lu, W. Zhang, and X. Zhang, *Negative refractive index in chiral metamaterials*, Phys. Rev. Lett. **102**, 023901 (2009).
- [107] G. Dolling, M. Wegener, C. Soukoulis, and S. Linden, *Negative-index metamaterial at 780 nm wavelength*, Opt. Lett. **32**, 53 (2007).
- [108] S. Zhang, W. J. Fan, N. C. Panoiu, K. J. Malloy, R. M. Osgood, and S. R. J. Brueck, *Experimental demonstration of near-infrared negative-index metamaterials*, Phys. Rev. Lett. **95**, 137404 (2005).
-

SUMMARY

Plasmons are collective oscillations of free electrons in a metal. At optical frequencies plasmons enable nanoscale confinement of light in metal nanostructures. This ability has given rise to many applications in e.g. photothermal cancer treatment, light trapping in photovoltaic cells, and sensing. Metal nanostructures also allow for manipulation of optical energy, providing such functionalities as guiding or redirecting light at the nanoscale.

This thesis focuses on nanoscale control of light using three types of metal nanostructures: 1) arrays of coupled metal nanoparticles, 2) metal nanowires, and 3) (coupled) coaxial waveguides.

In chapter 2 we first discuss the fabrication of metal nanostructures. We describe how electron-beam lithography and lift-off is used to fabricate Au and Ag nanoparticle arrays on glass with particles as small as 50 nm at an array pitch of 75 nm. Furthermore, we discuss how ion-beam lithography was used to fabricate coaxial plasmon waveguides composed of a Ag core, surrounded by a dielectric channel with a thickness down to 20 nm, clad in Ag.

Chapter 3 describes the optical behavior of metal nanoparticle array illuminated sideways along the array axis. Confocal microscopy shows that field concentrates on just a few particles at the front or back side of the particle chain. By changing the illumination wavelength we can control which side of the chain becomes excited. This work demonstrates a new paradigm for nanoantenna design, which is based on engineering of the interference between multiple antenna elements, rather than relying on field enhancement in the gap between two nanoantennas.

In chapter 4 we discuss angle resolved transmission measurements to determine the dispersion relation of plasmon modes in Au and Ag particle arrays. We find a large splitting between longitudinal and transverse modes that is inconsistent with reported electrostatic near-field models. Our results confirm that far-field dynamic interactions between particles are important, even for $\lambda/5$ -sized

structures. Taking into account dynamic interactions we calculate that the propagation length in plasmon particle arrays can be as much as 10 μm , which is an order of magnitude higher than previously estimated using quasi-electrostatic theory.

In chapter 5 we show that metal nanowires behave as plasmon resonators. We use cathodoluminescence imaging spectroscopy to determine the eigenmodes in 500–1200-nm-long Au nanowires at a resolution less than 10 nm. We find that the plasmon wavelength in the metal nanowires is significantly shorter than the free-space wavelength at the same energy. By combining spectral and spatial information we determine the dispersion relation for plasmons confined within the metal nanowires.

Chapter 6 focuses on coaxial plasmon waveguides. Optical transmission measurements on coaxial apertures in a Ag film point out that the plasmon dispersion in coaxial waveguides depends greatly on the refractive index and thickness of the dielectric channel. We find that the plasmon wavelength can be as small as 210 nm in coaxial apertures with ~ 50 -nm-wide dielectric channels at propagation lengths of $\sim 2 \mu\text{m}$. A plasmon phase shift up to π occurs upon reflection off the aperture ends. The phase shift depends greatly on the coax geometry, thereby providing further tunability of the optical behavior of coaxial nanostructures.

In chapter 7 we report on calculations of plasmon dispersion relations in coaxial waveguides. We find that certain coax geometries sustain modes of negative refractive index at optical frequencies. The spectral region of negative index can be shifted throughout the entire visible spectral range by changing the dielectric channel width from 10 to 70 nm. Furthermore, by fine-tuning the dielectric width, the special cases $n = -1$ and $n = 0$ can be achieved in the coax, while maintaining a propagation length of 500 nm or more.

Finally, in chapter 8 we present a novel optical metamaterial, composed of a single functional layer containing coupled coaxial Ag/GaP/Ag channels, that exhibits a negative index of refraction $n \sim -2$ in the blue. Using finite-difference time-domain simulations we find that the metamaterial index is independent of the angle-of-incidence over an angular range $\pm 50^\circ$ and is independent of polarization. This work signifies an important step towards the realization of nanoscale imaging of e.g. biological samples, and invisibility cloaking in the visible spectral range.

Altogether, this thesis demonstrates several new opportunities for resonant plasmonic nanostructures to control optical fields at the nanoscale. The presented concepts and insights hold great promise for new applications in integrated optics, photovoltaics, solid-state lighting, imaging below the diffraction limit, and even invisibility cloaking.

SAMENVATTING

Plasmonen zijn collectieve oscillaties van vrije elektronen in een metaal. Bij optische frequenties maken plasmonen het mogelijk licht op te sluiten in metalen nanostructuren. Deze eigenschap heeft geleid tot een groot scala aan toepassingen voor bijvoorbeeld de behandeling van kanker, lichtopsluiting in zonnecellen, en sensoren. Metalen nanostructuren maken het tevens mogelijk optische energie op nanoschaal te manipuleren. Dit verschaft een manier om licht te sturen en transporteren op lengteschalen kleiner dan de optische diffractielimiet.

Dit proefschrift richt zich op controle van licht op nanoschaal met drie typen metaalstructuren, te weten: 1) kettingen van gekoppelde metalen nanodeeltjes, 2) metalen nanodraden, en 3) (gekoppelde) coaxiale golfgeleiders.

In hoofdstuk 2 wordt allereerst besproken hoe metaalstructuren gefabriceerd kunnen worden. We beschrijven hoe elektronenbundellithografie gebruikt is om gouden (Au) en zilveren (Ag) nanodeeltjeskettingen aan te brengen op glas, met deeltjesdiameters van slechts 50 nm en een periodiciteit van slechts 75 nm. Verder behandelen we hoe ionenbundellithografie gebruikt kan worden om coaxiale plasmonogolfgeleiders te maken met een zilveren kern, omgeven door een diëlektrisch kanaal met een breedte van slechts 20 nm, ingebed in zilver.

Hoofdstuk 3 beschrijft vervolgens het optisch gedrag van rijen van metalen nanodeeltjes wanneer deze langs de as belicht worden. Met behulp van confocale microscopie laten we zien dat het lichtveld zich concentreert op een of twee nanodeeltjes aan de voor- of achterkant van de deeltjesketting. Door de belichtingsgolflengte te variëren kunnen wij controleren welke kant van de deeltjesrij aangeslagen raakt. Hiermee demonstreren wij een nieuw paradigma voor het ontwerpen van nanoantennes: in plaats van gebruik te maken van veldversterking tussen twee gekoppelde antennes is het ook mogelijk interferentie van vele verschillende antennes te gebruiken om op nanoschaal veld te concentreren.

In hoofdstuk 4 worden hoekafhankelijke metingen beschreven, die gedaan zijn om de plasmondispersie in gouden en zilveren deeltjeskettingen te bepalen. We

observeren een grote splitsing tussen de longitudinale en transversale modes die niet verenigbaar is met bestaande elektrostatische modellen. Onze resultaten bevestigen dat verre-veldeffecten tussen deeltjes van groot belang zijn, zelfs als de grootte van de structuur slechts een vijfde van de golflengte is. Wanneer dynamische interacties tussen deeltjes in beschouwing genomen worden berekenen we dat de weglengte van plasmons in deeltjeskettingen wel 10 micrometer groot kan zijn, wat een orde van grootte meer is dan eerder voorspeld op basis van elektrostatische theorie.

In hoofdstuk 5 tonen we aan dat metalen nanodraden zich gedragen als resonatoren voor plasmonen. We gebruiken cathodoluminescentiemicroscopie om plasmonische eigenmodes in gouddraden met een lengte van 500–1200 nanometer te visualiseren met een resolutie van 10 nm. We demonstreren dat de golflengte in metalen nanodraden significant korter is dan de vrije golflengte van licht bij dezelfde energie. Door het combineren van de ruimtelijke en spectrale informatie bepalen we de dispersierelatie voor plasmonen die zijn opgesloten in de nanodraden.

Hoofdstuk 6 richt zich op coaxiale plasmongolfgeleiders. Optische transmissiemetingen aan coaxiale gaten in een zilverfilm laten zien dat de plasmondispersie in coaxiale kanalen sterk afhangt van de brekingsindex en breedte van het diëlektrische kanaal. We tonen aan dat de golflengte van licht gereduceerd kan worden tot wel ~ 210 nm met plasmonweglengte van ~ 2 μm bij een vrije golflengte van 450 nm in coaxiale plasmongolfgeleiders met ~ 50 nm brede diëlektrische kanaaltjes. Verder hebben we ontdekt dat significante fasesprongen (tot π) kunnen plaatsvinden wanneer plasmonen reflecteren aan de uiteinden van de coaxiale golfgeleiders. Aangezien deze fasesprongen sterk afhangen van de coaxgeometrie bieden ze naast de dispersie een tweede manier om het optische gedrag van coaxiale nanostructuren te controleren.

In hoofdstuk 7 rapporteren we berekeningen van de plasmondispersie in coaxiale golfgeleiders. Deze berekeningen tonen aan dat zekere coaxgeometrieën een negatieve brekingsindex hebben bij optische frequenties. Door middel van het veranderen van de diëlektrische kanaalbreedte kan het negatieve indexgebied verschoven worden van de rode tot blauwe kant van het zichtbare spectrum. We tonen aan dat brekingsindices van $n = -1$ en $n = 0$ bereikt kunnen worden bij een plasmonweglengte van meer dan 500 nm.

Tenslotte presenteren we in hoofdstuk 8 een metamateriaal gebaseerd op een enkele laag van gekoppelde coaxiale golfgeleiders met zilveren kern en buitenzijde en galliumfosfide kanaal. We tonen aan dat dit nieuwe metamateriaal een negatieve brekingsindex $n \sim -2$ in het blauwe deel van het spectrum heeft. Door middel van simulaties laten we zien dat de brekingsindex in het metamateriaal

bijna niet afhangt van de hoek van inval en polarisatie. Met dit werk wordt een belangrijke stap gezet naar realisatie van lichtmicroscopie op nanoschaal en ontzichtbaarheid bij optische frequenties.

Samenvattend demonstreert dit proefschrift verschillende nieuwe mogelijkheden voor controle van licht op nanoschaal met plasmonische metaalstructuren. De concepten en inzichten die besproken worden zijn veelbelovend voor diverse nieuwe applicaties in geïntegreerde optica, zonnecellen, verlichting, nanomicroscopie, en onzichtbaarheidsbekleding.

ACKNOWLEDGEMENTS

Many people have contributed to this thesis in one way or another. I would like to start by acknowledging a few people in particular.

My first words of thanks are for my “promotor” Albert Polman, who provided me with four years of fascinating research. His fresh view on science and positive attitude have always been very stimulating. I am especially grateful for the opportunity to spend a year at Caltech and for all the support I received during parenthood.

The second person that I owe a great deal to is Femius Koenderink. I have learned an incredible amount from him during my rookie years as a Ph.D. student. Femius’ very own sense of humor and goal-getting attitude always made it fun and exciting to work together.

I would also like to thank Ernst Jan Vesseur for a fruitful and enjoyable collaboration. Ernst Jan has the rare ability to harmoniously combine a boundless enthusiasm with a critical mind. Many thanks also to Ewold Verhagen for many insightful discussions on the theory behind chapters 6 to 8. I am specially indebted to Maarten Hebbink for his patience and self-initiative during the hectic time while I was finishing my thesis.

I am grateful also to the other members of the Photonic Materials group: Martin Kuttge, Rob van Loon, Robb Walters, Erwin Kroekenstoel, Marc Verschuuren, Sébastien Bidault, Hans Mertens, Kylie Catchpole, Joan Penninkhof, Jeroen Kalkman, Anna Tchebotareva, Teun van Dillen, Timon van Wijngaarden and Martien den Hartog, thank you for many hours of stimulating discussion. I would like to thank Petra Rodriguez, Johan Derks and Hans Zeijlemaker as well for being an essential part of the team.

Furthermore, I would like to acknowledge all the people in the Center for Nanophotonics. It has been great to learn so much about everyone’s research. On top of this, the exhilarating nanophotonics colloquia have prepared me for even the toughest of audiences. I would like to specially thank Jord Prangma

Acknowledgements

and Kobus Kuipers for many stimulating discussions and for facilitating the measurements discussed in chapter 4.

Sample fabrication led me to spend many hours in AMOLF's Nanocenter cleanroom. I am extremely grateful to Chris Rétif who has been a great source of good ideas and conversation. I would also like to thank Hans Zeijlemaker for his unbridled enthusiasm and for the many improvements he made to the cathodoluminescence setup. Many thanks to the entire support staff for always being very helpful and creating a great atmosphere at AMOLF.

At Caltech, I owe a great deal of thanks to many people who made my stay there both successful and very enjoyable. First and foremost I would like to thank Harry Atwater for the opportunity he gave me. I greatly appreciate his warm hospitality and stimulating guidance throughout the year.

Second, I have had the great pleasure to closely collaborate with Stanley Burgos. Our connecting views and many exciting discussions led to a very fruitful outcome described in chapters 6 to 8. Science aside, my friendship with Stan (and his family) made all the difference during my year at Caltech.

I would also like to acknowledge Carry Hofmann for introducing me to Caltech and for the many hours she spent with me at the Nanoprobe. Furthermore, I thank Jennifer Dionne for sharing her knowledge and experience with me. Special thanks also to April Neidholdt for making me feel at home away from home. Being part of the A-team for a year has been an awesome experience and I would like to thank each and everyone on the team.

Last but not least I want to express my gratitude to my friends and family for their enduring support these last four years. Thanks Jeroen for always offering me a roof over my head in Diemen after a late night at AMOLF, and thank you and Daniele for being "paranimf". Nira, your support and belief in me have been incredible. I am forever grateful to you for having been pretty much a single working mother these past months. I love that life with you is always exciting and on the move. Above all, I love that it brought us Ella. I cannot wait for our next adventures together.

ABOUT THE AUTHOR

René de Waele was born on July 13, 1981 in Oss, The Netherlands. He obtained his VWO (secondary education) degree at the “Maaslandcollege” in Oss in 1999. René went on to study chemistry at the “Utrecht University”. In 2002 he performed a research project focused on phase-separation in colloid-polymer mixtures under supervision of Prof. Dr. H. N. W. Lekkerkerker. Two years later he investigated PbSe nanowire growth in the group of Prof. Dr. D. A. M. Vanmaekelbergh. René concluded his studies with an internship at the FOM Institute for Atomic and Molecular

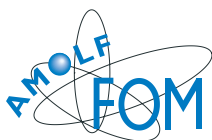


Physics (AMOLF) in Amsterdam, where he worked on self-assembly of particle plasmon waveguides under supervision of Prof. Dr. A. Polman in collaboration with Prof. Dr. A. van Blaaderen. In 2005 he received his M.Sc. degree with honors (“cum laude”). He continued his research at AMOLF as a Ph.D. student. The research performed within the context of this Ph.D. project is the subject of this thesis. Part of the work described in this thesis was performed in the course of a one-year visit of René to the group of Prof. H. A. Atwater at the California Institute of Technology in Pasadena, California. Aside from his scientific career René is part-owner of a software company, and has been an active bridge player, twice winning the Dutch national championships in the under-twenties and students categories.

LIST OF PUBLICATIONS

This thesis is based on the following publications:

- *Tunable nanoscale localization of energy on plasmon particle arrays*, R. de Waele, A. F. Koenderink, and A. Polman, *Nano Lett.* **7**, 2004 (2007); also highlighted in *Nature* **448**, 141 (2007). (**Chapter 3**)
 - *Experimental evidence for large dynamic effects on the plasmon dispersion of subwavelength metal nanoparticle waveguides*, A. F. Koenderink, R. de Waele, and A. Polman, *Phys. Rev. B* **76**, 201403 (2007). (**Chapter 4**)
 - *Direct observation of plasmonic modes in Au nanowires using high-resolution cathodoluminescence spectroscopy*, E. J. R. Vesseur, R. de Waele, M. Kuttge, and A. Polman, *Nano Lett.* **7**, 2843 (2007). (**Chapter 5**)
 - *Plasmon dispersion in coaxial waveguides from single-cavity optical transmission measurements*, R. de Waele, S. P. Burgos, A. Polman, and H. A. Atwater, *Nano Lett.* **9** (2009), in press. (**Chapter 6**)
 - *Negative refractive index in coaxial plasmon waveguides*, R. de Waele, S. P. Burgos, H. A. Atwater, and A. Polman, to be submitted. (**Chapter 7**)
 - *A single-layer negative-index metamaterial at visible frequencies*, S. P. Burgos*, R. de Waele*, A. Polman, and H. A. Atwater, to be submitted. (**Chapter 8**)
- *Joint first authors



The work described in this thesis was performed at the FOM-Institute for Atomic and Molecular Physics, Science Park 113, 1098 XG Amsterdam, The Netherlands, in collaboration with California Institute of Technology, Pasadena, CA, United States.

Affiliation:

Prof. Dr. A. Polman
Center for Nanophotonics
FOM-Institute AMOLF, Amsterdam, The Netherlands